TECHNISCHE
UNIVERSITÄT
DARMSTADT

Surface forces across colloidal dispersions

A study on the influence of the dispersions' nanostructure and oscillatory structural forces

Vom Fachbereich Physik
der Technischen Universität Darmstadt

zur Erlangung des akademischen Grades

Doktor der Naturwissenschaften (Dr. rer. nat.)

genehmigte Dissertation von
M. Sc. Michael Ludwig
aus Wörth an der Donau

Darmstadt 2021
D17

Ludwig, Michael: Surface forces across colloidal dispersions
Darmstadt, Technische Universität Darmstadt
Jahr der Veröffentlichung der Dissertation auf TUprints: 2021
URN: urn:nbn:de:tuda-tuprints-190985
Tag der mündlichen Prüfung: 30.06.2021

Promotionsausschuss:

Referentin:	Prof. Dr. Regine von Klitzing
Koreferent:	Prof. Dr. Emanuel Schneck
Prüfer:	Prof. Dr. Benno Liebchen
Prüfer:	Prof. Dr. Jens Braun

Tag der Disputation: 30.06.2021

Erklärung gemäß § 9 Promotionsordnung

Hiermit versichere ich, dass ich die vorliegende Dissertation selbstständig angefertigt und keine anderen als die angegebenen Quellen und Hilfsmittel verwendet habe. Alle wörtlichen und paraphrasierten Zitate wurden angemessen kenntlich gemacht. Die Arbeit hat bisher noch nicht zu Prüfungszwecken gedient.

_____

Datum und Unterschrift

Abstract

Colloid based products are ubiquitous in our daily life and precise knowledge of the interactions in these systems is of great interest in basic as well as in applied sciences. This thesis studies forces between macroscopic surfaces interacting across concentrated colloidal dispersions, focussing on the mutual effect between the dispersions' nanostructure and surface forces. Besides the well-known DLVO-type surface forces, specific structuring of colloidal particles may induce the so-called oscillatory structural forces. In particular, this study utilises two model colloidal dispersions: suspensions of silica nanoparticles and dispersions of self-assembled surfactant micelles. Throughout this work, surface forces across these colloidal dispersions are measured using colloidal-probe atomic force microscopy.

In dispersions of charged colloidal particles, electrostatic interactions cause a pronounced interparticle structuring. For spherical particles, the mean interparticle distance scales with the particles' volume fraction according to an inverse cubic root scaling law. Oscillatory structural forces across these dispersions typically show a wavelength which is directly related to the respective mean interparticle distance. Consequently, the measurement of oscillatory structural forces can be utilised as a tool for characterisation of colloidal particles, knowing the particles' volume fraction. This is demonstrated by measuring surface forces across concentrated silica nanoparticle suspensions to determine the respective nanoparticles' diameters.

The validity of this inverse cubic root scaling law is checked upon variation of the particles' surface charges. Mixing nonionic and anionic surfactants form particles with tunable surface charge as demonstrated by small-angle neutron scattering. It is shown that the inverse cubic root scaling law is only valid for highly charged colloidal particles. If the particles carry little or no charges, their interparticle structuring decreases. By this means, the oscillatory structural forces across dispersions are precisely tuned not only by the particles' volume fraction but also by the amount of surface charges per particle.

Complete description of the surface forces requires further contributions, other than the oscillatory structural forces. Here, forces between charged surfaces across concentrated silica nanoparticle suspensions are modelled as a superposition of two individual contributions - the electrostatic double layer and the oscillatory structural force. The electrostatic screening length of colloidal dispersions, an important parameter for the description of the electrostatic double layer force, is independently determined by conductivity measurements. In that way, both force contributions are untangled. This enables a uniform description of the surface forces from a few hundred nanometres down to the surfaces being almost in contact.

Kurzzusammenfassung

Kolloid-basierte Produkte spielen eine große Rolle in unserem täglichen Leben. Das Verständnis der Wechselwirkungen in diesen Systemen stellt einen wichtigen Aspekt der aktuellen Forschung dar. Diese Arbeit untersucht Oberflächenkräfte in kolloidalen Dispersionen im Hinblick auf die gegenseitige Beeinflussung der Nanostruktur dieser Dispersionen und der Oberflächenkräfte. Neben den Oberflächenkräften, welche durch die DLVO-Theorie beschrieben werden, treten oszillierende Strukturkräfte aufgrund einer spezifischen Ordnung der kolloidalen Partikel auf. Es werden zwei Modellsysteme als kolloidale Dispersionen verwendet: Suspensionen von Siliziumdioxid-Nanopartikeln und Dispersionen von Tensidmizellen. Im Rahmen dieser Arbeit werden Oberflächenkräfte in kolloidalen Dispersionen mit Hilfe der kolloidalen Sonden - Rasterkraftmikroskopie gemessen.

Elektrostatische Wechselwirkungen verursachen in Dispersionen von geladenen Partikeln eine ausgeprägte Ordnung zwischen diesen. Für sphärische Partikel skaliert der mittlere Partikelabstand mit dem Volumenanteil der dispergierten Partikel über eine inverse Kubikwurzelabhängigkeit. Oszillierende Strukturkräfte in diesen Dispersionen zeigen typischerweise eine Wellenlänge, welche sich direkt auf den mittleren Partikelabstand bezieht. Mit diesem Wissen kann eine Messung von oszillierenden Strukturkräften, bei bekanntem Volumenanteil der Partikel, zur Bestimmung von Partikeleigenschaften genutzt werden. Im Speziellen wird dies anhand der Bestimmung der Durchmesser von Nanopartikeln durch Kraftmessungen in kolloidalen Suspensionen demonstriert.

Die Gültigkeit dieser inversen Kubikwurzelabhängigkeit wird im Hinblick auf eine veränderte Oberflächenladung der Partikel überprüft. Durch Mischung von nicht-ionischen und ionischen Tensiden kann die Oberflächenladung von Partikel eingestellt werden, was mit Hilfe von Kleinwinkel-Neutronenstreuung nachgewiesen wird. Es wird gezeigt, dass die inverse Kubikwurzelabhängigkeit ausschließlich bei stark geladenen Partikeln erhalten wird. Mit abnehmender Oberflächenladung ist die Ordnung zwischen den Partikeln weniger ausgeprägt und deren mittlerer Partikelabstand reduziert. Somit werden oszillierende Strukturkräfte in diesen Dispersionen sowohl über den Volumenanteil, als auch die Oberflächenladung der Partikel genau angepasst.

Um die komplette Oberflächenkraft zu beschreiben ist es notwendig neben den oszillierenden Strukturkräften weitere Kraftbeiträge zu betrachten. Hier werden Kräfte zwischen geladenen Oberflächen in Suspensionen von Nanopartikeln mit einer Superposition von elektrostatischen Doppelschichtkräften und oszillierenden Strukturkräften modelliert. Die elektrostatische Abschirmlänge kolloidaler Dispersionen, ein wichtiger Parameter für die Beschreibung

der elektrostatischen Doppelschichtkraft, wird über Leitfähigkeitsmessungen unabhängig bestimmt. Auf diese Weise können beide Kraftbeiträge separiert werden. Dies ermöglicht eine einheitliche Beschreibung der Oberflächenkraft bis zu einem Abstand, bei welchem sich beide Oberflächen fast berühren.

Contents

List of abbreviations

AFM	Atomic force microscopy
CP-AFM	Colloidal probe atomic force microscopy
dl	Diffuse layer (potential), double layer (force)
DLVO	Derjaguin, Landau, Verwey, and Overbeek
DH	Debye-Hückel
el	Electrostatic
EDL	Electrical double layer
JA	Jellium approximation
MSA	Mean spherical approximation
NP	Nanoparticle
OLS	Optical lever sensitivity
osc	Oscillatory
OZ	Ornstein-Zernike
PB	Poisson-Boltzmann
PY	Percus-Yevick
SANS	Small-angle neutron scattering
SFA	Surface forces apparatus
str	Structural
TEM	Transmission electron microscopy
vdW	van der Waals

List of symbols

a	Area / m^2
A	Amplitude of oscillatory forces / $\mathrm{N\,m^{-1}}$
A_H	Hamaker constant / J
B	Background
c	Concentration / $\mathrm{mol\,L^{-1}}$
C	Constant
cmc	Critical micelle concentration / $\mathrm{mol\,L^{-1}}$
d	Diameter / m
d_{eff}	Effective (interaction) diameter / m
D^*	Mean (bulk) distance / m
F	Force / N
$g(r)$	Radial (pair) distribution function
h	Surface separation / m
h'	Offset / m
I	Ionic strength / $\mathrm{mol\,L^{-1}}$
k_c	Cantilever spring constant / $\mathrm{N\,m}$

$\vec{k}$	Wave propagation vector
K	Electrolytic conductivity / $\mathrm{S\,m^{-1}}$
N_{agg}	Aggregation number
n_p	Particle number density, number concentration / $\mathrm{m^{-3}}$
$P(q)$	Form factor
$\vec{q}$	Scattering vector / $\mathrm{m^{-1}}$
r	(Radial) distance / m
r_c	Core radius / m
r_{eff}	Effective (particle) radius / m
R	Radius / m
R_{eff}	Effective (interaction) radius / m
$S(q)$	Static structure factor
T	Absolute temperature / K
t_s	Shell thickness / m
U	Interaction potential (free energy) / J
W	Interaction potential per unit area, surface energy / $\mathrm{J\,m^{-2}}$
x	Distance / m
x_c	Core axial ratio
z	Valency
β	Fractional charge
ϵ	Relative permittivity
κ^{-1}	Debye length / m
λ	Wavelength / m
ϕ	Volume fraction
Π	(Disjoining) pressure / $\mathrm{N\,m^{-2}}$
ψ	Surface potential / V
ρ	Density
σ	Surface charge density / $\mathrm{C\,m^{-2}}$
ξ	Decay length / m
ζ	Zeta-potential / V

List of physical constants

Archimedes constant	π	$= 3.141\,592\,653\,59\ldots$
Avogadro constant	N_A	$= 6.022\,14 \times 10^{23}\,\mathrm{mol^{-1}}$
Boltzmann constant	k	$= 1.380\,65 \times 10^{-23}\,\mathrm{J\,K^{-1}}$
Elementary charge	e	$= 1.602\,176 \times 10^{-19}\,\mathrm{C}$
Vacuum permittivity	ϵ_0	$= 8.854\,19 \times 10^{-12}\ \mathrm{C\,V^{-1}\,m^{-1}}$

Non-essential and empirical parameters are not included

1 Introduction

1.1 Motivation

Colloid based products are ubiquitous in our daily life and govern countless environmental and technical processes. Emulsions, foams, gels, polymer latexes, paints & inks are all colloidal dispersions. They have a huge impact on the daily life and are important in industrial applications.

Despite daily consumer products and economically relevant applications being prominent examples, the outstanding importance of colloidal science is often found looking into nature. Biological processes are mostly driven by colloidal interactions. The first detailed description of the suspension stability of blood reaches back almost 100 years [1]. The organisation of living matter in general [2] and of cellular structures in particluar are also important examples, since 20 - 30 % of the cellular volume is occupied by soluble proteins and macromolecules, *i.e.* collodial particles [3, 4]. The understanding of colloidal interactions led to various applications, such as an increased target cell specifity in drug delivery [5] or the formation of antimicrobal nanostructured surfaces [6].

Listing only a few examples reveals that the term "colloid" comprises a tremendous number of different systems. Yet, all of them share one common feature: their constituents are characterised by extremely different size dimensions. Irrespective of the actual dimensions, the surfaces of larger particles may serve as spatial confinement of the smaller particles, as illustrated in Fig. 1.1.

Understanding the fundamental forces acting between surfaces - from planar macroscopic surfaces to interparticle forces on various length scales - is, therefore, an important problem for basic as well as for applied science. These interactions determine the macroscopic behaviour of colloidal systems, such as their phase behaviour [8, 9]

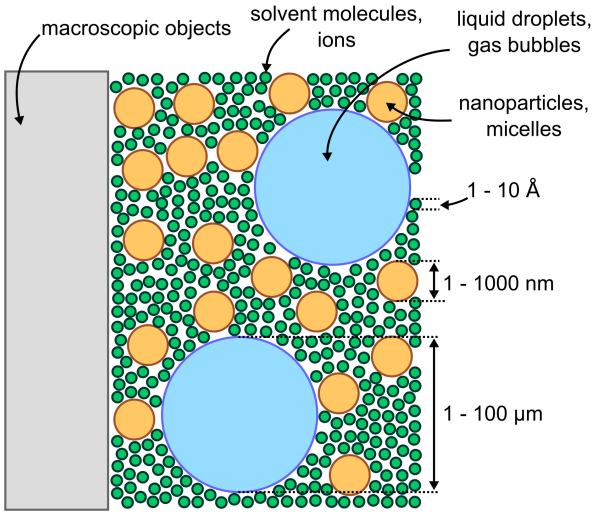

Figure 1.1: Sketch demonstrating different length scales in colloidal dispersions, starting from molecular scale of the dispersing medium, often water and hydrated ions. The mesoscopic length scale includes nanometer sized objects, often nanoparticles or surfactant micelles. Dispersed emulsion droplets or gas bubbles are often considered at the microscopic scale. At some point, the dispersion interacts with macroscopic objects. (adapted from [7])

or their bulk rheology [10]. This knowledge allows a precise formulation of products and processes including coagulation, flocculation, sedimentation, or lubrication. This work contributes to a better understanding of fundamental forces between surfaces across concentrated colloidal dispersions by addressing following topics: (i) the influence of the confined colloidal particles' surface charges, (ii) the interaction between confining surfaces and the colloidal dispersion, and (iii) the distribution and structure of colloidal particles when being confined between charged surfaces.

1.2 Outline of the thesis

The thesis starts with a scientific background to the relevant fields in chapter 2. An overview of various types of colloidal dispersions is given, including basic concepts of self-assembly and colloidal structure. State of the art understanding of surface forces is explained, starting with a general definition of common terms in surface science. Different types of forces, inside and outside the well established DLVO framework,

are reviewed.

Detailed experimental procedures are given in chapter 3. The two major techniques used throughout this work, atomic force microscopy and small-angle neutron scattering, are reviewed extensively including the fundamental principles of the respective technique. For additional techniques only the experimental details are given.

Most studies have focused on investigating the effect of the dispersions' properties on oscillatory structural forces. In chapter 4, the inverse problem is considered in so far, as the oscillatory structural force is used as a tool for characterisation of colloidal particles. Diameters of silica nanoparticles are determined by measuring the oscillatory structural forces across their corresponding colloidal suspensions. A limit of the inverse cubic root scaling law for charged particles is defined.

Chapter 5 reports on oscillatory structural forces across micellar dispersions. Special focus is drawn onto the influence of the micellar surface charge on the oscillatory structural forces. The surface charge is varied by different mixing ratios of nonionic and anionic surfactants. First, the bulk nanostructure of the micelles is probed by small-angle neutron scattering. The micellar structure is then compared with oscillatory structural forces across these dispersions, as measured by colloidal-probe atomic force microscopy.

Chapter 6 describes the combination of oscillatory structural forces with other surface forces. A superposition of double layer and structural forces is explored for the interaction of charged silica surfaces across suspensions containing charged nanoparticles and monovalent salt. A complete description of the interaction from a few hundred nanometers down to the surfaces almost being in contact is achieved.

The thesis is concluded in chapter 7. The results from this work are shortly summarised and put in context to each other. Finally, a personal opinion on potential future perspectives for this research field is given.

2 Scientific background

2.1 Colloidal dispersions

Colloidal systems are two-phase dispersions, uniform on the macroscopic but not on the microscopic scale. Unlike a solution, where solute and solvent comprise only one single phase, a colloidal dispersion is characterised by a continuous (outer) phase and a dispersed (inner) phase. The constituents of the dispersed phase have dimensions of around 1 nm to 1 µm, often called the mesoscopic scale. Different kinds of colloidal dispersions can be formed, see examples in Table 2.1.

Continuous phase	Dispersed phase	Term	Examples
Gas	Liquid	Aerosol	Clouds, fog, hairspray
	Solid	Aerosol	Smoke, dust, pollen
Liquid	Gas	Foam	Whipped cream, foam on beer
	Liquid	Emulsion	Milk, mayonnaise, skin creams
	Solid	Sol, suspension$^{(a)}$	Inks, paints
Solid	Gas	Porous solid$^{(b)}$	Pressed powders
		Solid foam	Insulating foams, soufflé
	Liquid	Solid emulsion	Bituminous road paving, butter
	Solid	Solid suspension	Concrete, some alloys

Table 2.1: Different types of colloidal dispersions with some common examples;
$^{(a)}$ The term "suspension" is the generic term and may include dispersed phases with dimensions $> 1\mu m$. For a more accurate definition the term "colloidal suspension" is recommended;
$^{(b)}$ Porous solids have a bicontinuous structure while in a solid foam the gas phase is dispersed. (adapted from [11, 12])

An important feature of all colloidal dispersions is that the internal contact area between the dispersed and continuous phase is relatively large. The area of contact is typically called interface. The term surface is often used as a synonym, although an interface is by definition the area where two explicitly named condensed phases meet (*e.g.* the solid-liquid interface but the solid surface). The energy associated with these interfaces is significant, and its study is an integral part of colloidal science.

2.1.1 Self-assembly and micelles

An interesting class of colloidal dispersions are self-assembled systems. Here, the field of **surf**ace **act**ive **a**ge**nts** (surfactants) and their ability to self-assemble into association colloids, *i.e.* structures of mesoscopic length scales is reviewed. Surfactants are the prototype of amphiphilic molecules, possessing a water-soluble (hydrophilic) and a water-insoluble (hydrophobic) part. The hydrophobic part is typically composed of one or more alkyl chains, which are linear or branched. The length of the alkyl chain is mostly in the range of eight to twenty carbon atoms (C_8 - C_{20}). Surfactants are primarily defined by the nature of their polar headgroup. It can be divided into two parts: nonionic versus ionic. For ionic surfactants, the classification can be further divided into cationic, anionic, or zwitterionic.

When dissolved in water, surfactants will preferably accumulate at the air-water interface. The insoluble hydrophobic group extends out of the bulk water phase towards air while the water-soluble headgroup remains in the water phase. Once the air-water interface is completely decorated with surfactants, they will self-assemble into aggregates, called **micelles** in order to minimise the free energy of the system. This self-assembly process starts once the surfactant concentration in bulk exceeds the critical micelle concentration (*cmc*). An aggregation number (N_{agg}) defines the number of surfactants per micelle. Often aggregation numbers range from 50 - 100 surfactants per micelle [11, 13]. The *cmc* can be determined measuring physico-chemical properties of the solution, such as its surface tension or electrolytic conductivity.

Properties of micelles, such as their size and shape, are typically defined by the length, branching and number of hydrophobic chains as well as by the size and nature of the polar headgroup. The concept of the spontaneous packing parameter p_0 [14] quantifies the preferred geometry of a surfactant and its self-assembled structures. The ratio

between apolar and polar surface of a single surfactant molecule is defined depending on the length l_c and the volume v_c of the apolar alkyl chain, as well as the effective area of the headgroup a_0.

$$p_0 = \frac{v_c}{l_c\, a_0} \tag{2.1}$$

In general, the spontaneous packing parameter p_0 of a surfactant molecule governs the curvature of the resulting self-assembly. The packing parameter p_0 is small ($< 1/3$) for *e.g.* ionic surfactants with one aliphatic chain or nonionic surfactants with large headgroups. To maximise the ratio of polar to apolar surface, spherical micelles are formed. If the surfactants consist of two aliphatic chains (*e.g.* in phospholipids), p_0 increases to a value of ≈ 1 leading to the formation of almost planar interfaces and bilayer structures.

2.1.2 Structure of concentrated colloidal dispersions

This work focusses on the influence of the nanostructure of colloidal dispersions on the interactions across such fluids. Colloidal dispersions are considered as concentrated, once its properties are influenced by the interactions between the colloidal particles. A theoretical framework for the description of a fluid structure already exists in the field of liquid state physics [15, 16]. Equations of statistical mechanics are used to describe fluid properties. It is possible to transfer these equations of statistical mechanics to colloidal dispersions by treating the colloidal particles similar to solvent molecules in simple liquids.

The spatial arrangement of colloidal particles is schematically illustrated in Fig. 2.1 (a). A quantitative measure of the static local structure is given by the radial (or pair) distribution function $g(r)$, which describes the local density $\rho(r)$ around a given particle as a function of the distance r from the centre of the particle. In other words, it is the probability of finding a particle at the radial distance r, where the origin is defined as the centre of a particle. A common feature of the $g(r)$ function is that it is zero at short distances, since the particles do not penetrate each other. At large distances $g(r)$ approaches 1, meaning that the local particle density $\rho g(r)$ approaches the bulk density ρ.

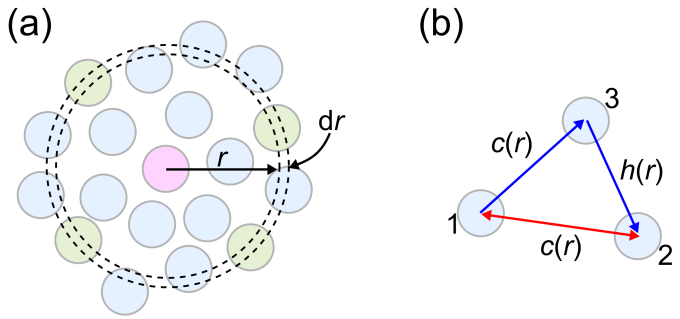

Figure 2.1: (a) Schematical representation of the spatial arrangement of colloidal particles and the definition of $g(r)$; (b) Contributions to the total correlation function $h(r)$ between two particles ($1 \leftrightarrow 2$) as described by the Ornstein-Zernike integral equation

The determination of $g(r)$ is directly related to the change in free energy $U(r)$ by bringing two particles from infinite separation to a separation r. In very dilute systems $U(r)$ is simply the interaction potential between two individual particles (similar to ideal gases).

In liquid systems, however, $U(r)$ is also often called the potential of mean forces, since it contains contributions from many-body interactions, which also become important at higher concentrations of colloidal particles.

$$g(r) = \exp\left(-\frac{U(r)}{kT}\right) \tag{2.2}$$

Possible solutions of $g(r)$ are based on the assumptions that the correlation between particles contains direct and indirect effects. A total correlation function $h(r)$ between two particles is directly connected to $g(r)$.

$$h(r) = g(r) - 1 \tag{2.3}$$

Given the picture in Fig. 2.1 (b), the total correlation consists of two contributions: a direct correlation between particle 1 and 2, characterised by the direct correlation function $c(r)$ and an indirect part, which is the influence of particle 1 on particle 3, which in turn affects particle 2, directly and indirectly. The indirect part contains the direct correlations $c(r)$ between particle 1 and 3 multiplied by the total correlation function

$h(r)$ between particle 2 and 3. The final result has to be multiplied over all possible positions of the third particle. This way, one obtains the Ornstein-Zernike (OZ) integral equation that provides the connection between $h(r)$ and $c(r)$ [15, 16] knowing the particle number density n_p.

$$h(|\vec{r_1} - \vec{r_2}|) = c(|\vec{r_1} - \vec{r_2}|) + n_p \int \mathrm{d}\vec{r_3} c(|\vec{r_1} - \vec{r_3}|) h(|\vec{r_2} - \vec{r_3}|) \tag{2.4}$$

Since this integral equation contains two unknown parameter, $h(r)$ and $c(r)$, it can only be solved if a so-called closure-relation is added. Various closure-relations were introduced. Here, two closure-relations are discussed in detail since they provide analytical solutions to the integral equations: the Percus-Yevick and the Mean Spherical Approximation.

The Percus-Yevick (PY) closure-relation is used when the particles (with diameters d) interact only via a hard-sphere potential [17]. Following closure-relation is used:

$$g(r) = \exp\left(-\frac{U(r)}{kT}\right)[g(r) - c(r)] \tag{2.5}$$

$$U(r) = \begin{cases} \infty, & r < d \\ 0, & r \geq d. \end{cases} \tag{2.6}$$

When the particles are charged, they are assumed to interact via a screened Coulomb potential. In this case, the mean spherical approximation (MSA) is used [18]. Its closure-relation reads as:

$$\begin{aligned} h(r) &= -1, \quad r < d \\ c(r) &= -\frac{U(r)}{kT}, \quad r \geq d. \end{aligned} \tag{2.7}$$

An interesting feature in using these two closure-relations is that for small surface charges or high screening, the MSA yields the PY result. Often different closure-relations yield slightly different results.

These analytic results of the OZ integral equation provide the formal framework to analyse scattering experiments on colloids. The structure of colloidal dispersions is

often defined by the static structure factor $S(q)$ which is experimentally accessible by scattering experiments. $S(q)$ is the spatial Fourier transform of $g(r)$ [11, 15].

$$S(q) = 1 + n_p \int_v g(r) \exp\left(i\vec{q}\vec{r}\right) \mathrm{d}\vec{r} \tag{2.8}$$

The integration is over the volume v of the dispersion. For isotropic scattering, following relationship is established [19]:

$$S(q) = 1 + n_p\, 4\pi \int_0^\infty [g(r) - 1] \frac{\sin(qr)}{qr} r^2 \mathrm{d}r. \tag{2.9}$$

As a result, the static structure factor $S(q)$ is used for description of the colloidal bulk structure. $S(q)$ depends on the scattering vector q. Further description and analysis of the structure factor $S(q)$ is carried out in the experimental section (chapter 3), and in chapter 5, where small-angle neutron scattering is used to determine the structure in concentrated micellar dispersions.

2.2 Surface forces

The following section provides an introduction to surface and interfacial forces. In the following, only the more general term "surface forces" will be used.

2.2.1 General introduction

Definition of different physical properties In colloidal science, equations defining surface forces are typically derived for the situation of interacting planar, semi-infinite surfaces. The surface separation is in the following defined as h. Using these notation, it is important to recall different properties, namely the interaction potential (free energy) $U(h)$, the force $F(h)$, the interaction potential per unit area (surface energy) $W(h)$ and the disjoining pressure $\Pi(h)$.

The force $F(h)$ is related to the interaction potential $U(h)$ as its negative derivative:

$$F(h) = -\frac{\mathrm{d}U(h)}{\mathrm{d}h}. \tag{2.10}$$

The surface energy $W(h)$ is the interaction potential $U(h)$ per unit area a:

$$W(h) = \frac{U(h)}{a}. \tag{2.11}$$

The surface energy $W(h)$ and with that the force $F(h)$ per unit area a is related to the disjoining pressure $\Pi(h)$:

$$\Pi(h) = -\frac{\mathrm{d}W(h)}{\mathrm{d}h} = \frac{F(h)}{a}. \tag{2.12}$$

Derjaguin approximation Based on the work of Derjaguin [20], it is possible to estimate the force $F(h)$ between different finite sized objects with various geometries from the surface energy $W(h)$ between two planar, semi-infinte walls. This approximation is nowadays widely known as Derjaguin approximation and serves as a fundamental basis in the field of colloidal science.

$$F(h) = 2\pi R_{\mathrm{eff}} W(h) \tag{2.13}$$

The effective radius R_{eff} accounts for the geometry of the interacting bodies. When two spheres with radii R_1 and R_2 interact with each other, the effective radius can be expressed as:

$$R_{\mathrm{eff}}^{-1} = R_1^{-1} + R_2^{-1}. \tag{2.14}$$

In this work, the Derjaguin approximation is used to normalise the force between a planar wall and a sphere. In this case, one radius is assumed infinite, and the effective radius equals the radius of the sphere.

$$R_{\mathrm{eff}} = R \tag{2.15}$$

It has to be noted, that this approximation remains valid as long as $h \ll R_1$, R_2. Due to this approximation, experimentally measured force profiles are typically reported as the ratio of the measured force and the effective radius $F(h)/R_{\text{eff}}$.

DLVO-theory Surface interactions are usually described by the classical theory of Derjaguin, Landau, Verwey, and Overbeek (DLVO-theory) [21, 22]. The DLVO-theory assumes the interaction energy between two charged surfaces by means of two additive contributions, namely the van der Waals interactions W_{vdW} and the double layer interactions W_{dl}.

$$W_{\text{DLVO}}(h) = W_{\text{vdW}}(h) + W_{\text{dl}}(h) \tag{2.16}$$

The following sections summarise surface interactions, that can either be part of or can be outside the DLVO theory. First of all the surface energies $W(h)$ will be derived assuming two planar, semi-infinite walls. The force acting between to finite sized objects $F(h)$ is then calculated using the Derjaguin approximation. The obtained equations will be presented as $F(h)/R_{\text{eff}}$, since this value is typically available from force measurements.

2.2.2 Van der Waals forces

The term van der Waals (vdW) forces includes the sum of three different contributions between individual molecules:

- Between two permanent dipoles (Keesom interaction)
- Between a permanent dipole and an induced dipole (Debye interaction)
- Between two induced dipoles (London dispersion interaction)

Although of different physical origin, they obtain the same dependency on the intermolecular distance h. They can be summarised in the general form of the vdW interaction $U(h)_{\text{vdW}}$.

$$U_{\text{vdW}}(h) = -\frac{C_{\text{Keesom}} + C_{\text{Debye}} + C_{\text{London}}}{h^6} = -\frac{C}{h^6} \tag{2.17}$$

Here, C acts as the scaling factor of the individual interaction contributions. Eqn. 2.17 reveals a very short ranged vdW interaction between molecules ($U(h) \propto h^{-6}$).

In the case of interacting macroscopic bodies, however, this relation expands to a many-body problem. Hamaker proposed the net interaction energy between two surfaces $W(h)$ as the integration of all pair contributions between molecules in two bodies with volumes v_1 and v_2 [23].

$$W_{\mathrm{vdW}}(h) = -\int_{v_1}\int_{v_2} \rho_1\rho_2 \frac{C}{h^6} dv_1 dv_2 \tag{2.18}$$

ρ_1 and ρ_2 are the molecular densities in the respective volumes. Although the integration can be solved for various geometries, the following will focus on the interaction between two planar, semi-infinite walls. The resulting Hamaker constant A_H summarises different properties and determines the strength of the vdW force.

$$W_{\mathrm{vdW}}(h) = -\frac{\pi\rho_1\rho_2 C}{12h^2} = -\frac{A_H}{12\pi h^2}, \quad \text{with } A_H = \pi^2 C\rho_1\rho_2 \tag{2.19}$$

The case for interacting spheres can also be solved analytically. Since the interaction energy for two planar walls was already determined, the Derjaguin approximation (eqn. 2.13) is used to directly display the van der Waals force between two interacting bodies using the effective radius R_{eff}.

$$\frac{F_{\mathrm{vdW}}}{R_{\mathrm{eff}}}(h) = -\frac{A_H}{6h^2} \tag{2.20}$$

It is important to mention that the interaction is significantly longer ranged for interacting macroscopic bodies ($U(h) \propto h^{-2}$ for two planar, semi-infinite walls) compared to the one obtained for individual molecules. The exact scaling factor as well as the distance scaling law depends on the geometry of the interacting surfaces.

The pairwise additivity of molecular contributions, as proposed by Hamaker, is typically not fulfilled, since neighbouring molecules might effect the polarisability, especially in condensed materials. Based on the theory of Lifshitz a general quantitative description of van der Waals forces was introduced [24]. This theory treats the macroscopic bodies as a continuum and the Hamaker constants can be derived from

dielectric properties. Although, the derived Hamaker constants differ from the original Hamaker approach, the distance dependence of the force remains the same.

So far, the vdW interactions are only described across vacuum. The Hamaker constant for the more relevant case, two bodies interacting through a medium, can also be derived. An important result is that vdW interactions are always attractive between surfaces of the same material, while it can be repulsive for dissimilar materials. An important example of repulsive vdW interactions is an air bubble interacting with a glass surface across water [25].

2.2.3 Double layer forces

This section is divided into two paragraphs. First, the chemical origins of charges and the formation of an electrical double layer next to an individual surface are explained. Second, the double layer force is described, which emerges when the double layers of two surfaces overlap.

The electrical double layer When a surface is exposed to a polar medium (most importantly water), it is typically charged. Basically, there are three different mechanisms that generate charged surfaces:

- The surface consisting of intrinsically charged units (*e.g.* clay surfaces containing negatively charged aluminate groups)
- Ionisation or dissociation of surface groups (*e.g.* of surfaces with titrable groups, such as $-NH_3$, $-COOH$, or $-OH$)
- Adsorption or binding of ions onto the surface (*e.g.* fatty acids and surfactants onto apolar surfaces, or large inorganic ions such as I^-, ClO_4^-, or SCN^-)

The most common mechanism in colloidal science is the formation of surface charges through ionisation or dissociation of surface groups. In this situation, the surface charge can be altered by the properties of the solution, such as its pH-value or the concentration of electrolyte.

A charged surface causes an electric field in the medium which will alter the distribution of ions next to the surface. The charged surface together with the adjacent layer with altered distribution of ions in solution is called electrical double layer (EDL).

An early and simple description of the EDL was proposed by Helmholtz [26]. It assumes the counterions to directly bind onto the surface and neutralise the surface charges. Although some basic features of charged surfaces could be explained, the model failed to describe the capacitance of an EDL. Gouy and Chapman observed that the capacitance of the EDL depends on ion concentration and surface potential [27, 28]. By introducing the so-called diffuse layer they took into account the thermal motion of the ions. Stern then combined both models to what is today defined as the Gouy-Chapman-Stern model (Fig. 2.2) [29].

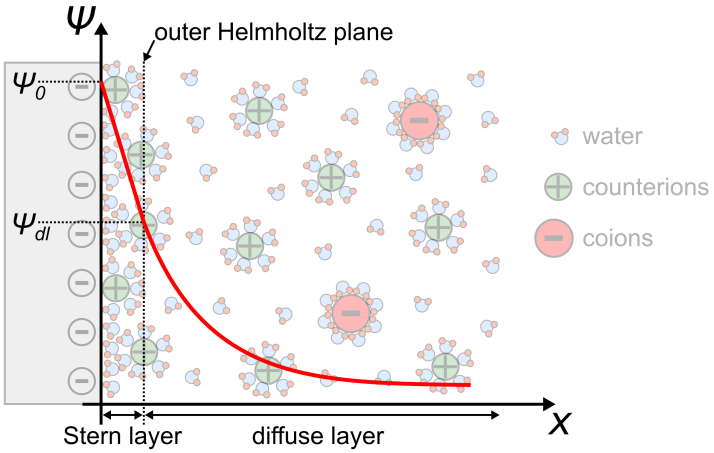

Figure 2.2: Gouy-Chapman-Stern model of the electrical double layer. Distribution of hydrated ions in the Stern and diffuse layer is shown together with the surface potential profile as a function of the distance from the charged surface $\psi(x)$ (red line). (adapted from [12, 13, 30, 31])

This model is typically applied for the description of the EDL and divides it into two regions: when a charged surface is in contact with an electrolyte solution, some ions may adsorb onto the surface, either directly or including their hydration shell, forming a layer of immobile ions (called Stern layer). The distance between the surface and the centres of the hydrated ions marks the so-called outer Helmholtz plane. At distances beyond the outer Helmholtz plane, the diffuse layer emerges where the ions in solution distribute in response to the surface potential.

The Poisson-Boltzmann theory The Poisson-Boltzmann (PB) theory provides a way to calculate the potential profile of the EDL, *i.e.* the potential as a function of distance from the surface $\psi(x)$ (see red line in Fig. 2.2). Assuming a charged planar surface, the Poisson equation generally expresses the surface potential ψ as a function of the normal distance to the surface x via the charge density ρ.

$$\frac{\mathrm{d}^2\psi}{\mathrm{d}x^2} = -\frac{\rho}{\epsilon\epsilon_0}, \tag{2.21}$$

where ϵ is the dielectric constant of water, and ϵ_0 is the dielectric permittivity of vacuum. Note that the distribution of the immobile ions in the Stern layer is not described by the PB theory. Although the following equations are general descriptions, the potential at the origin of the diffuse layer ψ_{dl} (which is equal to the potential at the outer Helmholtz plane) is considered as surface potential (with $\psi_{\mathrm{dl}} = \psi(x = 0)$) from here on*. The distribution of ions next to a charged surface will be altered by its bulk concentration $c_{i,\infty}$ according to Maxwell-Boltzmann statistics [32]. The charge density ρ in the diffuse layer can be calculated from the sum of all ionic species in the diffuse layer that are influenced by the diffuse layer potential ψ_{dl}.

$$\rho = e\sum_i z_i c_{i,\infty} \exp\left(-\frac{z_i e\psi(x)}{kT}\right), \tag{2.22}$$

with e is the elementary charge, z the ion valency, k is the Boltzmann constant, and T is the temperature. Combining equations 2.21 and 2.22 yields the Poisson-Boltzmann (PB) equation:

$$\frac{\mathrm{d}^2\psi}{\mathrm{d}x^2} = -\frac{e}{\epsilon_0\epsilon}\sum_i z_i c_{i,\infty} \exp\left(-\frac{z_i e\psi(x)}{kT}\right). \tag{2.23}$$

Analytical solution of the PB-equation Eqn. 2.23 can be analytically solved for symmetric z:z electrolytes. This is often called full one-dimensional case. One obtaines

*Note that the index "dl" is used simultaneously for the diffuse layer potential ψ_{dl} and the double layer force F_{dl} to remain consistent with other literature.

[13, 33]:

$$\tanh\left(\frac{ze\psi(x)}{4kT}\right) = \tanh\left(\frac{ze\psi_{\mathrm{dl}}}{4kT}\right)\exp(-\kappa x). \tag{2.24}$$

Considering the potential profile $\psi(x)$ without close proximity to the surface, one can approximate $\tanh(x) \approx x$ in the first term and obtains:

$$\psi(x) = \frac{4kT}{ze}\tanh\left(\frac{ze\psi_{\mathrm{dl}}}{4kT}\right)\exp(-\kappa x). \tag{2.25}$$

The absolute potential decreases with increasing distance x from the surface (as indicated in Fig. 2.2). This decrease follows a negative exponential decay with a decay length of κ^{-1}, also known as the Debye length.

$$\kappa^{-1} = \left(\frac{\epsilon_0\epsilon kT}{\sum z_i^2 c_{i,\infty} e^2}\right)^{1/2} = \left(\frac{\epsilon_0\epsilon kT}{2e^2 N_A I}\right)^{1/2} \tag{2.26}$$

The Debye length κ^{-1} only depends on the ion concentration in the electrolyte solution (N_{A} is the Avogadro constant). This is described by the ionic strength I, which is calculated from the valency z_i and concentrations c_i of all ionic species in solution.

$$I = \frac{1}{2}\sum_i z_i^2 c_{i,\infty} \tag{2.27}$$

The surface charge can be calculated from the assumption that the total charge in the diffuse layer represents the charge needed to neutralise the surface charge at the outer Helmholtz plane, due to electroneutrality. The resulting surface charge density σ_{dl} calculates from the diffuse layer potential ψ_{dl} using the Grahame equation [13, 33].

$$\sigma_{\mathrm{dl}} = -\int_0^\infty \rho \mathrm{d}x = -\epsilon_0\epsilon\frac{\mathrm{d}\psi}{\mathrm{d}x} = \frac{2kT\epsilon_0\epsilon\kappa}{ze}\sinh\left(\frac{ze\psi_{\mathrm{dl}}}{2kT}\right) \tag{2.28}$$

Debye-Hückel approximation In the case for low surface potentials ($\psi_{dl} \leq 25\,\mathrm{mV} \rightarrow |z_i e\psi| \ll kT$), the PB equation (eqn. 2.23) can be linearised, by expanding the exponential function into a series ($\exp(x) = 1 + x + x^2/2! + ...$) and neglect all but the the first linear term. This linearisation is called Debye-Hückel (DH) approximation [13, 30]. The approximation yields the surface potential profile as:

$$\psi(x) = \psi_{dl} \exp(-\kappa x) \tag{2.29}$$

and the surface charge density as:

$$\sigma_{dl} = \epsilon\epsilon_0 \kappa \psi_{dl}. \tag{2.30}$$

Limitations of the PB-theory The PB theory is a mean-field theory that applies assumptions to approximate the diffuse layer potential. These assumptions include the treatment of the ions as point charges and the solvent permittivity as constant. Moreover, surfaces are assumed to be ideally smooth with a homogeneous charge distribution. The PB theory has to be modified, *e.g.* when the ions gather a considerable volume and start to correlate [34], especially when anions and cations start to form ion pairs [35]. An ongoing debate concerns the modelling of colloidal particles with regard to the PB theory. This topic is addressed in chapter 6.

The double layer force The above equations describe the case of a single charged surface in solution. When two charged surfaces approach each other and the electrical double layers overlap, an (electrostatic) double-layer force F_{dl} arises*. The counterions of the respective double layers are forced to stay within the vicinity between the two surfaces. This originates a disjoining pressure Π due to an osmotic pressure difference between the vicinity and the bulk liquid. Please note that the double layer force is fundamentally different from the Coulomb force. The double layer force is due to an osmotic pressure caused by gains in entropy.

This section focuses on the description of the double layer force between two identical, parallel surfaces. In this situation, the symmetry of the potential profile can be used to

*Note that the index "dl" is used simultaneously for the diffuse layer potential ψ_{dl} and the double layer force F_{dl} to remain consistent with other literature.

simplify calculations. Following assumptions are made: the surface potentials ψ_{dl} are identical for both surfaces. Between the surfaces, the potential decreases. In the center of the gap, the so-called midplane at x_m, the gradient in surface potential must be zero, due to symmetry.

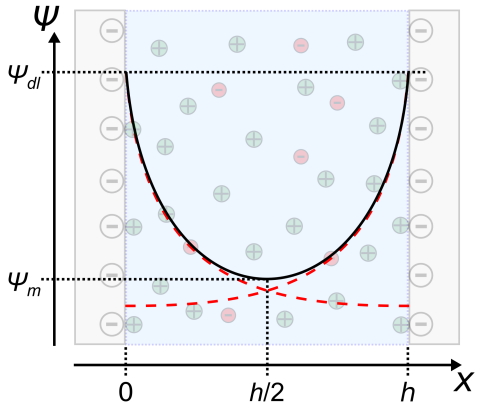

Figure 2.3: Potential distribution across equally charged surfaces at a separation h. Using the superposition approximation, the potential at the midplane ψ_m is calculated as twice the potential of an unperturbed surface at the midplane $\psi'(\frac{h}{2})$. (adapted from [12, 13])

The disjoining pressure Π_{dl} between the two surfaces is, for this specific case, given by the osmotic pressure difference between the midplane and the surrounding bulk.

$$\Pi_{\mathrm{dl}} = \Pi_{\mathrm{osm}}(x_m) - \Pi_{\mathrm{osm}}(\mathrm{bulk}) = kT \sum_i c_{i,\infty} \left(\exp\left(\frac{-z_i e \psi_m}{kT} \right) - 1 \right) \tag{2.31}$$

In the assumption of a weakly overlapping regime, where $|z_i e \psi_m| \ll kT$ the exponential can be written as a series ($\exp(x) = 1 + x + x^2/2! + ...$). In this case, the linearisation is called superposition approximation. Neglecting all terms higher than the quadratic one leads to the disjoining pressure $\Pi(h)$ from the potentials of the individual surfaces ψ'_{dl}.

$$\Pi_{\mathrm{dl}}(h) = \frac{\epsilon_0 \epsilon \kappa^2}{2} \psi_m^2, \quad \text{with} \quad \psi_m = 2\psi'_{\mathrm{dl}}(\frac{h}{2}) \tag{2.32}$$

Inserting the analytical solution of the PB equation (eqn. 2.25) into eqn. 2.32 yields:

$$\Pi_{\mathrm{dl}}(h) = 64 c_{i,\infty} kT\Gamma^2 \exp(-\kappa h), \quad \text{with } \Gamma = \tanh\left(\frac{ze\psi_{\mathrm{dl}}}{4kT}\right) \tag{2.33}$$

$$W_{\mathrm{dl}}(h) = -\int_{\infty}^{h} \Pi(h')\mathrm{d}h' = 64 c_{i,\infty} kT\kappa^{-1}\Gamma^2 \exp(-\kappa h) \tag{2.34}$$

$$\frac{F_{\mathrm{dl}}}{R_{\mathrm{eff}}}(h) = 128\pi c_{i,\infty} kT\kappa^{-1}\Gamma^2 \exp(-\kappa h). \tag{2.35}$$

In case of low surface potentials ($\psi_{\mathrm{dl}} \leq 25\,\mathrm{mV}$) the DH approximation (eqn. 2.29) can be consulted again for the calculation of the disjoining pressure Π_{dl} (eqn. 2.32):

$$\Pi_{\mathrm{dl}}(h) = 2\epsilon_0\epsilon\kappa^2\psi_{\mathrm{dl}}^2 \exp(-\kappa h) \tag{2.36}$$

$$W_{\mathrm{dl}}(h) = -\int_{\infty}^{h} \Pi(h')\mathrm{d}h' = 2\epsilon_0\epsilon\kappa\psi_{\mathrm{dl}}^2 \exp(-\kappa h) \tag{2.37}$$

$$\frac{F_{\mathrm{dl}}}{R_{\mathrm{eff}}}(h) = 4\pi\epsilon_0\epsilon\kappa\psi_{\mathrm{dl}}^2 \exp(-\kappa h). \tag{2.38}$$

Limitations of the superposition approximation The above expressions are obtained using the superposition approximation. It treats the potential profiles of both surfaces as additive and assumes that they do not affect each other. It describes the situation at large surface separations well, but is not accurate at small surface separations. At some point, the overlap of the two double layers will alter their structures. Two boundary conditions were defined: either the charge in the Stern layer remains constant (constant charge approximation) or the diffuse layer potential remains constant (constant potential approximation). In reality overlap of the double layers may induce ions to adsorb on the surface, changing both the surface charge and potential. This effect is summarised as charge regulation [36–38].

2.2.4 Oscillatory forces

Parts of this section are published in "Recent progress in measurements of oscillatory forces and liquid properties under confinement", Michael Ludwig and Regine von Klitzing, *Curr. Opin. Colloid Interface Sci.*, **2020**, 47, 137-152. [39] doi:10.1016/j.cocis.2020.02.002

Forces described by the DLVO theory treat the liquid between the surfaces as a continuum. In reality, a discrete structuring between *e.g.* solvent molecules or dispersed colloidal particles occurs that will also influence surface interactions across fluids. The DLVO theory fails to describe surface interactions at length scales at which a pronounced structuring occurs. The bulk structuring of colloidal dispersions is introduced in section 2.1.2. There, the radial distribution function $g(r)$ is defined as the probability of finding a particle in radial distance to the center of another particle. This is closely related to the issue in this section, where the probability of finding a particle perpendicular to a macroscopic surface is considered.

First, a general introduction for the cases of simple liquids, *i.e.* liquids consisting of only one component (mainly solvent molecules), is given. Looking at closer distances x, the particle density ρ deviates from their mean bulk value due to short range correlations. Next to a macroscopic surface, the particle density fluctuations are most pronounced via the formation of layered structures (often called interfacial region). This can be modelled using a damped oscillatory profile (Fig. 2.4 (a)) perpendicular to the surface. When the liquid is confined between two surfaces, interference of the interfacial regions is observed (Fig. 2.4 (b)).

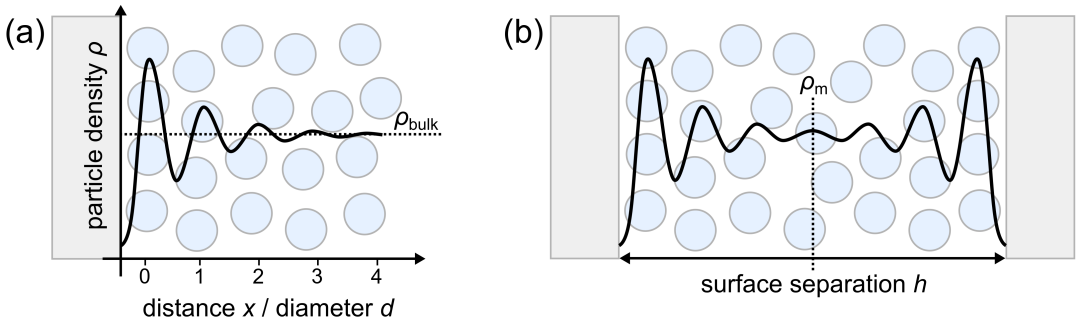

Figure 2.4: Schematic representation of a particle density profile (a) next to a single surface, and (b) between two confining surfaces. (adapted from [13, 33])

When comparing the particle density at the midplane ρ_m at infinitely separated surfaces, the midplane particle density is equal to the bulk particle density: $\rho_m(\infty) = \rho_\infty$. At approaching surfaces, the particle density at the midplane will change as a function of surface separation h. The difference in particle density is responsible for an oscillatory disjoining pressure Π_{osc} that applies to the surfaces:

$$\Pi_{osc}(h) = kT\left(\rho_m(\frac{h}{2}) - \rho_m(\infty)\right). \tag{2.39}$$

When the surface separation h is a multiple integer (n) of the particle diameter d ($h = n\,d$), optimal arrangement of the particles can be achieved and with that a maximum in pressure (Fig. 2.5 (b), (d), (f)). At surface separations between ($h = (n + 0.5)\,d$), packing problems occur and with that a minimum in pressure (Fig. 2.5 (c), (e), (g)). This leads to alternating repulsive and attractive forces with respect to the separation of the surfaces.

At even closer surface separations no particles are present between the confining surfaces (Fig. 2.5 (a)). There, the disjoining pressure Π simply relates to the bulk particle density ρ_∞ as:

$$\Pi_{osc}(h \to 0) = -kT\rho_\infty. \tag{2.40}$$

The force versus separation profile can be fitted via the well-known oscillatory exponential decaying force profile, as introduced by Horn and Israelachvili [40].

$$\frac{F_{osc}}{R_{eff}}(h) = -A \cdot \exp\left(-\frac{h}{\xi}\right) \cdot \cos\left(\frac{2\pi}{\lambda}(h - h')\right) \tag{2.41}$$

In equation 2.41, four fitting parameters are present. The amplitude A corresponds to the strength of the oscillatory force. The correlation length ξ indicates the interaction range away from the confining surfaces. The wavelength λ is the period of the force versus separation profile. The offset h' corrects for the position of the force oscillations.

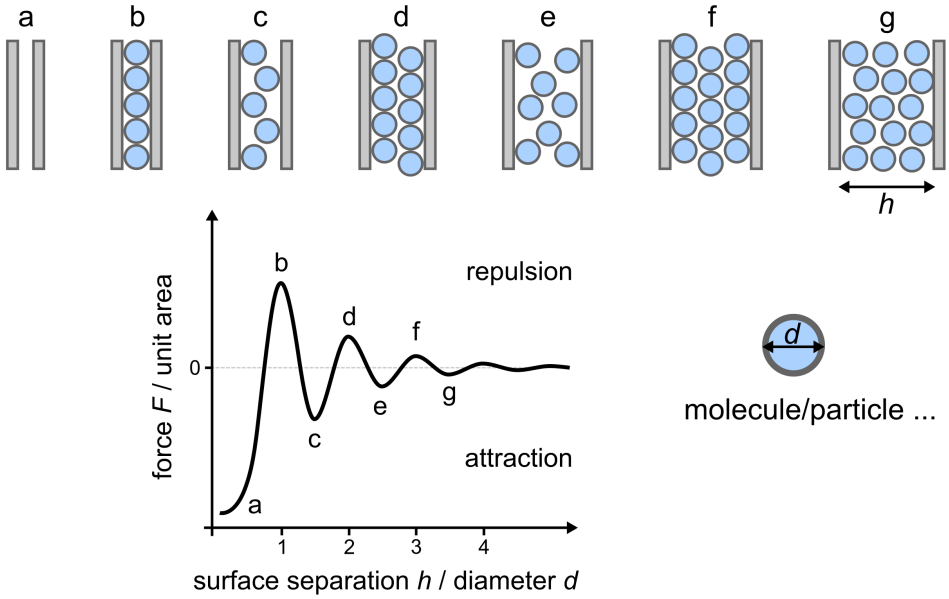

Figure 2.5: Schematic drawing of a liquid confined between two walls. The liquid structuring changes depending on the surface separation h. This results in an oscillating force versus separation profile. The maximum force F per unit area is achieved at surface separations of multiple diameters of the liquids predominant structure. (adapted from [12, 13, 33])

Fig. 2.6 shows a schematic overview of different systems inducing oscillatory forces. They are viewed and characterised as (pseudo) one-component or two-component systems. Similar to section 2.1.2, the equations derived for simple liquids (one-component systems) are transferred to colloidal dispersions (two-component systems).

One-component systems In the context of simple liquids, oscillatory forces are typically called **solvation forces**. The first measurement of solvation forces was realised across a nonpolar liquid, namely octamethylcyclotetrasiloxane (OMCTS) [40]. OMCTS has developed to the most commonly studied liquid for oscillatory forces, due to its properties as a cyclic siloxane forming well defined layers [41, 42]. Also the structure and orientation of other nonpolar liquids [43–45], water [46, 47] and alcohols were measured [48, 49]. Furthermore, liquid crystals were characterised [50]. For liquid crystals also other fitting formulas (unlike eqn. 2.41) were developed based on the work of de Gennes [51].

Similar force versus separation profiles are obtained for measurements of ionic liquids

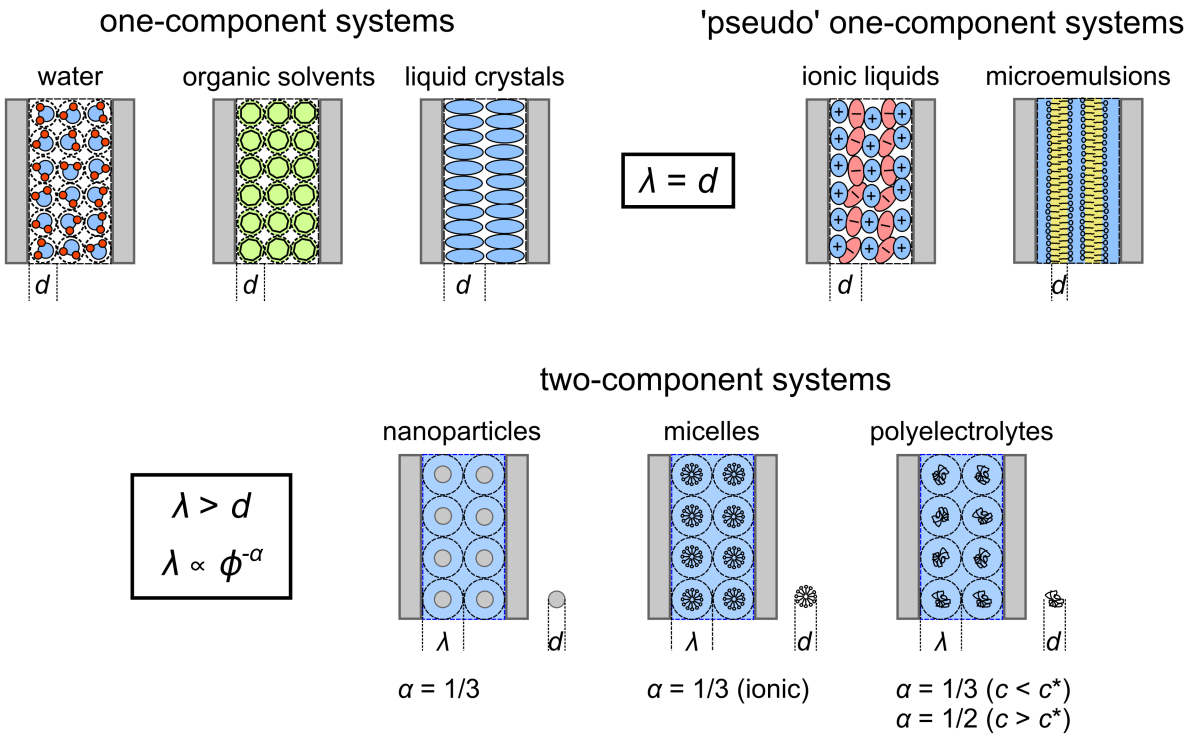

Figure 2.6: Schematical overview of different systems inducing oscillatory forces. For polyelectrolyte systems, c^* denotes threshold concentration between the dilute - semi dilute regime.

(ILs) and microemulsions (MEs) [52–55]. Rather than fitting the force profiles in these systems, often only the wavelength λ is determined. The investigation of ILs emerged in recent years, due to the possible industrial use. In this context the oscillatory force is sometimes called structural force, although this classification should only be used in cases of two-component sytems. Special focus was set on manipulation of the ILs' surface nanostructure with applied surface potential [56]. Interested readers are guided to more detailed review articles on force spectroscopy of ILs [57, 58].

Although consisting of cations and anions - as for ILs - or different water and oil phases - as in MEs -, both are described as pseudo one-component liquids, since they share one feature with simple one-component systems: the oscillation wavelength λ in the force versus separation profile is equivalent to the dominant liquid structure d perpendicular to the confining surfaces.

$$\lambda = d \tag{2.42}$$

Therefore, the systems nanostructuring perpendicular to the confining surfaces is directly sensed and the dominant liquid length scale can be deduced from the force versus separation profile.

Two-component systems Oscillatory forces occur also in two-component systems, *i.e.* in colloidal dispersion. The well-known depletion attraction due to non-adsorbing polymers, as introduced by Asakura and Ooasawa marks the first evidence for oscillatory forces [59]. Depletion interactions were thoroughly studied ever since [60]. The pure depletion attraction is considered as the limiting case at low concentrations of non-adsorbing particles. Only the last attractive well is observed, similar to eqn. 2.40. For higher concentrations of dispersed particles, oscillatory forces occur [7, 61]. Therefore, the term oscillatory depletion force or simply **depletion force** is sometimes used. Due to the nature of depleting colloidal particles the term oscillatory colloidal forces is used, too. We define this type of force in the framework of **oscillatory structural forces**, since the dominating wavelength λ in the force versus separation profile is related to the bulk colloidal structure. This can be emphasised by a combination of direct force measurements and bulk scattering techniques [62, 63] and will be further discussed in the main part of this thesis.

Oscillatory structural forces in dispersions of charged colloidal particles were extensively studied for ionic micelles [64–71], polyelectrolytes [72–82] and solid nanoparticles [68, 83–89]. Experimental evidence for oscillatory structural forces in dispersions of uncharged particles is available for aqueous solutions of nonionic surfactants [90, 91] and latex particles [92, 93].

In two-component systems, the measured wavelength λ is typically larger than the actual particle diameter d. The particles do not touch each other and the picture given in Fig. 2.5 has to be modified by the introduction of an effective interaction diameter d_{eff}. Definition of the effective diameter will be discussed in chapter 4. The wavelength λ is sensitive to the concentration and, therefore, to the volume fraction ϕ of the dispersed phase. In dispersions of charged colloidal particles distinct scaling laws with a scaling-factor α are observed.

$$\lambda \propto \phi^{-\alpha} \tag{2.43}$$

The prominent **inverse cubic root scaling law**, with a scaling exponent of $\alpha = 1/3$ is observed in systems of charged spherical particles, such as silica nanoparticles and ionic micelles [68, 84, 87, 89]. In polyelectrolyte solutions the scaling exponent switches from $\alpha = 1/3$ when the concentration is in the dilute region, to $\alpha = 1/2$ once the concentration enters the semi-dilute region [79, 81]. The threshold concentration between dilute and semi-dilute regime is marked as c^* in Fig. 2.6. Experimental measurements of non-spherical systems are limited to a few examples. Solid ZnS nanorods with different aspect ratios were measured, however, no oscillations in the force versus separation profiles are observed [94]. Sphere-to-rod transitions in micellar dispersions were also detected [91, 95]. A distinct scaling exponent α, however, was not extracted for non-spherical systems experimentally.

The scaling behaviour is a result of a packing issue and was, therefore, found to be very robust against different parameters, such as the ionic strength of the dispersions [63] as well as against properties of the confining surfaces, such as its roughness [96], elasticity [97] or surface potential [98, 99]. A scaling exponent of $\alpha = 1/3$ is only obtained for dispersions of charged particles. For uncharged particles, the wavelength λ was found to be less dependent on the volume fraction ϕ [90, 91, 100, 101]. The general validity of the inverse cubic root scaling law with respect to the particles' surface charges will be a major point of discussion in chapter 5.

2.2.5 Other surface forces

Further contributions to surfaces forces are known. Despite all of these types of forces being interesting fields of study itself, they are out of scope of this thesis. Here, the investigations focus on DLVO-type and oscillatory forces. A few examples of other surface forces are listed in the following [11–13, 33]:

- Bridging attraction or steric repulsion between surfaces are observed when they contain adsorbed or covalently bound polymers, such as polymer brushes or polyelectrolyte multilayers.
- Kinetic effects become important at high approach velocities of two surfaces. Especially in very viscous liquids, hydrodynamic forces often play a significant role.

- Strong adhesive capillary forces are observed when liquid meniscii are formed between the contact area of two neighbouring particles. This must be taken into account when studying systems with large surface areas, such as powders.

3 Experimental section

3.1 Materials and sample preparation

3.1.1 Nanoparticle suspensions

Three types of colloidal silica nanoparticle (NP) suspensions (Ludox SM-30, Ludox HS-30 and Ludox TM-40, Sigma Aldrich, Germany) were used during the measurements. Ludox is a registered trademark of W.R. Grace & Co.-Conn. for discrete, spherical NPs of amorphous silica. The NPs differ in size, which is discussed in chapter 4. The NPs are dispersed in water, with sodium as counterions of the negatively charged surface groups. The original stock of NP suspension was dialysed in dialysis tubes (SnakeSkin, 3.5k MWCO, ThermoFisher, Germany) with ultrapure water (milliQ-grade, 18.2 MΩ cm resistivity, Merck, Germany) for ten days, with daily water exchange. This dialysis method (diffusion dialysis) is able to extract certain impurities, yet a considerable amount of counterions remains in solution [102]. After dialysis, the NP concentration was characterised by weighing the sample before and after drying (24 h at 80 °C and vacuum). The dialysed stock suspension was then diluted with ultrapure water (chapter 4) or with aqueous sodium chloride (NaCl, Suprapure 99.99, Merck, Germany) solutions (chapter 6) to achieve the desired concentrations assuming ideal mixing.

3.1.2 Micellar dispersions

Micellar dispersions are studied in chapter 5. The nonionic surfactants Tween20 (also known as polysorbate 20, Fig. 3.1 (a)) and BrijL23 ($C_{12}E_{23}$, previous brand name: Brij-35, Fig. 3.1 (b)) were purchased from Sigma Aldrich (Germany). The purity of both nonionic surfactants was analysed by mass spectrometry. Mass spectra of Tween20

(Fig. 5.10) reveal a mixture composed of two major products, a polysorbate monoester and isosorbide polyethoxylate (Fig. 5.11 and Table 5.2). The mass spectra of BrijL23 (Fig. 5.12) show only one major species, the alkyl polyethyleneoxide ether (Fig. 3.1 (b)). The anionic surfactant sodium dodecyl sulfate (SDS, ultrapure, Fig. 3.1 (c)) was purchased from PanReac AppliChem (Germany).

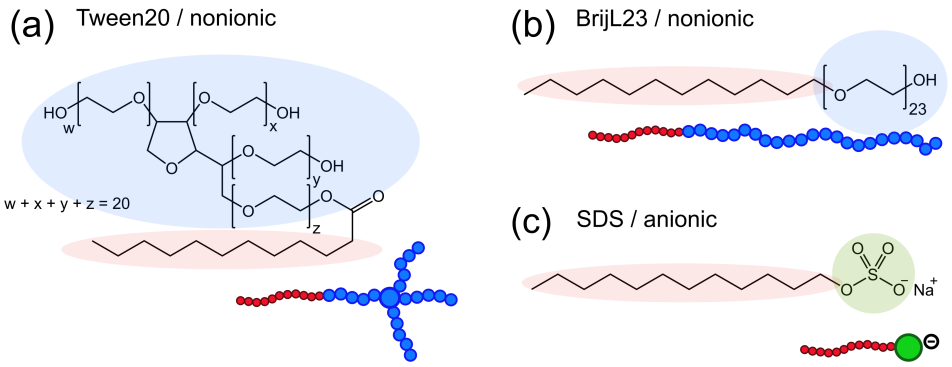

Figure 3.1: The molecular structures and schematic drawings of the surfactants used in this study: (a) nonionic Tween20, (b) nonionic BrijL23, and (c) anionic SDS. The hydrophobic alkyl chains are highlighted in red. The hydrophilic headgroups are highlighted in blue and green for nonionic EO groups and the anionic sulfate group, respectively.

Heavy water (D_2O, 99.9 atom% D) was purchased from Sigma Aldrich (Germany). For H_2O, ultrapure water (milliQ-grade, 18.2 MΩ cm resistivity, Merck, Germany) was used. All chemicals were used without further purification. Before use, all glassware was cleaned by soaking in aqueous Hellmanex III (Hellma Analytics, Germany) solution for at least one hour and rinsing with large amounts of water. The surfactant dispersions were prepared in D_2O for small-angle neutron scattering experiments and in H_2O for force measurements. The mixed surfactant systems were prepared by mixing Tween20 and SDS stock solutions. Four different mixing ratios of SDS and Tween20 were prepared. The mixing ratio X is defined as $X = [SDS] / ([SDS] + [Tween20])$. The composition ranges from $X = 0.00$ (pure nonionic surfactants) up to $X = 0.35$ (a proportion of 35 mol% of anionic SDS surfactants). The samples were prepared three days before each experiment to allow sufficient dissolution. Detailed information on the surfactant properties is listed in Table 5.4.

3.2 Methods

3.2.1 Atomic force microscopy (AFM)

Parts of this section are published in "Recent progress in measurements of oscillatory forces and liquid properties under confinement", Michael Ludwig and Regine von Klitzing, *Curr. Opin. Colloid Interface Sci.*, **2020**, 47, 137-152. [39] doi:10.1016/j.cocis.2020.02.002

Principle Atomic force microscopy (AFM) was originally invented for imaging the topographies of surfaces in 1986 [103]. In a typical AFM experiment, a sharp tip is located at the end of a micro-fabricated cantilever, which is then brought in contact with the sample surface and scanned over the surface by moving either the tip or the sample. All AFM experiments rely on monitoring the elastic deformation of the cantilever.

In the following years, AFM quickly developed as a technique for force spectroscopy. In the past 40 years, several other techniques for direct measurements of surface forces were developed, namely: the surface forces apparatus (SFA), optical tweezers and total internal reflection microscopy. Related to that, the disjoining pressure in films with fluid interfaces can be controlled by sucking the liquid out of the film (capillary cell) or by applying an outer pressure (porous plate technique or thin film pressure balance). Excellent reviews are given by Claesson *et al.* [104] and in the book of Butt and Kappl [12]. All of these techniques vary in contact geometry/area as well as in force resolution. They can be considered as complementary techniques rather than competitive ones. Among all direct force measuring techniques, AFM and SFA are the most commonly used instrument. The following will only focus on AFM, since all force measurements presented in this work were carried out using this technique.

Colloidal-probe atomic force microscopy (CP-AFM), introduced in the early 1990s [105–108], extends the concept of AFM towards more controlled force measurements. Figure 3.2 shows a schematic drawing of the CP-AFM setup, together with various possible measurement geometries. The curvature of the confining surface is exactly known using a colloial-probe, and thus, the measured force F can be normalised using the Derjaguin approximation (eqn. 2.13). This allows the results to be compared with the surface energy W. The colloidal-probe, most often a silica microsphere, is glued at the

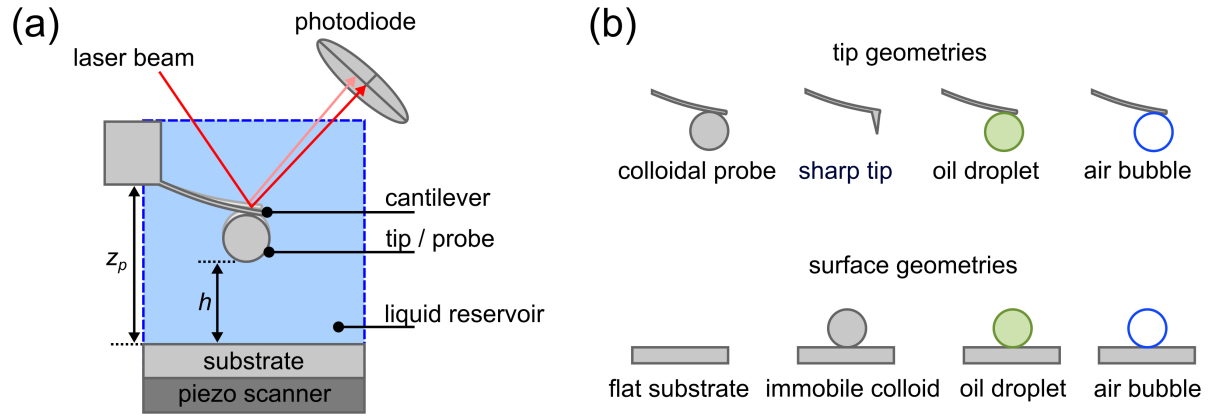

Figure 3.2: (a) Scheme of the instrumental setup in a CP-AFM measurement. (b) Overview of different tip and surface geometries used in force measurements.

end of a cantilever using a microtranslational stage or the AFM itself. It was shown that the stability of the glued particle can be increased by sintering the particle after glueing [109]. This processing is only applicable for cantilevers made of silicon or silicon nitride without any additional reflective coating due to the high temperatures needed for sintering (usually above 1100 °C). Although the reflected laser intensity of uncoated cantilevers is sufficient for most applications, this approach can limit the use of very soft and thin cantilevers, where the intensity of the reflected laser beam is very low.

Further geometries were established besides a spherical colloidal particle and a flat substrate. Sintering micronsized silica particles not only at the cantilever but also at a quartz glas disk allows AFM measurements between two (almost) identical particles [110, 111]. This is, with the exception of optical tweezers, the only method where symmetric, non-deformable confining surface, *i.e.* surfaces with the same geometry and surface potential, can be realised so far [112]. Bubbles generated at a solid substrate can also be used as an opposing surface. This allows the interaction of a solid and a deformable surface to be measured, *e.g.* between a silica surface and an air bubble [97, 113, 114]. Extending this principle, the interaction force between a pair of oil or gas bubbles can be directly measured using AFM [115, 116]. A hydrophobised cantilever is used to pick up one suitable bubble from the substrate. This "bubble-probe" is then aligned on top of another bubble in order to directly measure the interactions between the two bubbles. Once the substrate is changed from a flat surface, lateral adjustment

of the particles or droplets is required. This is typically done via optical microscopy which is integrated in an AFM setup.

Until recently, the size of colloidal probes was limited to $\gtrsim 1\,\mu m$ since it had to be visible in an optical microscope in order to be attached to the cantilever. Particles with a soft outer shell, like a polymer coating, could neither be used with this approach. These limitations were overcome using micro-fabricated cantilevers in the so-called "FluidFM-technology" [117, 118]. Instead of glueing the particles permanently to the cantilever, the particles can be sucked by a hollow microfabricated cantilever. Like this, the interaction force of particles with a diameter down to less than 500 nm as well as of polymer-coated particles could be measured.

Data processing In general, the raw data in an AFM force measurement consists of two parts measured simultaneously: (i) the deflection of a cantilever which is typically detected by the reflection of a laser beam from the top of the cantilever onto a photodiode (detector signal S), (ii) the displacement of the piezoelectric scanner (z piezo position z_p). To convert the raw data into force F versus separation h curves (in the following described as force profiles), a well known algorithm was developed [105, 108, 119] (Fig. 3.3). It has to be noted, that the distance between tip and substrate is not measured directly which can be problematic using soft cantilevers and/or when matter strongly adsorbs onto the surface.

The construction of force versus separation profiles involves several steps:

1. For large separations, the cantilever does not interact with the surface (region 1 in Fig. 3.3). In this region, the cantilever does not bend upon approaching the surface and a constant detector signal S_0 is obtained.

2. Next, region 4 of Fig. 3.3 is considered. There, the colloidal probe is considered to be in contact with the substrate and every movement of the z piezo z_p is directly transferred into bending of the cantilever z_c. This is called "constant compliance region". Defining this region is crucial for successful force measurements.

$$z_p = z_c \quad \text{(constant compliance region).} \tag{3.1}$$

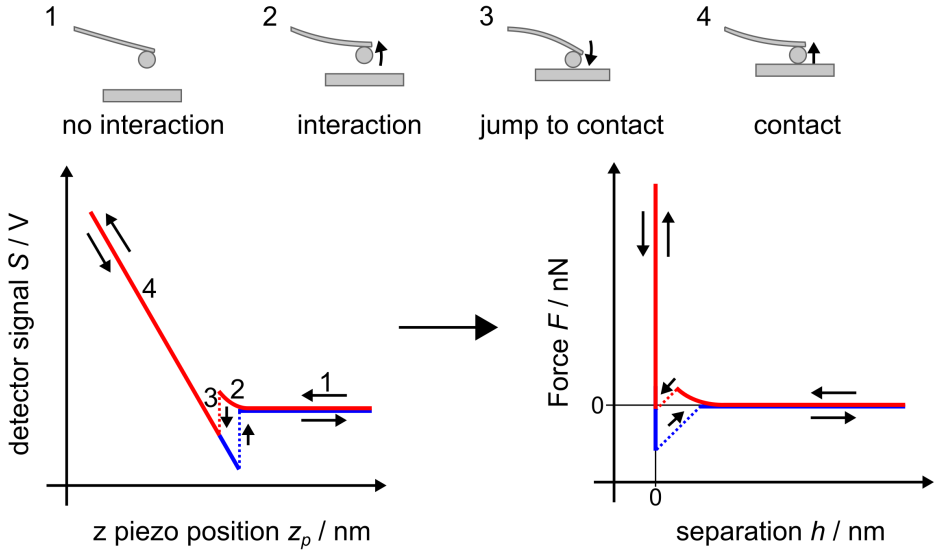

Figure 3.3: Schematic of an AFM force measurement. The left graph shows the measured raw data: detector signal S versus z-piezo position z_p. The force F versus separation h profile (right graph) is derived from the raw data. Cantilever and surface motion is schematically shown on top.

$$S = \mathrm{OLS}\, z_c, \text{ with } \mathrm{OLS} = \frac{\Delta S}{\Delta z_c} \tag{3.2}$$

The optical lever sensitivity (OLS) is the slope of the curve in region 4 and acts as conversion factor between the detector signal S (in V) and the cantilever deflection z_c (in nm).

3. The position of the z piezo where both surfaces start to touch is denoted as $z_{p,0}$. It is calculated from the intersection of the fitted constant compliance region and the detector signal without bending of the cantilever S_0.

$$z_{p,0} = \mathrm{OLS}^{-1}\, S_0 \tag{3.3}$$

In the following, the surface separation h can be calculated from the combined movement of the substrate z_p and the bending of the cantilever z_c.

$$h = z_p + z_c - z_{p_0} \tag{3.4}$$

4. Finally, the cantilever deflection z_c is converted into force F from the cantilevers spring constant k_c, using Hook's law:

$$F = k_c \, z_c. \tag{3.5}$$

Substrates and Colloidal Probes All force measurements were carried out between a spherical colloidal probe and a flat substrate, *i.e.* in sphere-plate geometry. Silicon wafers (Soitec, France) were used as substrates. Prior to the experiments, the wafers were cleaned by the Piranha method, using a 1:1 (vol:vol) mixture of hydrogen peroxide (30 %, Th. Geyer, Germany) and sulphuric acid (96 %, Carl Roth, Germany). With this method, a very smooth native silica layer is formed on the silicon surface. Afterwards, the wafers were rinsed with large amounts of water and dried in a nitrogen stream. Non-porous, spherical silica particles (Bangs Laboratories, USA) with a diameter of 5 µm were used as colloidal probes. One particle was glued (UHU Endfest Plus 300, UHU, Germany) to the end of a tipless rectangular cantilever (SD-qp-SCONT-TL, Nanosensors, Switzerland) using a three-dimensional microtranslation stage (MP-225, Sutter Instrument, USA). Immediately before the experiment, both, cantilever and substrate, were cleaned by exposure to oxygen plasma (Diener Femto, Germany) to remove all organic impurities.

Determination of the cantilever spring constant Various methods for the determination of the spring constant have been reported [120–122]. In this thesis, the method by Sader *et al.* [123] was used which is nowadays incorporated in different AFM softwares. It determines the cantilevers spring constant k_c from the resonance frequency ν_0 and the quality factor Q of the cantilevers first resonance peak, which is excited from thermal noise as:

$$k_c = 0.1906 \rho w^2 L Q \Gamma_i(Re) (2\pi\nu_0)^2. \tag{3.6}$$

To be able to apply this method, both the width w and the length L of a rectangular cantilever have to be known. ρ is the density of the surrounding medium and $\Gamma_i(Re)$ is the

imaginary part of the hydrodynamic function that depends on the Reynolds number Re. Furthermore, the viscosity η of the surrounding medium has to be known.

$$Re = \frac{\rho w^2 2\pi\nu_0}{4\eta} \tag{3.7}$$

In principal, this method can be applied to various fluids, yet uncertainties increase for stronger hydrodynamic interaction. As a result, this method should preferentially be applied in air.

Experiments Force measurements were carried out using a Cypher ES atomic force microscope (Asylum Research, USA). Before each experiment, the spring constants of the cantilevers were determined as $0.012 - 0.026\,\mathrm{N\,m^{-1}}$. After calibration, cantilever and substrate were completely immersed within the various dispersions. The temperature was set to $20.0\,^\circ\mathrm{C}$ via a cooler-heater sample stage and left to equilibrate for at least 30 minutes. Force profiles were generated as described above. The Derjaguin approximation was used to normalise the measured force F against the effective radius R_{eff}. For a sphere-plate geometry, R_{eff} is simply the colloidal probe radius R. The resulting force is, therefore, in the following described as $\frac{F}{R}$.

The starting point of each measurement in silica nanoparticle suspensions was set to 1000 nm with an approach-retraction velocity of $100\,\mathrm{nm\,s^{-1}}$. The starting point in micellar dispersions was set to 500 nm with an approach-retraction velocity of $50\,\mathrm{nm\,s^{-1}}$. In very viscous micellar dispersion the velocity was reduced to $10\,\mathrm{nm\,s^{-1}}$. At these velocities, the hydrodynamic force on the cantilever is negligibly small. The surfaces were assumed to be in contact (*i.e.* constant compliance region) once the normalised force $\frac{F}{R}$ exceeds $0.4\,\mathrm{mN\,m^{-1}}$ in chapters 4 and 5. In chapter 6, the onset of the constant compliance region was increased to $2.5\,\mathrm{mN\,m^{-1}}$ to overcome double layer repulsions. For each system, at least 30 individual force profile were averaged to ensure reproducibility and to substantially increase the force resolution to less than $0.002\,\mathrm{mN\,m^{-1}}$. The data shown are the results of averaging the stacked experimental curves (binomial smooth, 10^3 points) unless stated otherwise.

Fitting of interaction forces Processing and fitting of experimental data was done using the Igor Pro software (Wavemetrics, USA). In chapters 4 and 5, the normalised

interaction forces $\frac{F}{R}$ between two surfaces at separations h are fitted to the oscillatory structural force F_{osc} (similar to eqn. 2.41).

$$\frac{F}{R}(h) = \frac{F_{\text{osc}}}{R}(h) = -A \cdot \exp\left(-\frac{h}{\xi}\right) \cdot \cos\left(\frac{2\pi}{\lambda}(h - h')\right) \tag{3.8}$$

The force profile is described by the amplitude A, the decay length ξ, and the wavelength λ. The parameter h' corrects for the offset of the structural force. The fit parameters of the oscillatory structural force may vary so that the fit parameters are not independent of the fit region [88]. To account for this, the starting point of the fit is varied. Error bars refer to the standard deviations of all individual fits with different starting points in the force profile. This fitting procedure resolves the force profile for surface separations above the first maximum of the oscillatory structural force.

Typically, van der Waals forces are taken into account for the description of interaction forces. The Hamacker constant of the type of silica colloidal probe used was previously determined as $A_H = 0.07 \times 10^{-21}$ J [110]. Van der Waals forces are, therefore, neglected in the following analysis, since they are small and short ranged under the studied conditions. We also neglect double layer forces between the confining surfaces in chapters 4 and 5, assuming that they do not influence the force profile at surface separations above the first maximum of the oscillatory structural force.

The influence of the double layer force is investigated in chapter 6. By increasing the onset of the constant compliance region to 2.5 mN m^{-1}, the double layer repulsion can be overcome. This enables the complete interaction force profiles, *i.e.* also at surface separations below the first maximum of the oscillatory structural force to be described. Therefore, the normalised interaction forces $\frac{F}{R}$ between two charged surfaces at separations h were fitted using a superposition of double layer F_{dl} and structural forces F_{str}.

$$\frac{F}{R}(h) \;=\; \frac{F_{\text{dl}}}{R}(h) + \frac{F_{\text{str}}}{R}(h)\,. \tag{3.9}$$

To properly describe both force contributions, assumptions were made. Detailed explanation continues in chapter 6.

3.2.2 Small-angle neutron scattering (SANS)

Principle Self-assembled structures in aqueous solution, *e.g.* surfactant micelles, have low contrast for imaging techniques, such as electron microscopy. Imaging with real space techniques requires a lot of effort in sample preparation and is often invasive to the fragile structures. Small-angle neutron scattering (SANS) provides an elegant way to *in situ* and non-invasively probe the structure of such complex fluids. Concentrated colloidal dispersions have now been studied via this method since over 50 years.

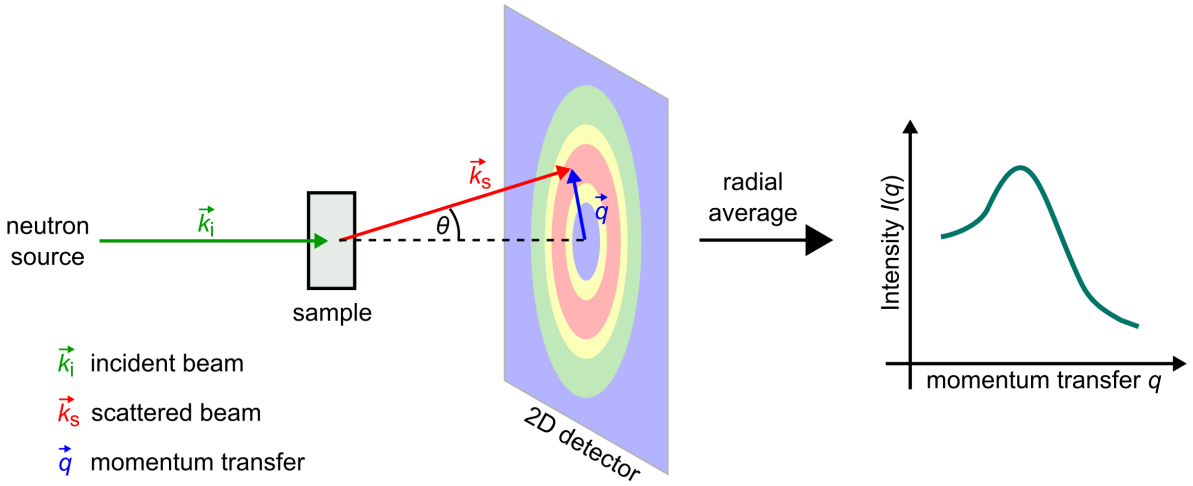

Figure 3.4: Sketch of a small-angle neutron scattering (SANS) setup. (adapted from [124–126])

Figure 3.4 shows the typical setup of an SANS experiment. The incoming beam of monochromatic, highly collimated neutrons is interacting with the sample and gets scattered under a specific scattering angle θ. The scattered beam intensity is then detected as a function of the scattering angle θ. In practice, a scattering vector $\vec{q}$ is defined instead of using the scattering angle θ.

$$\vec{q} = \vec{k}_s - \vec{k}_i \tag{3.10}$$

$\vec{k}_s$ and $\vec{k}_i$ are the propagation vectors of the scattered beam and the incident beam, respectively. In elastic scattering, the only type of scattering used in throughout this work, the magnitudes of $\vec{k}_s$ and $\vec{k}_i$ are identical. The neutron beam only changes its direction but not its energy. The magnitude of the scattering vector q corresponds to

the length of $\vec{q}$ as illustrated in Figure 3.4 and can be written as a function of scattering angle θ and the neutron wavelength λ.

$$q = |\vec{q}| = \frac{4\pi}{\lambda} \sin\left(\frac{\theta}{2}\right) \tag{3.11}$$

The scattered intensity I is a quantitative description of the interaction of the radiation with the sample. It only depends on the structure of the sample and the type of radiation used. For isotropic scatterers, the 2D signal at the detector can be radially averaged. The resulting coherent scattering intensity $I(q)$ is a function of the scattering vector q. It is given by:

$$I(q) = n_p \, P(q) \, S(q) \; + \; B. \tag{3.12}$$

with n_p being the number density of colloidal particles. $P(q)$ is the form factor of a single particle which is characteristic for the particle size and shape. $P(q)$ includes information on the particle volume V_p and the contrast factor $\Delta\rho$. The structure factor $S(q)$ describes the interparticle interactions and structure. A constant background B accounts for incoherent scattering.

The contrast factor $\Delta\rho$ is defined by the difference in scattering length density (SLD) between two phases. The scattering length for neutrons depends considerably on the isotope, especially for hydrogen and deuterium. It is, therefore, common in SANS experiments to use deuterated samples and/or solvent to increase contrast [127, 128].

The experimentally measured intensity $I(q)$ cannot be fitted directly and models for $P(q)$ and $S(q)$ have to be chosen in order to reconstruct the scattering profile. Combining externally obtained information helps to choose an appropriate expression for $P(q)$ and $S(q)$. Form factors for a wide variety of structures were derived and were summarised by Pedersen *et al.* [129].

Experiments Small-angle neutron scattering experiments were carried out on the D11 beamline at the Institut Laue-Langevin (ILL, Grenoble, France) [130]. A neutron wavelength of $\lambda = 5.5\,\text{nm}$ with $\Delta\lambda/\lambda = 0.1$ and sample-detector distances of 1.8 and 8 m were used to cover a q-range of 0.006 - 0.395 Å^{-1}. Samples were measured in Hellma quartz cells with a path-length of 2 mm. The temperature was adjusted to 20.0 °C.

The sample scattering was normalised with respect to incident intensity, transmission, sample thickness, acquisition time and background. The data were brought to absolute scale using ultrapure water as secondary standard. Data reduction was done using the Lamp software on site of the ILL.

The Institut Laue-Langevin is acknowledged for the provision of beam time. Data is available from doi:10.5291/ILL-DATA.EASY-440 and doi:10.5291/ILL-DATA.EASY-646.

Theoretical modelling In chapter 5, SANS is used to investigate the bulk structure of surfactant micelles. The scattering intensity $I(q)$ is a function of the scattering vector magnitude q in micellar dispersions and is modelled as:

$$I(q) = n_p \, P(q) \, S'(q) \, + \, B. \tag{3.13}$$

Its intensity and shape depends on the number density of micelles n_p. B is a constant background that takes incoherent scattering, mostly from hydrogen, into account. Analysis of the reduced SANS data was done with build-in functions in the SASView 5.0.3 software (www.sasview.org).

A monodisperse core-shell ellipsoid model is used to describe the form factors $P(q)$ of single micelles [131, 132] (Fig. 3.5, see SASView 5.0.3 documentation for details). The main parameters in this model are: the equatorial radius of the core (r_c), the axial ratio between the polar and the equatorial radius of the core (x_c), and the thickness of the shell (t_s), which is assumed constant throughout the whole area. The scattering length density of the core (ρ_c), the shell (ρ_s), and the solvent (ρ_{D_2O}) represents the contrast of the micelles.

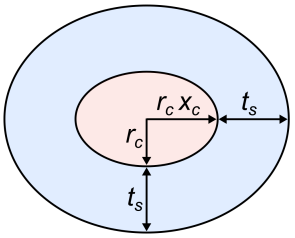

Figure 3.5: Schematic drawing of the core-shell ellipsoid model used for the calculation of the single particle form factor $P(q)$.

In order to reduce the number of fit paramters, following assumptions are made: the core consists of hydrophobic hydrocharbon chains; the shell contains the surfactant polar headgroups hydrated by water molecules that can penetrate the shell but not the core. The equatorial radius of the micelle core r_c is fixed to 1.67 nm, being the length of a fully extended dodecyl hydrocarbon chain [133]. The core extends in the direction of the polar radius and is fitted by the axial ratio of the core x_c. The core is assumed to only contain hydrocarbon chains, so that the scattering length density (SLD) of the core is $\rho_c = -0.39 \times 10^{-6}\,\text{Å}^{-2}$. The solvent SLD is $\rho_{D_2O} = 6.34 \times 10^{-6}\,\text{Å}^{-2}$. The fitted shell thickness t_s is equal throughout a single micelle. The strong hydration of the surfactant polar groups was taken into account by fitting the SLD of the shell ρ_s. Self-consistent fitting was checked using material balance equations from known molecular volumes and SLDs (details in Table 5.5).

A structure factor $S(q)$ generally accounts for interparticle interactions and structure. In systems containing disordered ellipsoidal scatterers, an apparent, orientationally-averaged interparticle structure factor $S'(q)$ is approximated from the structure factor of isotropic scatterers, using the decoupling approximation. It assumes that the interactions between the particles are independent from particle size and orientation and is, therefore, only valid for small polydispersities and small anisotropies [131].

$$S'(q) = 1 + \frac{P(q)^2}{\langle |P(q)|^2 \rangle}(S(q) - 1) \tag{3.14}$$

We use two different interaction potentials to fit the intermicelle structure factor $S(q)$. For micelles with a charged surface (*i.e.* pure anionic and mixed nonionic-anionic micelles), the RMSA (rescaled mean spherical approximation) [134] based on the mean spherical approximation (MSA) from Hayter and Penfold [18] is used. It describes the intermicellar interaction as a hard-sphere with screened Coulombic potential. For uncharged particles (*i.e.* pure nonionic micelles), a hard-sphere interaction potential with the PY (Percus-Yevick) closure relationship is used [17]. The MSA and PY closure relationship provide analytical solutions to the Ornstein-Zernike integral equations [15, 16]. Both yield identical results in the case of hard-sphere fluids and can, therefore, be used for the transition of uncharged and charged micelles.

In this analysis, the volume fraction of micelles ϕ results from fitting the structure factor $S(q)$, assuming the ellipsoids to occupy its equivalent volume of a sphere. The surface charge z per micelles is also fitted to $S(q)$. No surface charge is extracted for

pure nonionic micelles, since its structure factor was modelled using the hard-sphere interaction of uncharged particles. A recent study shows that hard-sphere interactions are sufficient to describe the interactions between Tween20 micelles [135]. At higher degrees of ethoxylation (>20), partial charges on the ether oxygen in the EO groups enhance the intermicellar interactions. By defining the ellipsoidal micelle to occupy its equivalent volume of a sphere, an effective micellar radius r_{eff} can be calculated:

$$r_{\text{eff}} = [(r_c + t_s)^2 (r_c x_c + t_s)]^{1/3}. \tag{3.15}$$

The aggregation number N_{agg} is calculated from the volume fraction of micelles ϕ, the effective radius r_{eff}, the total surfactant concentration c, and Avogadros number N_A:

$$N_{\text{agg}} = \frac{4}{3}\pi r_{\text{eff}}^3 \frac{cN_{\text{A}}}{\phi}. \tag{3.16}$$

Nonionic surfactants feature low critical micelle concentrations ($cmc = 0.049$ mM for Tween20 [136]; 0.09 mM for BrijL23 [137]). Here, the lowest concentration of nonionic surfactant is 82 mM allowing the *cmc* to be neglected in the calculations. Finally, the micelles fractional charge β is defined for charged micelles.

$$\beta = \frac{z}{N_{\text{agg}}} \tag{3.17}$$

The extracted structure factor $S(q)$ of micelles with a near range ordering shows a pronounced first-order peak, that can be fitted to a Lorentzian profile:

$$S(q) = \frac{S_{\text{max}} \left(\frac{\Delta q}{2}\right)^2}{(q - q_{\text{max}})^2 + \left(\frac{\Delta q}{2}\right)^2} + S_0, \tag{3.18}$$

where S_{max} denotes the intensity of the peak, Δq is the full width at half maximum (FWHM), q_{max} the position and S_0 the baseline of the peak. The Lorentzian peak profile is the Fourier transformation of the radial distribution function $g(r)$ of the micelles (eqn. 2.9). Because of this, the Lorentzian lineshape of $S(q)$ can be used for description the of micellar bulk structuring [79, 87, 138]. The same approach is applied in chapter 5.

This work benefited from the use of the SasView 5.0.3 application, originally developed under NSF award DMR-0520547. SasView contains code developed with funding from the European Union's Horizon 2020 research and innovation programme under the SINE2020 project, grant agreement No 654000.

3.2.3 Additional methods

Mass spectrometry of nonionic surfactants Experiments were carried out by the mass spectrometry core facility team of the Chemistry Department (TU Darmstadt). MALDI-TOF experiments were carried out using an Autoflex speed TOF/TOF (Bruker Daltonik) mass spectrometer. A saturated solution of alpha-cyano-4-hydroxycinnamic acid (HCCA) in acetonitril / 0.1 % aqueous TFA (30:70, v:v) was used as matrix. Possible added salt solutions were 0.1 mol L^{-1} aqueous KTFA or NaTFA solutions. Aqueous solution of Tween20 and BrijL23 with a concentration of $c = 100$ µg mL^{-1} were prepared. 20 µL of the aqueous surfactant solution was mixed with 20 µL matrix solution and 1 µL salt solution. 1 µL of the resulting mixture was then deposited on the sample target and dried. Measurements were performed operating in the positive-ion reflector mode. Spectra in the m/z range of 500 to 2500 were obtained by accumulating data from 4500 laser shots. The mass spectra were evaluated using the mMass software (Version 5.5.0). The instrument was provided by the German Research Foundation (DFG) through grant no INST 163/445-1 FUGG (MALDI MS).

Density measurements The densities of silica NP suspensions were determined by weighing suspensions with known concentrations using a high precision volumetric flask. Setting the density of water to 0.998 g cm^{-1} (20 °C) the density for silica was determined as 1.97 ± 0.07 g cm^{-1}. The determination was not carried out using a density meter in order to avoid adsorption of silica NPs onto the mechanics of the instrument.

Densities of nonionic surfactants (Tween20 and BrijL23) were determined by density measurements of aqueous surfactant solutions with known mass fractions. Measurement were carried out using a density meter (DM40, Mettler Toledo, Germany).

Transmission electron microscopy (TEM) Transmission electron microscopy measurements were carried out by my colleague Marcus U. Witt. Single silica NPs were imaged using transmission electron microscopy (TEM) (FEI CM20 microscope, The Netherlands). The TEM was equipped with a LaB_6 cathode (acceleration voltage of 200 kV) and a Gatan double tilt holder. The samples were prepared by drying a drop of a 0.02 wt% suspension of silica NPs on a copper grid covered with a carbon film (300mesh, Science Service, Germany). The analysed images obtain a resolution of up to 0.83 nm per pixel. Images were evaluated using the ImageJ software (imagej.nih.gov).

Zeta-Potential measurements The electrophoretic mobilities μ_e of silica NPs were measured by electrophoretic light-scattering, using a Nano Zetasizer (Malvern Instruments, UK). The electrophoretic mobility is defined as the velocity $\vec{v}$ of the particles in response to an electric field $\vec{E}$.

$$\vec{v} = \vec{E}\mu_e \tag{3.19}$$

Before each measurement, the measuring cell was rinsed thoroughly with water and absolute ethanol and dried in a nitrogen stream. The samples were equilibrated for 2 min at 25 °C. Three measurements, each consisting of at least ten runs were performed for each sample. The particles' zeta-potential ζ was then calculated from the electrophoretic mobility μ_e using Henry's equation:

$$\mu_e = \frac{2\epsilon_0\epsilon\zeta}{3\eta} f(\kappa R). \tag{3.20}$$

Here, ϵ_0 is the dielectric permittivity of vacuum, ϵ is the dielectric constant of the liquid, and η the dynamic viscosity of the liquid. $f(\kappa R)$ is known as the Henry function, a correction function that relates the particle radius R to the thickness to the diffuse layer around the particle. The Henry function was calculated for all measured NP suspensions separately using a build-in function in the Zetasizer software. Due to the low ionic strength of the silica NP suspensions, the correction function becomes small ($\kappa R \ll 1$) and the Henry function $f(\kappa R)$ is in all cases close to 1, which is known as the Hückel approximation [139, 140].

Conductivity measurements The conductivities of suspensions containing silica NPs and monovalent salt were measured using a Nano Zetasizer (Malvern Instruments, UK). The sample and cell preparation is the same as for zeta-potential measurements. Typically, the conductivity was measured with the same run as the zeta-potential. One data point is averaged by at least five measurements to ensure reproducibility.

Potentiometric Titration Potentiometric titration of silica NP suspensions (initial volume = 10 mL) were carried out at three different volume concentrations of NPs upon addition of hydrochloric acid solution (HCl, Titrisol, Merck, Germany). The pH was measured using a pH-electrode (inoLab pH 720, VWR, Germany).

4 Limit of the inverse cubic root scaling law

Similar content is published in "Bridging the gap between two different scaling laws for structuring of liquids under geometrical confinement" Michael Ludwig, Marcus U. Witt, and Regine von Klitzing, *Adv. Colloid Interface Sci.*, **2019**, 269, 270-276. [141] doi: 10.1016/j.cis.2019.04.012

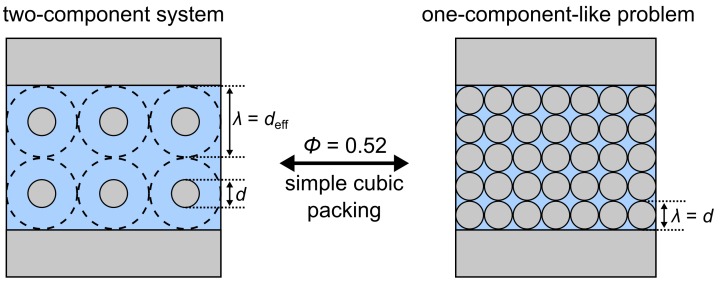

Abstract

Oscillatory forces are a phenomena obtained when confining liquids of one-component (*e.g.* for organic solvents) and two-components (colloidal dispersions), alike. In this chapter, an attempt is made to bridge the gap between both systems by defining the limit of the scaling law for two-component systems. Colloidal-probe atomic force microscopy (CP-AFM) is used to measure oscillatory structural forces acting on surfaces across suspensions containing silica nanoparticles of three different sizes. The oscillation wavelength λ in the measured force profiles is larger than the actual particle diameter and depends on the particles volume fraction ϕ, following the inverse cubic root scaling law: $\lambda \propto \phi^{-1/3}$. It is shown that the particle diameter can be determined by

a gedankenexperiment extrapolating the fitted wavelength from the oscillatory structural force measurements to a particle volume fraction of $\phi = 0.52$ - the packing factor for simple cubic packing. This extrapolation can be interpreted as the transition from a two-component system towards a one-component-like problem. In this case, particles are assumed to be in contact and the wavelength is equal to the particle diameter as in one-component systems. The determined diameters of the different silica nanoparticles agree well with independent measurements using transmission electron microscopy (TEM), validating the used approach.

4.1 Introduction

So far, research typically focussed on the prediction of the oscillatory structural force by investigating the properties of colloidal dispersions, such as the particles size and shape and interparticle interactions. This chapter, can be considered as the inverse problem. How can particle properties be determined from measurements of the oscillatory structural force?

In chapter 2, two different systems inducing oscillatory forces were defined: For one-component systems, the information is typically straight forward. There, the wavelength λ in the force profile is equal to the predominant structure d perpendicular to the confining surfaces ($\lambda = d$), such as *e.g.* the diameter of solvent molecules or a domain size in liquid crystals. When two-component systems, *i.e* colloidal dispersion, contain spherical, charged particles, the wavelength λ of the oscillatory structural force depends on the particles volume fraction ϕ as $\lambda \propto \phi^{-1/3}$.

So far, one- and two-component systems were discussed separately. Here, an attempt is made to bridge the gap between these two cases by determining the limit of the inverse cubic root scaling law for two-component systems. This limitation can be used to extract particle properties. In this specific case, the diameter of silica nanoparticles is determined by measurements of oscillatory structural forces across aqueous suspensions of the respective nanoparticles.

4.2 Results

4.2.1 Particle characterisation using electron microscopy

Transmission electron microscopy (TEM) is used as an independent method to determine the diameters of the silica nanoparticles (NPs). The spatial resolution obtained from electron microscopy is sufficient to distinguish between single particles and to obtain a good analysis of the solid NPs. Fig. 4.1 shows representative micrographs and the estimated size distributions for the three different types of NPs used. Size distributions are calculated using 166 Ludox SM, 1049 Ludox HS and 1289 Ludox TM particles. The mean particle diameters are determined as 10.3 ± 2.0 nm, 15.8 ± 2.9 nm, and 26.1 ± 4.0 nm, respectively.

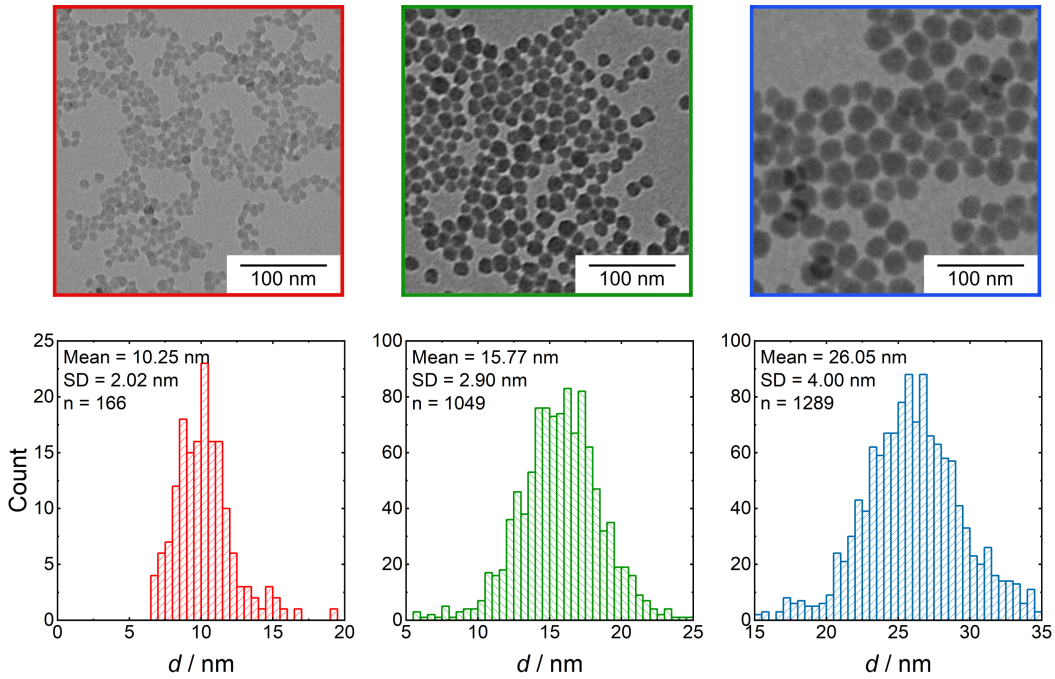

Figure 4.1: Top: Representative TEM micrographs of Ludox SM (red, left), Ludox HS (green, middle) and Ludox TM (blue, right) silica NPs;
Bottom: Size distribution of Ludox SM (red, left), Ludox HS (green, middle) and Ludox TM (blue, right) particles. The mean value, standard deviation and amount of analysed particles is added for each type of NPs.

The zeta-potentials ζ of the NPs are determined as -83.6 ± 3.2 mV, -77.7 ± 4.0 mV,

and $-69.6 \pm 2.2\,\mathrm{mV}$ for Ludox SM, Ludox HS and Ludox TM, respectively. The zeta-potentials ζ do not change within the used particle concentrations.

4.2.2 Oscillatory structural forces across nanoparticle suspensions

Interaction forces between macroscopic surfaces across silica NP suspensions were measured at various volume fractions ϕ of NPs (Fig. 4.2). All force profiles show characteristic oscillatory structural forces due to the structuring of the NP suspension between the confining surfaces. In general, more oscillations are observed at higher particle concentrations. At the highest particle concentrations, oscillatory structural forces could be detected up to a surface separation of over 200 nm. The wavelength λ of the oscillations decreases with increasing particle concentration, reflecting a decrease in distance between the layers of particles. If the gradient in the force profile exceeds the cantilevers spring constant, the full force curve cannot be resolved and a "jump" to the next stable branch occurs. Here, this phenomena is observed for Ludox HS suspensions at higher concentrations and for all Ludox SM suspensions.

The normalised interaction forces $\frac{F}{R}$ between two surfaces at separations h are fitted to the oscillatory structural force F_{osc} as described in chapter 3.

$$\frac{F}{R}(h) = \frac{F_{\mathrm{osc}}}{R}(h) = -A \cdot \exp\left(-\frac{h}{\xi}\right) \cdot \cos\left(\frac{2\pi}{\lambda}(h - h')\right) \tag{4.1}$$

Summary of all fit parameters can be found in Table 4.2, Appendix. The following section focusses on the information extracted from the wavelength λ.

It is noted, that in the original publication [141], an extended fitting procedure has been applied. The detailed fitting procedure was previously developed in this research group by Sebastian Schön [88]. There, an additional exponential decay, with two additional parameters B and ξ_2 improves the fit at small surface separations h. Furthermore, it shows, that fit parameters are more stable with respect to the area of the fit. The extended fitting procedure is deliberately left out in this chapter since it is not necessary for a sufficient description of the wavelength λ. The need of an extended fitting procedure is discussed in chapter 6.

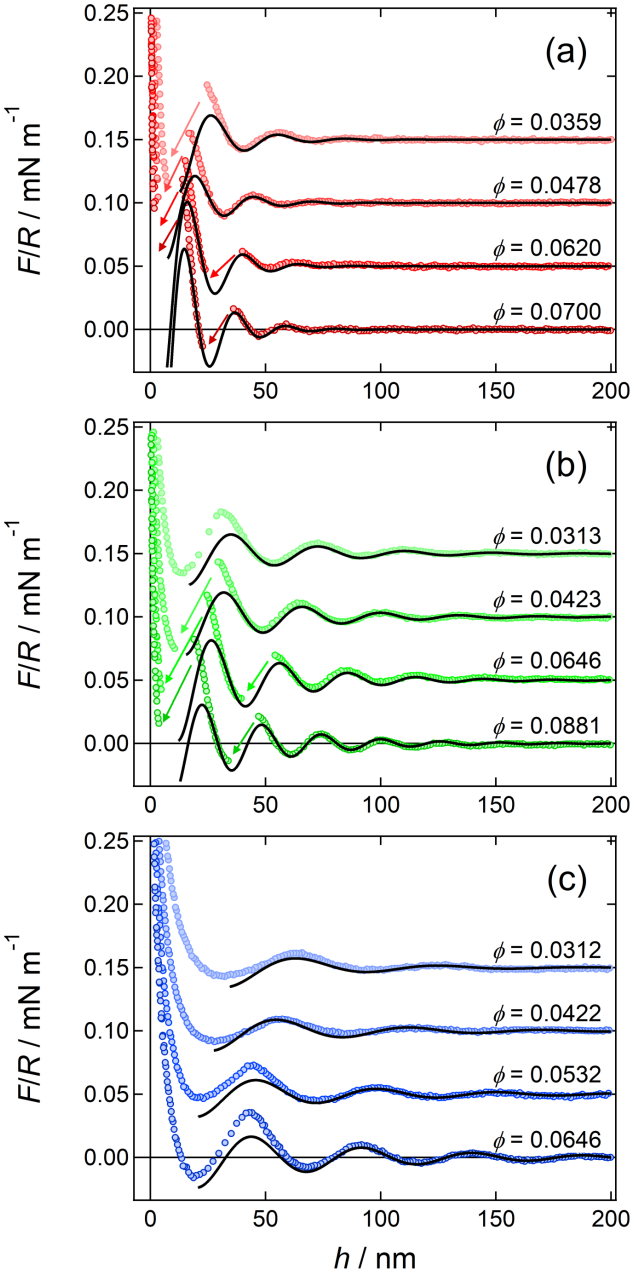

Figure 4.2: Interaction force profiles across different silica NP suspensions at various volume fractions ϕ of NPs. (a) Ludox SM, (b) Ludox HS, and (c) Ludox TM. The curves are vertically shifted for clarity. Arrows indicate "jumps" of the cantilever. Data are fitted to eqn. 4.1 (black, solid line).

4.2.3 Nanoparticle diameters extracted from force measurements

Fig. 4.3 shows the fitted wavelength λ as a function of particle volume fraction ϕ for all measured NP suspensions. The coloured dotted lines describe the well-known inverse cubic root scaling law for charged particles: $\lambda \propto \phi^{-\frac{1}{3}}$.

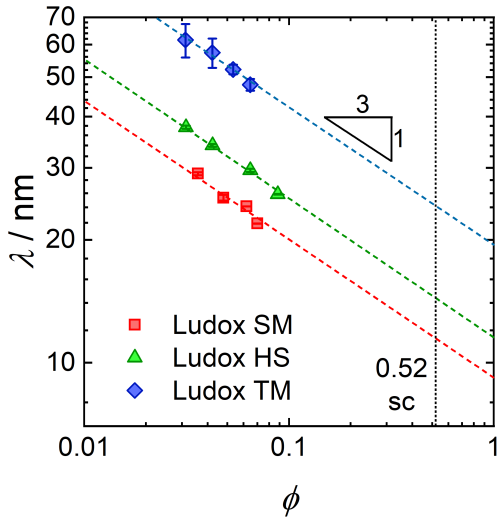

Figure 4.3: The fitted wavelength λ in dependence of the NPs' volume fraction ϕ for different Ludox suspensions. The coloured dotted lines act as a guide for the eye to emphasise the $\lambda \propto \phi^{-\frac{1}{3}}$ scaling. The vertical dotted line shows the volume fraction of $\phi = 0.52$ for a simple cubic (sc) packing.

Concentrating a suspensions volume fraction ϕ to a value of $\phi = 0.52$ - the packing factor of simple cubic packing - would mean that the dispersed NPs are in contact already in bulk suspension. In this case, the wavelength λ extracted from oscillatory structural force measurements should equal the particle diameter d, achieving a transition from a dispersed two-component systems towards a one-component-like problem. Experimental measurements are, however, limited to NPs' volume fractions of $\phi \lesssim 0.10$ due to increasing viscosities with increasing particle concentrations. Nevertheless, one can extrapolate the fitted wavelengths λ at a known solid volume concentration ϕ, to the solid volume concentration of $\phi = 0.52$, using the inverse cubic root scaling law. This is schematically shown in Fig. 4.3 as the intersections of dotted lines. Thus, the diameter d of silica NPs in suspensions can be determined by oscillatory structural force measurements via eqn. 4.2. Resulting values for the diameters d can be found in Ta-

ble 4.1.

$$\log d = -\frac{1}{3} \cdot \log 0.52 + \left(\log \lambda + \frac{1}{3} \log \phi \right) \tag{4.2}$$

Linear fitting of the experimental values for the wavelength λ against particle concentration ϕ has been performed. The slope α reflects the exponent of the scaling law as $\lambda \propto \phi^{\alpha}$. The slope of the linear fits for Ludox HS and Ludox TM particles agree well with the inverse cubic root law, with a value of $\alpha = -0.33$. The slope obtained for Ludox SM particles, however, is less clear pronounced.

Table 4.1 summarises the determined particle properties of silica NPs. Particle diameters d from the experimental wavelengths λ of CP-AFM experiments are compared to the mean particle diameter d as obtained from TEM measurements. For all three types of NPs, the independently obtained values from both methods are in good agreement with each other.

	d / nm (TEM)	d / nm (AFM)	ζ / mV	α
Ludox SM	10.3 ± 2.0	11.6 ± 0.3	-83.6 $\pm$ 3.2	-0.39 $\pm$ 0.06
Ludox HS	15.8 ± 2.9	14.6 ± 0.2	-77.7 $\pm$ 4.0	-0.36 $\pm$ 0.02
Ludox TM	26.1 ± 4.0	24.3 ± 0.4	-69.6 $\pm$ 2.2	-0.35 $\pm$ 0.04

Table 4.1: The determined properties of silica NPs: the particle diameter d from TEM and as calculated from the experimental wavelength λ from AFM experiments independently, the particles zeta-potential ζ, and the fitted exponent in the structural force scaling law of $\lambda \propto \phi^{\alpha}$

4.3 Discussion

4.3.1 Effective particle diameters in two-component systems

In two-component systems, the wavelength λ is considerably larger than the particle diameter d. For a better description of this phenomena, an effective particle diameter d_{eff} has to be introduced. First explanations described the effective particle diameter

d_{eff} in dispersion as the particle diameter + its counterion atmosphere, using the Debye screening length κ^{-1} with $d_{\text{eff}} = d + 2\kappa^{-1}$ [64]. This picture was proven to be insufficient in later publications [142, 143].

In dispersions with low ionic strength, the Debye length κ^{-1} is usually relatively large and the electrostatic interactions U_{el} long-ranged. Instead of describing the effective diamter d_{eff} with the Debye screening length κ^{-1} it can rather be determined by simple packing arguments. Due to the restricted space - the volume of the liquid - the repelling particles are holding itself in a preferred structuring. The particle accommodates its effective diameter d_{eff} to the available space in the dispersion, which is determined by the particle number density n_p, as proposed by Zeng *et al.* [87] and Danov *et al.* [142]. Different approaches have then been made to calculate an interparticle interaction U_{el} in charged disperison at low ionic strength [142, 144]. In these cases, a preferred structuring of the particles is obtained once the interparticle interaction U_{el} exceeds a certain threshold. An analytical approximation sets this threshold to $U_{el} = 2.8\,kT$ [144].

A previous study reports on small-angle scattering on silica NP suspensions in bulk and its combination with force measurements from CP-AFM demonstrating that the wavelength λ from force measurements equals the position of the suspensions structure factor $S(q)$ in bulk [87]. This is a direct proof, that the distance between NPs is almost equal in bulk and under confinement. Moreover, the average distance of the NPs in bulk dominates the distance between the NPs under confinement. The confining surfaces force the NPs into layering which can be detected by force measurements. Measurements of oscillatory structural forces in two-component systems, therefore, show bulk liquid properties, since the effective diameter d_{eff} is directly measured. This means that the measured wavelength λ is approximately the average distance between the particles in bulk solution D^*. In summary, following dependencies are observed:

$$d_{\text{eff}} = D^* = \lambda \approx (n_p)^{-\frac{1}{3}} = 1.612(0.5\,d)\phi^{-\frac{1}{3}}. \tag{4.3}$$

These dependencies seem fundamental since they are very robust against *e.g.* the salt concentration in dispersion [63] and surface properties, such as roughness and elasticity [96, 97]. With increasing salt concentration, the oscillatory structural forces in the experiment vanish as soon as the interparticle interaction U_{el} decreases and at a point that interparticle structuring cannot be sustained. Simultaneously, no change in the wavelength λ is obtained.

4.3.2 Limit of the inverse cubic root scaling law

So far, the one- and two-component-systems were discussed separately. In order to bridge the gap between the two systems, a limit of the inverse cubic root scaling law is proposed and discussed. An extrapolation to a particle volume concentration in which the effective diameter reduces to the real particle diameter is necessary. Fig. 4.4 visualises this gedankenexperiment. Due to the increased particle number density n_p the effective diameter is shrinking. The limit of the inverse cubic root scaling law is, therefore, attributed to a volume fraction where the effective particle diameter d_{eff} is completely filled with the real particle diameter d itself and consequently the scaling law switches to the one-component-like problem with $\lambda = d$. Due to the scaling behaviour, this method is limited to spherical colloidal particles.

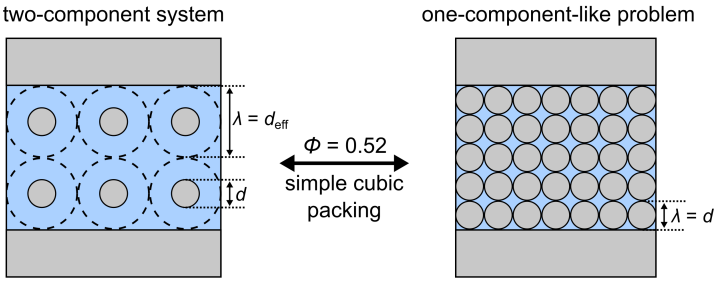

Figure 4.4: Left: In two-component systems, the particles strongly repel each other and accommodate their effective particle diameter d_{eff} to the available space which is defined by the particle number concentration n_p;
Right: The limit of scaling law at a volume concentration of $\phi = 0.52$. In this case, the particles start to touch and the wavelength λ is equal to the real particle diameter d.

4.3.3 Structuring in suspensions of charged nanoparticles

Due to the low ionic strength and high suface charges of the NPs, the interparticle interactions U_{el} are highly repulsive. We attribute the particles (with its effective diameter) to have a simple cubic arrangement of the particles within the confinement and in bulk since this reflects the least dense packing and the interparticle distance d in this case is at maximum. If the packing factor would be different, the wavelength λ would differ from the effective diameter d_{eff} in bulk, too ($\lambda \neq d_{\text{eff}}$). Unfortunately,

there are little direct experimental observations of the liquid structuring under confinement. Monte Carlo simulations of charged spherical particles confined between charged walls, however, resulted in simple cubic packing when the surface potential was set to $\phi = -160\,\mathrm{mV}$, however, hexagonal packing was obtained for wall with a surface potential of $\phi = -80\,\mathrm{mV}$ [99].

To account for that, an extrapolation towards a packing factor of $\phi = 0.74$ was performed. This reflects the packing factor for a hexagonal close packing, the densest possible packing factor of spherical particles. The obtained particle diameter d after extrapolation are $10.3 \pm 0.3\,\mathrm{nm}$, $13.2 \pm 0.5\,\mathrm{nm}$, and $21.6 \pm 0.3\,\mathrm{nm}$ for Ludox SM, Ludox HS and Ludox TM, respectively. For the larger particles, namely Ludox HS and Ludox TM, the results suggests, that the assumption of a simple cubic arrangement should be considered, since better agreement between TEM and AFM values are obtained. Interestingly, assuming hexagonal closest packing increases the agreement between the two values for the smallest, Ludox SM particles. The smallest particles, however, show the highest polydispersity (with a coefficient of variation (CV) of 19 % from TEM measurements). More polydisperse samples show the tendency for insufficient ordered packing [83]. Also, the deviation from perfect spherical shape is more pronounced for smaller particles. This might explain the mismatch in the determined particle diameter d using AFM force measurements (with an extrapolation to simple cubic packing) as well as the deviation in the fitted slope α of the two-component scaling law. The Ludox SM particles, therefore, may highlight the need for spherical, low polydisperse systems, when using this approach. It remains unclear whether the assumption of a simple cubic packing is just a feature of the considered model or it reflects the real packing structure of the charged particles within the confined surfaces. In chapter 5, the surface charge of confined colloidal particles is varied and the interparticle ordering is further discussed. Despite the real packing structure still being unknown, assuming simple cubic packing of charged spherical particles results in a successful determination of the diameters of nanoparticles.

4.4 Conclusion

In this chapter, two different scaling laws of oscillatory forces induced by liquids under geometrical confinement were depicted. For classical one-component systems, such

as pure solvents, the wavelength λ of the measured oscillatory forces simply reflects the molecular diameter d perpendicular to the confining surface. In two-component systems, such as concentrated colloidal dispersions, λ is larger than the actual colloidal diameter d. It is shown, that the limit of the scaling law for two-component systems may be defined by simple packing arguments.

This definition was emphasised by measuring the oscillatory structural forces across suspensions of silica nanoparticles. The wavelength λ of the force profile depends on the particle volume fraction ϕ which is known as the inverse cubic root scaling law. An effective particle diameter d_{eff} was defined, as the maximum distance between the particles arranged by simple cubic packing. In the following gedankenexperiment, the concentration of the particles in suspension was increased to $\phi = 0.52$ using the $\lambda \propto \phi^{-1/3}$ dependency. This can be seen as the transition from the two-component system to a one-component-like problem where the scaling law switches to simply $\lambda = d$.

The determination of a particle diameter d is a direct result from this gedankenexperiment. The extrapolated wavelength λ equals the particles diameter d. Using transmission electron microscopy (TEM), this method was validated to obtain reliable values for spherical, inorganic nanoparticles. Only one single force measurement, with a known volume fraction of particles in the dispersion is needed, to determine the particles size. Assumptions used in this approach, however, limits its application to dispersions containing low polydisperse, spherical particles with the ability to measure oscillatory structural forces. In general, this requirements are fulfilled for charged, nano-sized objects at low amount of background salt.

4.5 Appendix

Fit results The values of the fit parameters typically vary with the same period of the force profile for different starting points of the fit. To account for this problem, the starting point of the fit is varied. Error bars refer to the standard deviations from all individual fits with different starting points in the force profile.

	ϕ	A	λ	ξ	h'
		$\mathrm{mN\,m^{-1}}$	nm	nm	nm
Ludox SM	0.0359	0.083 ± 0.013	29.0 ± 0.2	18.2 ± 1.0	12.9 ± 0.5
	0.0478	0.068 ± 0.014	25.3 ± 0.4	17.0 ± 1.3	7.6 ± 1.0
	0.0620	0.163 ± 0.007	24.1 ± 0.1	14.2 ± 0.2	4.9 ± 0.2
	0.0700	0.188 ± 0.004	21.9 ± 0.1	14.0 ± 0.1	4.6 ± 0.3
Ludox HS	0.0313	0.038 ± 0.008	37.9 ± 0.3	38.3 ± 3.7	17.1 ± 0.9
	0.0423	0.045 ± 0.007	34.0 ± 0.2	38.4 ± 2.9	15.6 ± 0.7
	0.0646	0.068 ± 0.007	29.6 ± 0.3	34.8 ± 1.6	12.3 ± 0.9
	0.0881	0.058 ± 0.006	25.8 ± 0.1	35.6 ± 1.9	10.0 ± 0.2
Ludox TM	0.0312	0.035 ± 0.022	61.6 ± 5.4	41.1 ± 5.4	34.5 ± 15.1
	0.0422	0.027 ± 0.032	57.4 ± 4.7	49.8 ± 13.4	28.3 ± 12.4
	0.0532	0.026 ± 0.010	52.2 ± 1.4	54.8 ± 8.3	20.9 ± 4.0
	0.0646	0.033 ± 0.013	47.9 ± 1.6	63.9 ± 10.1	20.7 ± 4.8

Table 4.2: Fit parameters extracted from fitting the experimental data to the oscillatory structural force, eqn. 4.1

5 Oscillatory structural forces across dispersions containing micelles with variable surface charge

Similar content is contained in a draft of a manuscript which is in preparation and will be submitted for publication in the near future. Michael Ludwig, Ramsia Geisler, Philipp Ritzert, Sylvain Prévost, and Regine von Klitzing, *in preparation*.

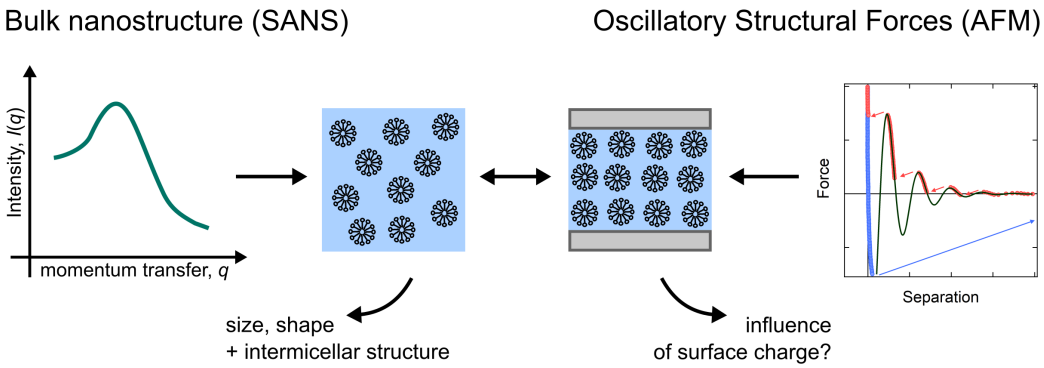

Abstract

When surfaces interact through concentrated colloidal dispersions, oscillatory structural forces often arise due to a specific structuring of colloidal particles. Although this type of force was studied intensively, the effect of the particles' surface charge is still poorly understood. In this chapter, we explore micellar dispersions containing a mixture of nonionic and anionic surfactants. Small-angle neutron scattering (SANS)

reveals the self-assembly of surfactant mixtures into mixed micelles with variable surface charge, from pure uncharged surfactants up to a proportion of 35 % anionic surfactant. Oscillatory structural forces across these dispersions, as probed between silica surfaces using colloidal-probe atomic force microscopy (CP-AFM), can be adjusted by the volume fraction as well as the surface charges of the micelles.

A preferred structuring of the micelles in bulk and under confinement is confirmed in SANS and AFM experiments, respectively. By introducing surface charges onto intrinsically uncharged micelles, the bulk intermicellar distance increases until the electrostatic repulsion forces the micelles into a specific structure. There, the mean distance between charged micelles D^* relates to the micellar volume fraction via the inverse cubic root law as $D^* \propto \phi^{-1/3}$. The micelle structuring in bulk and under confinement are compared to gain further insight. While uncharged micelles reduce their mean intermicellar distance under confinement, no such compressibility is observed once the micelles are charged. Introducing surface charges also enhances the amplitude of oscillatory structural forces due to stronger electrostatic repulsions of the micelles with the equally charged confining surface. This effect, however, is not represented in bulk scattering experiments.

5.1 Introduction

Chapter 2 introduced oscillatory structural forces across colloidal dispersions containing one type of objects as dispersed phase. Furthermore, dispersions containing multiple components were investigated. When mixing the uncharged triblock copolymer Pluronic F108 with anionic sodium dodecyl sulfate (SDS) surfactants, both components form complexes that lead to a depletion attraction [145]. Other research reports on the mixing of negatively charged silica nanoparticles with anionic poly(acrylic acid) (PAA) polyelectrolytes [146], where each component is able to induce oscillatory structural forces on its own. More pronounced oscillatory structural forces occur due to the adsorbtion of polymers onto the nanoparticles - although both components carry the same charge [147]. Recent work reports on a depletion attraction induced via formation of mixed micelles from nonionic Pluronic P123 triblock-copolymers and SDS [148].

Oscillatory structural forces across dispersions containing uncharged particles are theoretically described by statistical mechnanics [149] and density functional theory [150]. There, the particles interact via a hard-sphere potential. These theories led to the development of semiempirical analytical expressions [100, 101] using scaled particle theory [151, 152]. The expressions dervied for hard-sphere interactions do not apply to charged particles because the oscillatory structural force is strongly affected by the long-ranged electrostatic interactions between the particles. The wavelength λ of the force osciallations relates particles' volume fraction ϕ as $\lambda \propto \phi^{-1/3}$ due to geometrical considerations. This inverse cubic root scaling law allows to determine the aggregation numbers of various ionic surfactants [142, 153] and the diameters of charged solid nanoparticles [141], see also chapter 4. The question arises if this scaling law is universal for all charged particles or if it changes with the particles' surface charge. Kralchevsky *et al.* [61] recently reviewed theories of oscillatory structural force in charged and uncharged particles elucidating that the transition point between uncharged and charged particles is still poorly understood, experimentally as well as theoretically.

Intrinsically charged solid nanoparticles are inappropriate candidates to study the transition point between charged and uncharged particles because their material properties determine the surface charge. Addition of salt or modifications in pH alter the effective surface charge density, always affecting the ionic strength and with that the screening behaviour of the surrounding medium. Furthermore, agglomeration of the charge-stabilized particles occurs at high ionic strength.

To overcome these challenges, this chapter presents a systematic study of mixtures of uncharged and charged surfactants at different ratios in the form of self-assembled micelles with variable surface charge. This approach seems particularly promising since the system builds on a known hard sphere fluid and surface charges are subsequently introduced. The main system of interest is composed of the nonionic surfactant Tween20 and the anionic surfactant SDS. Anionic surfactants were chosen to form negatively charged micelles that do not adsorb onto the negatively charged surfaces. Moreover, the well-known nonionic surfactant BrijL23 is investigated to allow comparison with Tween20. First, small-angle neutron scattering (SANS) yields size and shape of individual micelles, micellar surface charge and bulk structuring in micellar dispersions. Second, colloidal-probe atomic force microscopy (CP-AFM) studies the oscillatory structural forces across these micellar dispersions. Correlations between

the bulk nanostructure and oscillatory structural forces are discussed in terms of micellar volume fraction and surface charge of the individual micelles. It is demonstrated how the doping of initially uncharged surfactant micelles enables a precise tuning of the oscillatory structural forces.

5.2 Results and Discussion

The bulk structure of micellar dispersions (5.2.1) and direct force measurements across these dispersions (5.2.2) are described before the interplay between bulk nanostructure and oscillatory structural forces is discussed (5.2.3).

The main part contains the analysis of pure Tween20 micelles followed by the investigation of mixed Tween20-SDS micelles. Moreover, pure micellar dispersions of either BrijL23 or SDS surfactants are investigated. The analysis is attached as Appendix of this chapter.

5.2.1 Bulk structure and interactions in micellar dispersions

The bulk properties of the micellar dispersions are studied using small-angle neutron scattering (SANS). Especially mixed surfactant systems are known to form micelles with many different morphologies. SANS is a powerful tool to probe the size and shape of individual micelles as well as intermicellar structuring and interactions *in situ*. This study aims to describe the structuring of micelles by analysis of the structure factor $S(q)$. In order to extract the structure factor $S(q)$, a precise description of the form factor $P(q)$ of individual micelles is needed. Theoretical background on the analysis of SANS data can be found in section 3.2.2.

Pure nonionic micelles The self-assembly of Tween20 in aqueous solution was studied at high surfactant concentrations (c(Tween20) = 106 - 286 mM)) in order to obtain pronounced intermicellar structuring. Previous studies by other groups depicted the self-assembled structures either as globular core-shell micelles [154] or as core-shell ellipsoids [155, 156].

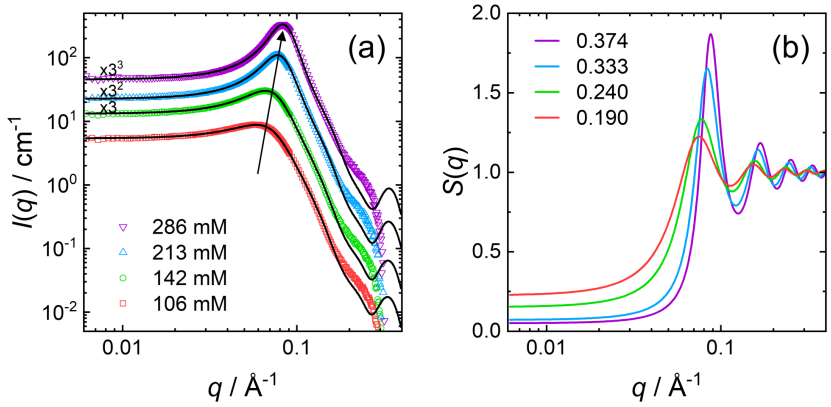

Figure 5.1: (a) SANS data for pure Tween20 micellar dispersions at various concentrations. Symbols are experimental scattering data. The black solid lines are model fits to eqn. 3.13. Data sets are scaled by the factors in black for clarity. (b) Extracted structure factors $S(q)$ from the model fits at different volume fractions ϕ. Same colour indicates same samples in panels (a) and (b).

In this work, SANS data of pure Tween20 are quantitatively analysed by a core-shell ellipsoid model (Fig. 5.1 (a)). The black solid lines display the model fits to the corresponding data sets, according to eqn. 3.13. Overall, the model fits and the experimental data points are in excellent agreement. The small distances that are probed at high q-values (*e.g.* molecular inhomogeneities between water and surfactant head-groups in the shell) are not described by the simple core-shell model assuming homogeneous scattering from cores and shells. Therefore, deviation between fit and data points at high q-values is expected. The scattering curves follow a similar shape at all concentrations measured. The extracted structure factor $S(q)$ (Fig. 5.1 (b)) becomes more pronounced with increasing Tween20 concentration, *i.e.* the structure factor peak increases with Tween20 concentration. This denotes stronger intermicellar structuring at higher surfactant concentrations. Apart from the peak intensity, also the peak position shifts towards higher q-values (see arrow in Fig. 5.1 (a)) and with that to smaller intermicellar distances at higher Tween20 concentrations. The peak shift resulting from the intermicellar interactions with increasing volume fraction is even more clearly visible in the $S(q)$ profiles extracted from the model fits (Fig. 5.1 (b)). The scattering curves of Tween20 are similar to the ones of the linear and well-known nonionic BrijL23 surfactants (Fig. 5.13, Appendix) indicating a similar shape and type of interactions between pure nonionic micelles.

Formation of mixed nonionic-anionic micelles After describing the bulk nanostructure of pure micelles, the effect of mixing nonionic Tween20 and anionic SDS surfactants is investigated. According to my knowledge, no SANS study on the formation of mixed micelles from these two surfactants has been reported in literature so far. Ideally, both surfactant species distribute homogeneously and form mixed nonionic-anionic micelles (Fig. 5.2).

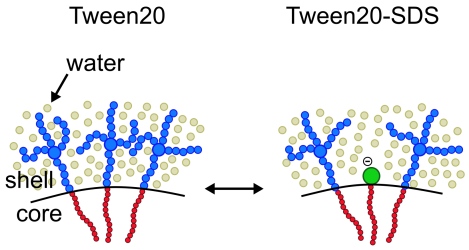

Figure 5.2: (a) Proposed distribution of surfactants. Surfactants are assumed to be homogeneously distributed to form mixed nonionic-anionic micelles.

Fig. 5.3 (a) shows the SANS scattering data of mixed micelles from nonionic Tween20 and anionic SDS surfactants. Four different mixing ratios of SDS and Tween20 are investigated. The composition ranges from the pure nonionic surfactants ($X = 0.00$) up to a proportion of 35 mol% of anionic SDS surfactants ($X = 0.35$).

The data clearly reveal the effect of substitution of nonionic with anionic surfactants on the intermicellar structuring. With increasing X, *i.e.* at higher amounts of anionic surfactant, the structure factor peak intensifies while the general shape of the scattering curves remains similar. The low impact on the curve shape confirms no significant architecture modifications of the single micelles upon admixing SDS. The intermicellar structuring is clearly visible in the extracted structure factors $S(q)$ (Fig. 5.3 (b)). At volume fractions of $\phi = 0.190$ - 0.215 (red lines) the peak position shifts towards lower q-values at higher mixing ratios X (see red arrow). Also, the structure factor intensifies along with the peak shift. Fig. 5.3 (b) contains another set of extracted structure factors (blue lines) at higher volume fractions $\phi = 0.333$ - 0.352. Interestingly, a higher SDS proportion has less influence on the structure factor at higher volume fractions of micelles. Not only does the peak position remain constant (see blue arrow), but also the peak intensity and peak width are only slightly affected.

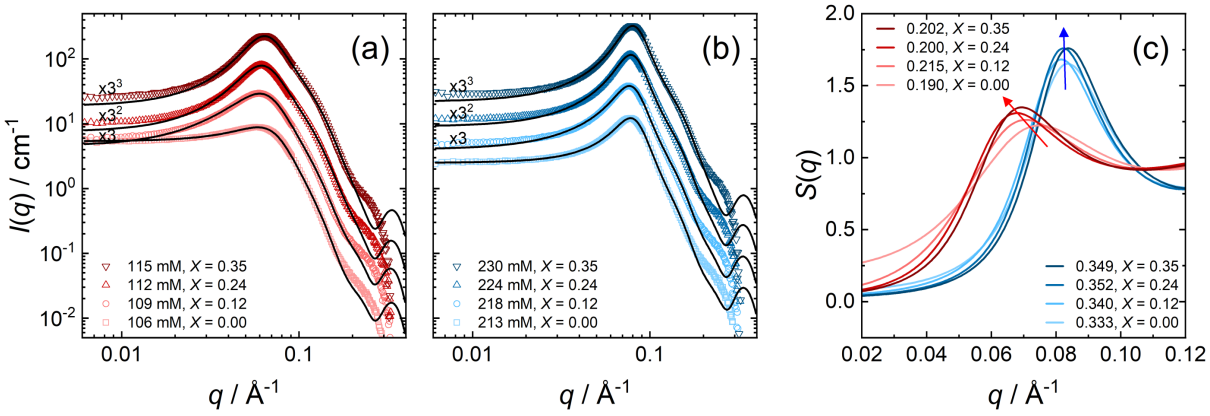

Figure 5.3: SANS data from mixed Tween20-SDS dispersions at similar surfactant concentrations ((a) $c = 106$ - 115 mM, and (b) $c = 213$ - 230 mM) but at varying mixing ratios X. Symbols are experimental data, black solid lines are model fits to eqn. 3.13. Data sets are scaled by the factors in black for clarity. (c) Extracted structure factors $S(q)$ from the model fits. The red data set is extracted from the data shown in panel (a) at $\phi = 0.190$ - 0.215. The structure factors shown in blue are from SANS data in panel (b) at $\phi = 0.333$ - 0.352.

Summary of fit parameters Table 5.1 summarises the fit results for the pure Tween20 and mixed Tween20-SDS surfactant micelles. The fit parameters of pure BrijL23 and pure SDS surfactant micelles can be found in Table 5.6 and Table 5.7, respectively (Appendix).

The hydrophobic core of pure Tween20 micelles is modelled with a fixed equatorial radius r_{eq} of 1.67 nm. Core axial ratios x_c of 1.72 - 2.21 indicate the formation of prolate ellipsoids. The thicknesses of the hydrated shells t_s are 1.72 - 1.81 nm. At higher Tween20 concentrations the micellar size decreases slightly, from an effective radius r_{eff} of 4.05 nm at 106 mM to 3.75 nm at 286 mM. Pure Tween20 micelles comprise smaller micelles compared to the pure BrijL23 micelles (Table 5.6, Appendix). The effective radii r_{eff} of pure BrijL23 micelles range from 4.28 - 4.02 nm. The aggregation numbers N_{agg} of Tween20 are with values of 92 - 102 higher than for pure BrijL23 micelles, which contain 58 - 61 surfactants per micelle. Pure BrijL23 micelles are less elliptical compared to pure Tween20 micelles, with core axial ratios x_c of 1.69 - 1.89. Pure SDS micelles (Table 5.7, Appendix) are much smaller than the pure nonionic micelles, with effective radii r_{eff} between 1.90 -2.06 nm. The aggregation number N_{agg} of SDS micelles increases with increasing surfactant concentration from 87 at 72 mM SDS to 105

X	c	ϕ	x_c	t_s	$\rho_s \cdot 10^{-6}$	r_{eff}	N_{agg}	z	β
	mM			nm	Å^{-2}	nm			
0	106	0.190	2.21	1.81	5.06	4.05	94		
	142	0.240	2.14	1.77	5.08	3.99	95		
	213	0.333	1.93	1.72	5.10	3.85	92		
	286	0.374	1.72	1.72	5.18	3.75	102		
0.12	109	0.215	2.21	1.85	5.22	4.10	88	10	0.11
	146	0.270	2.17	1.82	5.21	4.05	90	9	0.10
	218	0.340	2.01	1.74	5.20	3.90	96	9	0.09
0.24	112	0.200	2.02	1.78	5.27	3.94	87	15	0.18
	149	0.278	2.12	1.78	5.37	3.99	85	14	0.16
	224	0.352	1.99	1.71	5.33	3.86	93	12	0.13
0.35	115	0.202	1.92	1.71	5.44	3.83	81	17	0.21
	153	0.268	1.96	1.71	5.47	3.85	82	16	0.20
	230	0.349	1.93	1.65	5.44	3.77	89	14	0.16

Table 5.1: Summary of SANS fit parameters. The mixing ratio X is defined as X = [SDS] / ([SDS] + [Tween20]). c is the total surfactant concentration ([SDS]+[Tween20]). Fitted values: volume fraction ϕ, axial ratio of the core x_c, shell thickness t_s, shell scattering length density ρ_s, and the charge per micelle z. Calculated values: the effective radius r_{eff} (eqn. 3.15), the aggregation number N_{agg} (eqn. 3.16), and the fractional charge β (eqn. 3.17).

at 359 mM SDS.

In addition to the properties of pure Tween20 micelles, Table 5.1 reveals different effects when mixing nonionic Tween20 and anionic SDS surfactants. At all mixing ratios X investigated, the nonionic-anionic micelles can be modelled as core-shell ellipsoids. The equatorial radius r_{eq} of the core was set to 1.67 nm as for the pure nonionic micelles. The core ellipticity x_c appears robust at different SDS ratios. All micelles show axial ratios of the core between 1.72 - 2.21. The shell thickness t_s reduces slightly with increasing SDS fraction in the mixed micelles, from 1.85 - 1.65 nm. The effective radii r_{eff} of all Tween-SDS micelles are in the range of 4.10 - 3.77 nm, *i.e.* they vary within

less than 9 %. The aggregation numbers N_{agg} decrease with increasing SDS ratio. The values vary within 15 % from pure nonionic micelles to a SDS ratio of $X = 0.35$. With increasing X, the surface charge per micelle z and with that the fraction charge β clearly increases. While pure nonionic micelles are uncharged, up to 17 surface charges per micelle (*i.e.* 21 % of all surfactant molecules in the micelle) are detected at a mixing ratio of $X = 0.35$.

Literature reports on different properties of pure Tween20 micelles. Aggregation numbers range from 349 [154], 90 [155], 70 [90], to 22 [156] accompanied by varying micelle dimensions. Our results are in good agreement with the results obtained by Penfold *et al.* [155]. The aggregation numbers and core radii are similar while only the shell thickness is around ≈ 0.5 nm thicker. The difference probably results from the purity of the Tween20 used. In our work, we use commercially available Tween20, whereas the surfactants in the study of Penfold *et al.* were specifically synthesised. The Tween20 used in this work was analysed by mass spectrometry identifying two major products (Fig. 5.10, Appendix). Both products have predominantly C_{11} alkyl chains but a different distributions of head groups (chemical structures in Fig. 5.11, Appendix): One head group contains 26, the other one 11 EO groups. The surfactant mixture contains 20 EO groups in average, as indicated by the manufacturer (details in Table 5.2, Appendix). The presence of larger head groups located in the shell might explain the thicker shell when using the commercial product. Interestingly, BrijL23 surfactant molecules form larger micelles compared to Tween20 although BrijL23 micelles comprise a lower aggregation number. This indicates a stronger hydration of the linear BrijL23 headgroups compared to the branched headgroups of Tween20. The aggregation number of SDS increased with its concentration. This trend of increasing aggregation number is well-known for SDS [157, 158].

When mixing nonionic Tween20 and anionic SDS surfactant molecules, mixed micelles of similar sizes are formed. At higher SDS ratios, one would initially assume mixed micelles to decrease in size because the sulfate headgroup being around 30 times smaller compared to the EO headgroup of a Tween20 molecule. The smaller headgroup volume of SDS, however, is almost completely compensated by an increased hydration of the shell at higher SDS ratios. Hydration of the headgroup does not only affect the size of the micelle but also the contrast of the shell and with that its scattering length density (SLD). Material balance equations from known molecular volumes and SLDs reveal a slight mismatch of core volumes if only comprised of hydrocarbon chains and the

SLD of the shell assuming homogenous scattering. An inhomogenous distribution of EO-groups within the micelles may describe this phenomenon. Some EO-groups may enter the hydrophobic core and accumulating at the core-shell interface. This was already demonstrated for $C_{12}E_6$ surfactants using molecular dynamics simulations [159], or for $C_{18}E_{100}$ using SANS [160].

The counterion condensation plays an important role on the micellar surface charge. Although the charge per micelle z increases with increased mixing ratio X, the strength of counterion binding to the micelles varies. At a mixing ratio of $X = 0.12$, the fractional charge of the micelles is $\beta = 0.09$ - 0.11. The similarity of both values indicate that most counterions are dissociated from the sulfate headgroup. Exact calculations (degree of SDS dissociation = β / X, assuming all SDS molecules to incorporate into the micelles) show that at $X = 0.12$ between 78 % - 92 % of the SDS headgroups are dissociated. At $X = 0.35$, the counterion condensation elevates and only between 44 % - 59 % of SDS headgroups remain dissociacted. Thus, the surface charge and the mixing ratio do not linearly depend on each other. Electrostatic limitations, similar to the Manning limiting law [161], influence the effective surface charge. The role of the counterion condensation is well known from studies on other mixed micelles, such as from nonionic $C_{12}E_{23}$ surfactant with SDS [162], or from nonionic sugar based surfactants with SDS [163].

The distribution of charged sites across the micelles surface indicates that both types of surfactants (nonionic-anionic) are homogenously distributed in the mixed micelles formed. Homogeneous distribution might not only be favoured by the hydrophobic effect of the alkyl chains but also by favourable interactions between the EO and sulfate headgroups. This is assumed, since favourable interactions between EO- and sulfate groups were previously reported for linear PEO polymers and SDS surfactants dissolved in water revealed strong polymer-surfactant complexes being formed [164–167].

Bulk intermicellar structuring The major focus of this study is on the bulk structuring of the micelles. This is evaluated from the Lorentzian fit to the respective structure factors $S(q)$ according to eqn. 3.18. The mean intermicellar distance D^* is calculated from the position of the peak maximum $q_{\max}$ as $D^* = \frac{2\pi}{q_{\max}}$. The inverse cubic root scaling law estimates the mean intermicellar distances D^* for charged particles (eqn. 5.1),

considering packing arguments knowing the effective particle radius r_{eff} and the particle volume faction ϕ.

$$D^* = f\, r_{\mathrm{eff}}\, \phi^{-1/3} \tag{5.1}$$

The type of particle packing determines the value of the pre-factor f. For a simple cubic packing $D^* = n_p^{-1/3} = (4/3\pi)^{1/3} r_{\mathrm{eff}}\, \phi^{-1/3}$, so that $f = 1.612$ (see also eqn. 4.3 in chapter 4). Experimentally, a $f = 1.436$ is found for microemulsions [168]. In Fig. 5.4, the bulk intermicellar distance D^* is normalised to the effective diameter ($2r_{\mathrm{eff}}$) for comparison to the micelles number density n_p. Data are obtained by fitting the structure factors $S(q)$ of pure Tween20 (Fig. 5.1 (b)), and mixed Tween20-SDS (Fig. 5.4 (b)). Detailed analysis of pure BrijL23 (Fig. 5.13 (b)) and pure SDS Fig. 5.14 (b)) can be found in the Appendix.

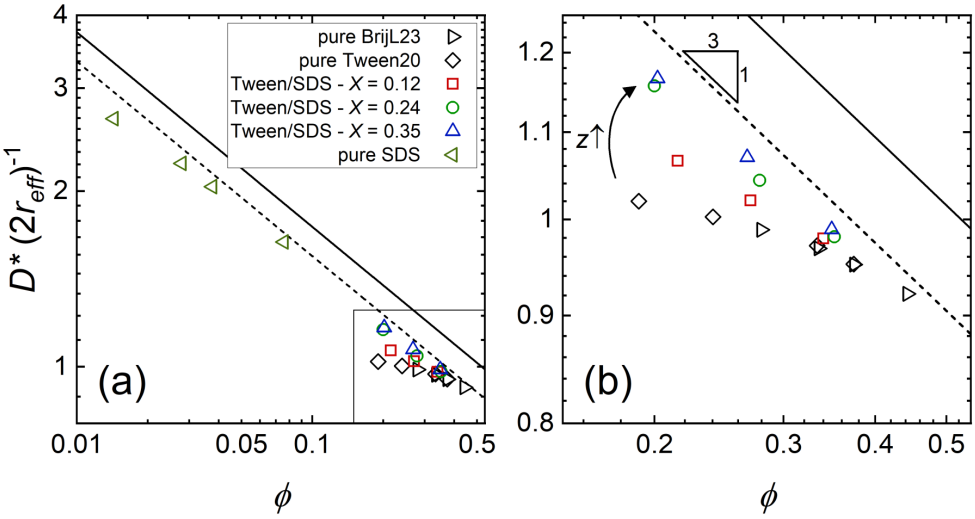

Figure 5.4: The bulk intermicellar distance D^* normalised to the effective radius r_{eff} in dependency of the volume fraction ϕ in various micellar dispersions. The lines are predictions according to eqn. 5.1 with a pre-factor of $f = 1.436$ (dashed line) and $f = 1.612$ (solid line). Panel (b) is a magnification of the box in panel (a). The arrow in panel (b) highlights the influence of a higher surface charge z.

Both types of pure nonionic micelles (BrijL23 and Tween20) follow the same volume fraction dependency. The intermicellar distance varies only very little with the volume fraction ϕ. At higher ϕ, the values of nonionic micelles approach the scaling be-

haviour for charged particles. This is not surprising, since at close packing geometries ($\phi \gtrsim 0.52$) the interparticle distances of charged and uncharged particles will not differ. In the same way, it is reasonable that the mean distance D^* between micelles at $\phi \approx 0.35$ changes only slightly by introducing surface charges to the micelles. At $\phi \approx 0.20$, the intermicellar distance subsequently increases with increasing ratio of SDS, *i.e.* with increasing micellar surface charge. The electrostatic repulsion between micelles increases with the amount of surface charges. As a result, the micelles form a stronger intermicellar structuring. The same behaviour is observed for pure anionic SDS micelles at smaller volume fractions ϕ. Due to the increased surface charge of pure micelles, this specific structuring can be maintained towards smaller volume fractions ($\phi \approx 0.01$). When the micelles carry a certain amount of surface charge - in this study mixed Tween20-SDS micelles with $X = 0.24$ and $X = 0.35$ as well as pure SDS micelles - they follow the inverse cubic root scaling law proposed for charged particles (eqn. 5.1 with $f = 1.436$, dashed line in Fig. 5.4).

At high volume fractions ($\phi > 0.3$), the intermicellar distance is smaller than the effective diameter of the micelle as indicated by a value below 1 of $D^* (2r_{\text{eff}})^{-1}$. The effective radius is calculated assuming the ellipsoid occupying the same volume as a sphere. Closer intermicellar distance than the effective diameter may result from a preferred alignment of the ellipsoids. The micelles ellipticity ranges from 1.36 - 1.58, due to the elliptical hydrophobic core but a constant shell thickness. However, no explicit anisotropy was observed in the scattering detector image. Furthermore, the apparent structure factor $S'(q)$ determined by the decoupling approximation may comprise some inaccuracies at volume fractions and ellipticities used in this study [169].

5.2.2 Oscillatory structural forces across micellar dispersions

In this part, the colloidal probe atomic force microscopy (CP-AFM) technique is used to measure forces between two confining surfaces across these micellar dispersions. The forces are measured for the pure Tween20 (Fig. 5.5), pure BrijL23 (Fig. 5.15, Appendix), and pure SDS (Fig. 5.17, Appendix) micellar dispersions. The effect of admixing the anionic surfactant SDS is demonstrated for the Tween20-SDS mixtures (Fig. 5.6).

The normalised interaction forces $\frac{F}{R}$ between two surfaces at separations h are fitted to

the oscillatory structural force F_{osc} as described in chapter 3.

$$\frac{F}{R}(h) = \frac{F_{osc}}{R}(h) = -A \cdot \exp\left(-\frac{h}{\xi}\right) \cdot \cos\left(\frac{2\pi}{\lambda}(h - h')\right). \tag{5.2}$$

In the presence of nonionic surfactants, adsorption of surfactant onto the confining surfaces may occur [170]. The absolute values of the surface separation h should, therefore, be treated with care.

Pure nonionic micelles Fig. 5.5 shows the force profiles between silica surfaces across nonionic Tween20 micellar dispersions measured by CP-AFM.

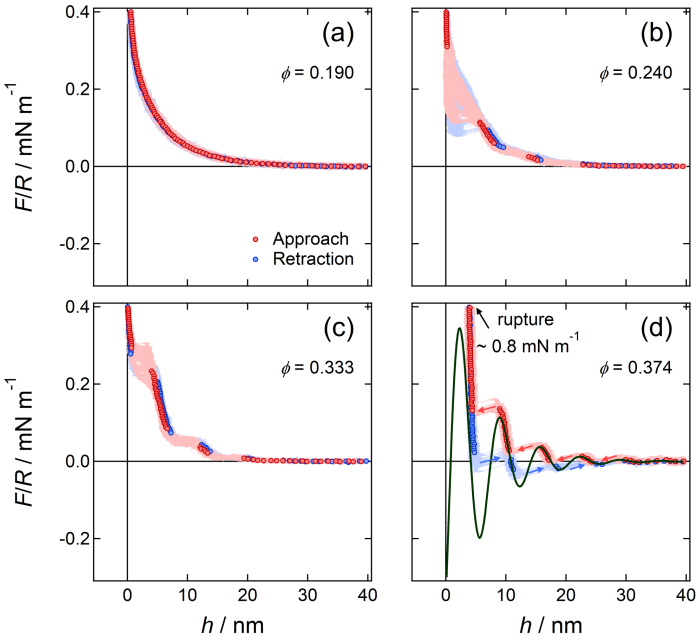

Figure 5.5: Interaction forces between silica surfaces across nonionic Tween20 micellar dispersions. Red dots are data points for approaching surfaces; blue dots are data points for retracting surfaces. Experimental data are fitted to eqn. 5.2 (black, solid line).

The combination of all data points (bright colours) is shown along with smoothed, time-averaged data (larger dots). Unsmoothed data are included to highlight that the transitions (also referred to as "jumps") between stable force branches are often not clearly pronounced. Jumps in the force profile appear once the gradient in the force

profile exceeds the cantilever spring constant. It is difficult to distinguish between adsorbed surfactant molecules on the surface and depleted micellar particles. A study reports on strong adsorption of nonionic surfactants on silica surfaces, often forming hemicylinders [170]. In contrast to this, nonionic BrijL23 micelles show slower formation and decomposition kinetics compared to Tween20 micelles [171]. BrijL23 micelles are, therefore, considered more stable. Force profiles across dispersions of BrijL23 micelles are shown in Fig. 5.15, Appendix. There, the transitions between stable force branches are more pronounced.

Oscillatory structural forces emerge with increasing volume fraction of Tween20. At a volume fraction of $\phi = 0.240$, almost no oscillatory structural forces could be detected which is in agreement with a former study [91]. Only at the highest volume fraction of $\phi = 0.374$, clear oscillatory structural forces with at least five oscillations in the force profiles are observed and fitted to a damped oscillatory profile (eqn. 5.2). The high viscosity of the dispersion enhances the thermal noise in the measurement substantially. At surface separations below $h \approx 4.8$ nm, adsorbed surfactant on the silica surfaces may be confined. This layer then ruptures at $F/R \approx 0.8\,\mathrm{mN\,m^{-1}}$.

Mixed nonionic-anionic micelles Interaction forces between silica surfaces across mixed Tween20-SDS micelles are shown in Fig. 5.6. The plots are arranged in a manner that: (i) the surface charge per micelle z increases from left to right; (ii) the volume fraction ϕ increases from top to bottom. The concentrations and mixing ratios are the same as used in the SANS experiments (Table 5.1). However, contrarily to SANS samples prepared in D_2O, AFM samples are prepared in H_2O. No significant change in micellar structure is assumed or expected.

Oscillatory structural forces are observed across all these systems. The magnitude and range varies according to the charge per micelle z and volume fraction ϕ. At the smallest volume fraction ($\phi = 0.190$) and smallest ratio of anionic surfactants in the system ($X = 0.12$), only one oscillation occurs (Fig. 5.6 (a)). The oscillatory structural force becomes stronger due to two reasons: higher micellar surface charge and higher volume fraction. In consequence, the oscillatory structural force is most pronounced in Fig. 5.6 (i) showing at least four distinct force oscillations up to surface separation above 40 nm.

Additional SDS in the micelles enhances the electrostatic repulsion between individual

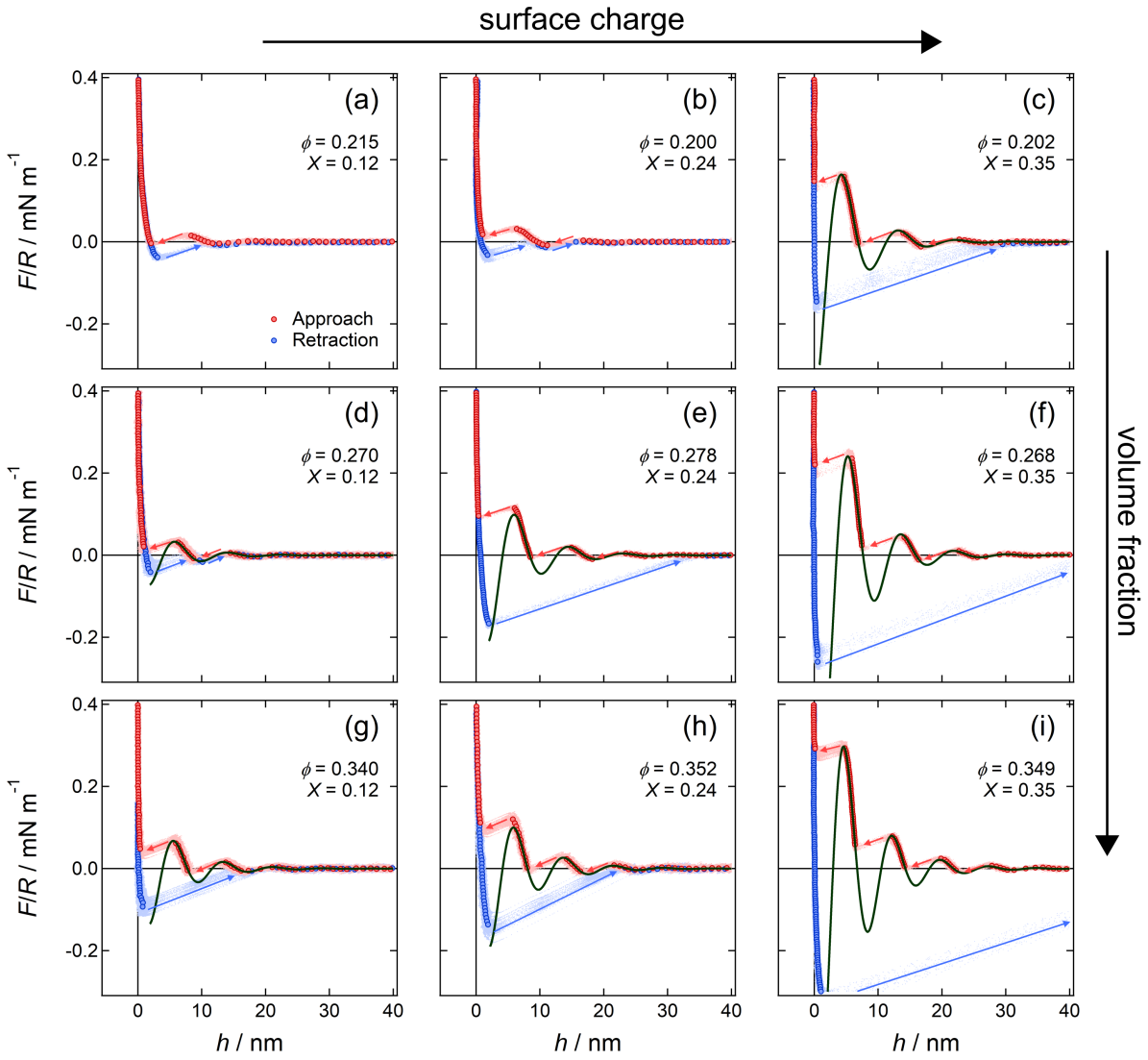

Figure 5.6: Interaction forces between silica surfaces across mixed Tween20-SDS micellar dispersions for different volume fractions ϕ and different mixing ratios X. Red dots are data points for approaching surfaces, blue dots for retracting surfaces. Experimental data are fitted to eqn. 5.2 (black, solid line)

micelles and also amplifies the interaction between the micelles and the negatively charged confining surfaces. As a result and unlike for pure nonionic Tween20 micelles, no adsorbed surfactant layer is observed. Moreover, the oscillatory structural forces across mixed micellar dispersion are better defined compared to the pure Tween20 micelles, discussed in Fig. 5.5.

5.2.3 Comparison of the bulk nanostructure and oscillatory structural forces

Further description of the oscillatory structural force involves the discussion of the fit parameters deduced from eqn. 5.2. Main focus is on the fit parameters from pure Tween20 (Fig. 5.5) and mixed Tween20-SDS (Fig. 5.6) micellar dispersions. Due to the weakly expressed oscillatory structural force in Figs. 5.5 (a) - (c) and 5.6 (a) , (d), no fit results can be obtained for these samples. In the following, parameters describing the oscillatory structural forces (*i.e.* dispersion properties under geometrical confinement) from AFM are compared to the parameters obtained from the Lorentzian fits (eqn. 3.18) to the first peak of the structure factor $S(q)$ (*i.e.* dispersion properties in bulk) from SANS experiments. The description of the intermicellar distance further includes parameters from pure BrijL23 (Fig. 5.16, Appendix) und pure SDS (Fig. 5.18, Appendix) micellar dispersions.

Mean intermicellar distance The mean intermicellar distance under confinement is considered as the wavelength λ of the oscillatory structural force. These values are compared to the mean intermicellar distance in bulk D^*, extracted from the structure factors peak positions $q_{\max}$ as $\frac{2\pi}{q_{\max}}$.

Fig. 5.7 compares the intermicellar distances obtained in bulk and under confinement. The results are further compared to an existing analytical semiempirical model for the oscillatory structural force based on numercial results for hard-sphere fluids to describe the wavelength λ from uncharged micelles. Similar to eqn. 5.1, the wavelength λ depends on the number density of micelles n_p. The use of the effective radius r_{eff} transfers this to a dependecy on the volume fraction ϕ as [101]:

$$\frac{\lambda}{2r_{\text{eff}}} = 2\pi \left(4.45160 + 7.10586\phi - 8.30671\phi^2 + 8.29751\phi^3\right)^{-1}. \tag{5.3}$$

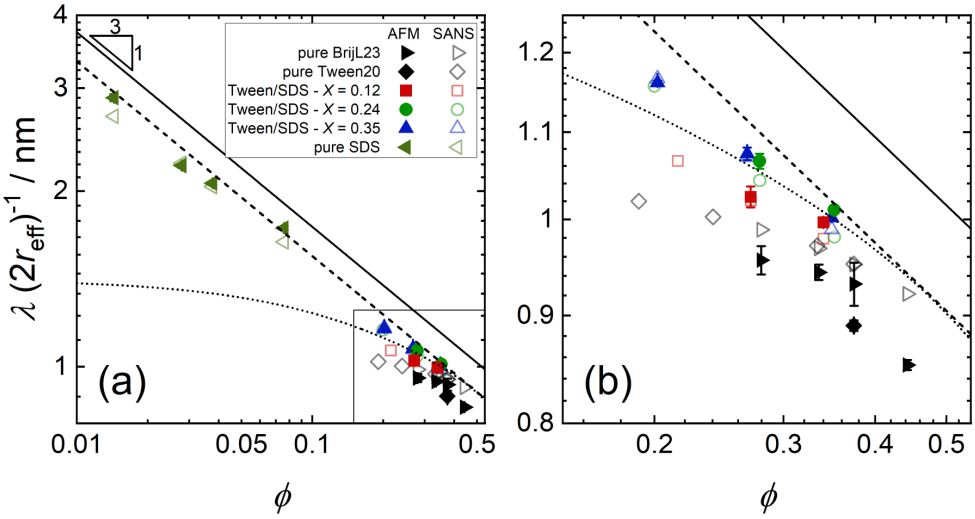

Figure 5.7: Comparison of the intermicellar distances: under confinement as AFM wavelength λ (filled symbols) and in bulk dispersion from SANS according to $D^* = \frac{2\pi}{q_{max}}$ (empty symbols, see also Fig. 5.4) for all studied systems as a function of their volume fraction ϕ. Distances are normalised to the effective diameter ($2r_{eff}$) of the micelles. The lines are predictions according to eqn. 5.1 with a pre-factor of $f = 1.436$ (dashed line) and $f = 1.612$ (solid line). The dotted line is a prediction according to the theory for uncharged particles (eqn. 5.3).

Here, the mean intermicellar distances between uncharged micelles (Tween20 and BrijL23) in bulk (empty black symbols in Fig. 5.7) and under confinement (filled black symbols in Fig. 5.7) are up to $\approx 10\,\%$ smaller than predicted by eqn. 5.3 (dotted line in Fig. 5.7). However, both, experimental data and the analytical semiemperical model, follow the same qualitative trend.

Interestingly, the bulk intermicellar distance D^* of uncharged micelles is larger than the intermicellar distance under confinement λ. Obviously, uncharged micelles are compressible under confinement. The results from SANS and AFM deviate stronger, *i.e.* show higher compressibility, at higher volume fractions of micelles ϕ. In contrast to the uncharged micelles, micelles obey the same intermicellar distance as in bulk and are not compressible once they are charged (filled, coloured symbols in Fig. 5.7). This incompressibility is observed for mixed Tween20-SDS as well as for pure SDS micellar dispersions. The wavelengths λ of all charged micelles are described by their mean intermicellar distance in bulk D^*. When the micelles are highly charged, the inverse

cubic root scaling law is found (eqn. 5.1 with $f = 1.436$). This is in good agreement with a pervious study on pure SDS micelles, where $f = 1.396$ is found [68].

Contrary to this, solid colloidal particles, like silica nanoparticles, were considered with a prefactor of $f = 1.612$ (eqn. 4.3), assuming perfect simple cubic packing. This approach was used in chapter 4 to extract the particle diameter d from the measured wavelength λ and the particles' volume fraction ϕ. However, when trying to calculate the exact prefactor f by measuring the particle diameter d and volume fraction ϕ, this picture is less clear. Due to uncertainties in the diameters d of the solid nanoparticles, the prefactor f contains a large uncertainty, too. A precise determination of the real particle structuring via the prefactor f is not possible for solid nanoparticles, in chapter 4. In contrast to the solid nanoparticles, the self-assembled surfactant micelles are less polydisperse. Therefore, the pre-factor f can be determined more precisely and a deviation from a simple cubic packing (with $f = 1.612$) is observed. One can only speculate if solid colloidal particles and surfactant micelles obtain a different interparticle structuring. If so, this might be due to surfactant micelles being a more dynamic and softer compared to solid nanoparticles.

Correlation length In AFM, the correlation length under confinement is extracted as decay length ξ from the fit to the oscillatory structural force. In bulk, thus from SANS results, a correlation length is extracted from the full-width at half maximum of the structure peak Δq as $\frac{2}{\Delta q}$. Here, the results for pure Tween20 and mixed Tween20-SDS micelles are shown. Results for the pure BrijL23 and pure SDS micellar dispersions can be found in the Appendix (Fig. 5.16 (c), and Fig. 5.18 (c), respectively)

Fig. 5.8 compares both correlation lengths. The analytical semiempirical model for the oscillatory structural force of uncharged micelles yields the decay length ξ depending on the effective particle radius r_{eff} and the volume fraction ϕ as [101] (dotted line in Fig. 5.8):

$$\frac{\xi}{2r_{\text{eff}}} = \left(4.78366 - 19.64378\phi + 37.37944\phi^2 - 30.59647\phi^3\right)^{-1}. \tag{5.4}$$

In this study, the decay length ξ is almost constant for all dispersions under confinement, irrespective of the micellar surface charge z or volume fraction ϕ. The hard-sphere repulsion is the dominant parameter for the decay length in the confined dis-

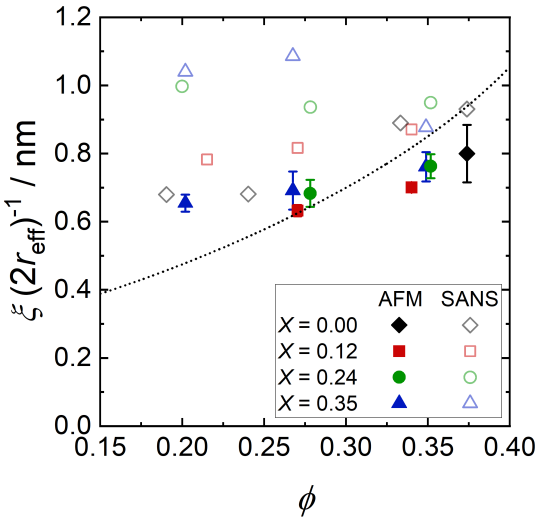

Figure 5.8: Comparison of the correlation lengths: under confinement as AFM decay length ξ (filled symbols) and in bulk dispersion from SANS as $\frac{2}{\Delta q}$ (empty symbols) for all Tween20-SDS systems studied as a function of their volume fraction ϕ. X represents the mixing ratio of both surfactants. The dotted line is a prediction according to the theory for uncharged particles (eqn. 5.4).

persions and introducing surface charges does not affect these values. The correlation length of the confined dispersions (filled symbols in Fig. 5.8) agrees well with the correlation length determined for uncharged micelles in bulk (empty, grey diamonds in Fig. 5.8).

Unlike the decay length ξ, the bulk correlation length $\frac{2}{\Delta q}$ increases with increasing micellar surface charge z. The effect of electrostatic interactions becomes especially important at lower volume fractions, *i.e.* when the micelles are more separated. This is only observed between charged micelles in bulk but not under confinement. Interestingly, no such deviation between the correlation lengths in bulk and under confinement is found for solid, charged nanoparticle suspensions [87]. The decrease of the correlation length under confinement compared to bulk in micellar dispersions might again be contributed to the micelles being more dynamic and softer.

Structuring strength The amplitude A of oscillatory structural forces is often related to only the interparticle interactions in dispersions. It was, however, demonstrated that the interaction between confining surfaces and the particles alters the amplitude

A [98, 99], meaning that the amplitude does not only depend on properties of the bulk dispersions. Here, the results for pure Tween20 and mixed Tween20-SDS micelles are shown. Results for the pure BrijL23 and pure SDS micellar dispersions can be found in the Appendix (Fig. 5.16 (a), and Fig. 5.18 (a), respectively)

Fig. 5.9 compares the amplitude A with the strength of the intermicellar structuring in bulk calculated from the excess intensity of the structure factor peak: the maximum intensity of the structure factor is normalised to 1: $S_{max} + S_0 - 1$. This was done, since $S(q) = 1$ indicates a random intermicellar distribution with only the form factor $P(q)$ contributing to the scattering intensity.

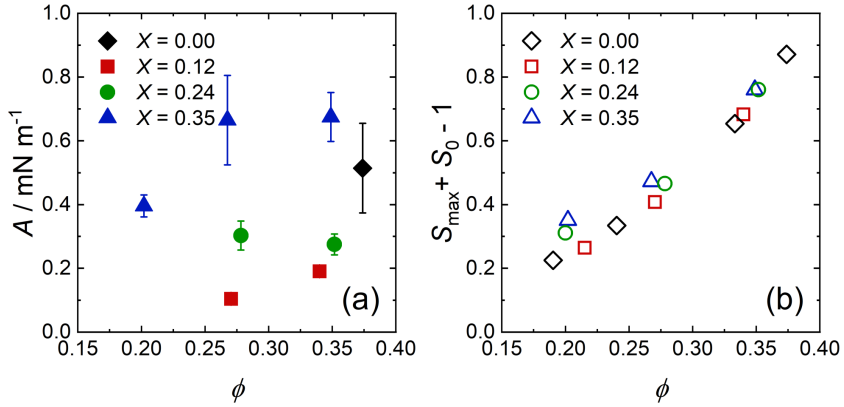

Figure 5.9: Comparison of (a) the amplitude A from force measurements and (b) SANS $S_{max} + S_0 - 1$ for all Tween20-SDS systems studied as a function of their volume fraction ϕ. X represents the mixing ratio of both surfactants.

The amplitude A of the oscillatory structural forces enhances at higher surface charges of the micelles (Fig. 5.9 (a)). The effect of ϕ on A is almost negligible, compared to the influence of the surface charge. The amplitude from the oscillatory structural force across pure Tween20 micelles ($X = 0.00$) is neglected in the discussion. There, the first layer in the force profile is considered as an adsorbed layer of nonionic surfactant surfactant so that the data cannot be compared. Unlike the effect on A, micellar surface charges do almost not impact the intensity of the structure factor peak in bulk. It is dictated by the volume fraction ϕ. This means, that structuring of the micelles in bulk is due to hard-sphere repulsions, at $\phi \gtrsim 0.20$. Both values, A and $S_{max} + S_0 - 1$, cannot be compared, since A strongly depends on the interactions of the micelles with the confining surfaces. This information cannot be obtained from experiments with bulk small-angle scattering experiments.

5.3 Conclusion

This chapter shows that mixed nonionic-anionic micelles form when mixing Tween20 and SDS surfactant stock solutions at different ratios. The samples investigated range from pure nonionic micelles to micelles containing up to 35 % SDS. Self-assembled micelles are of similar size and shape. Variation of the mixing ratio adjusts the surface charge. Moreover, pure nonionic BrijL23 and pure anionic SDS surfactant solution were investigated for comparison. Oscillatory structural forces were successfully measured across these micellar dispersions. The force profile may be well adjusted by a variation of the micellar surface charge as well as the micelle volume fraction.

Comparison of the dispersion properties in bulk and under geometrical confinement reveals different behaviours of uncharged and charged micelles. Charged micelles are forced into a preferred structuring by electrostatic repulsion. The intermicellar distance in bulk D^* scales with the volume fraction ϕ as $D^* \propto \phi^{-1/3}$. This distance does not change under confinement as seen in the wavelength λ of the oscillatory structural force ($\lambda = D^*$). The bulk intermicellar distance D^* of uncharged micelles is less sensitive to the micellar number density since the micelles interact only via hard-sphere interactions. Furthermore, uncharged micelles can be compressed under geometrical confinement ($\lambda < D^*$). Differences in the bulk structuring of charged and uncharged micelles become less pronounced at higher volume fractions ($\phi \gtrsim 0.20$) since hard-sphere interactions starts to dominate the bulk micellar structuring. In contrast to the results for bulk structuring, the oscillatory structural forces are very sensitive to the amount of surface charges per micelle. This is explained by stronger interactions between the micelles and the confining surfaces when the micelles carry more surface charges. This, in turn, strongly affects the amplitude of the oscillatory structural forces. The effect of the confining surfaces will be further investigated in the next chapter.

These findings can be transferred to various colloidal systems. In general, this study shows that the inverse cubic root scaling law is not a universal property of all colloidal dispersions. This dependency is obtained when the interactions between dispersed particles are highly repulsive.

5.4 Appendix

Mass spectra of Tween20 Fig. 5.10 shows the measured mass spectra of Tween20 in different matrices. Peaks in the spectra can be described as a mixture of PME and IPE. The different peaks of each set are spaced by a mass/charge ratio of 44.03, corresponding to the mass of ethylene oxide (EO, C_2H_4O) unit.

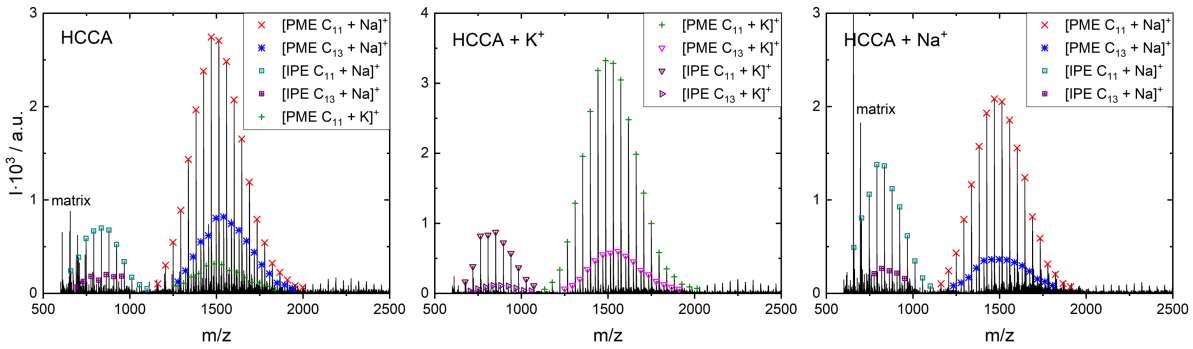

Figure 5.10: MALDI-TOF spectra of Tween20 from a pure HCCA matrix and from HCCA matrices upon addition of K^+ or Na^+ salt.

Previous studies revealed that the commercially available Tween20 is often a mixture of various compounds [172–177]. The two major components found in this study are shown in Fig. 5.11. In order to understand the occurrence of both compounds, the synthesis pathway of the surfactant has to be reviewed. Upon dehydration of sorbitol, which is typically the first step in the synthesis of polysorbate surfactants, a mixture of sorbitan and isosorbide can be obtained. Further steps in the synthesis (ethoxylation and esterification) then lead to the two compounds that were found in this study: the polysorbate monoester (PME) and the isosorbide polyethoxylate (IPE).

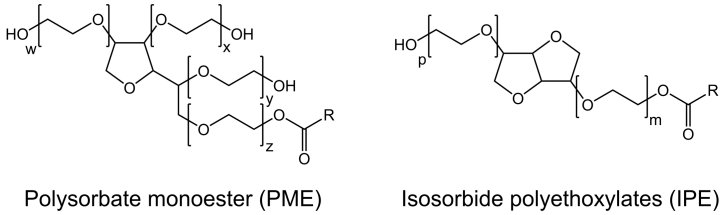

Figure 5.11: Molecular structures of the two major components found in commercially available Tween20: the polysorbate monoester (PME) and isosorbide polyethoxylate (IPE). $-$R denotes the alkyl chain, $-C_{11}H_{23}$.

Table 5.2 summarizes the key findings. In all measurements, PME as well as IPE components were identified. The aliphatic alkyl chain is predominantly C_{11} with a small amount of C_{13} chains also present. The number of EO units is roughly 25 - 26 for the PME molecules (w+x+y+z) and 10 - 11 for IPE molecules (p+m). Interestingly, the mean value over all PME and IPE molecules is approximately 20 - 22 which is similar to the value given by the manufacturer (= 20). The Tween20 surfactants are, therefore, modelled assuming the head-group consisting of 20 EO groups.

matrix	PME : IPE$^{(a)}$	C_{11} : $C_{13}$$^{(b)}$	w+x+y+z	p+m
HCCA	4.5 : 1	3.3 : 1	25.7 ± 0.1	10.8 ± 0.1
HCCA + K^+	2.0 : 1	4.7 : 1	25.6 ± 0.1	10.7 ± 0.1
HCCA + Na^+	5.7 : 1	6.1 : 1	25.6 ± 0.1	10.7 ± 0.1

Table 5.2: $^{(a)}$ Determined as the ratio of the peak areas from molecules with a C_{11} alkyl chain; $^{(b)}$ Determined as the ratio of the peak areas of PME

Mass spectra of BrijL23 Fig. 5.12 shows the measured mass spectra of BrijL23 in HCCA matrix and without and upon addition of different salts. Similar to the case of Tween20, the peaks of different sets are spaced by the mass value of one EO group.

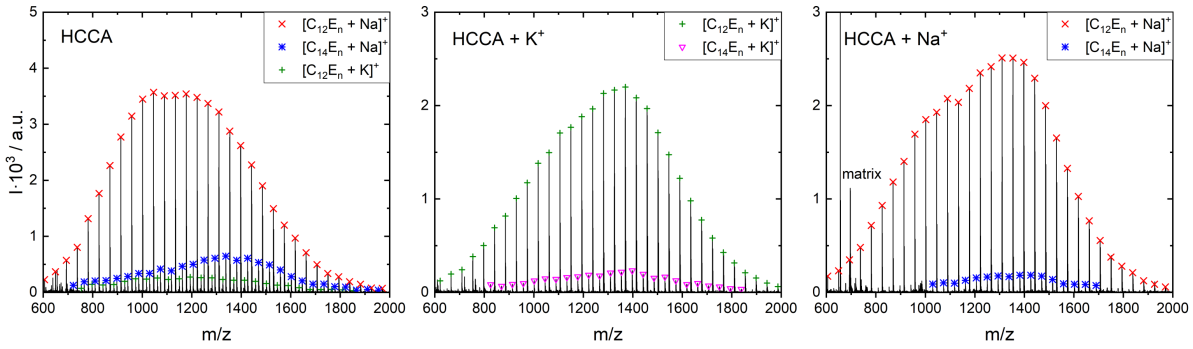

Figure 5.12: MALDI-TOF spectra of BrijL23 from a pure HCCA matrix and from HCCA matrices upon addition of K^+ or Na^+ salt.

Table 5.3 summarizes the two key findings. The alkyl chain length is predominantly C_{12}, with a small portion of C_{14} chains present. The number distribution of EO groups between single surfactants can be described as Gaussian shaped. The mean value of EO group per surfactant is roughly 23, the value given by the manufacturer. This result confirms the findings from previous literature studies [172, 175].

matrix	$C_{12}:C_{14}$	EO-units
HCCA	8 : 1	21.6 ± 0.1
HCCA + K^+	42 : 1	23.6 ± 0.1
HCCA + Na^+	14 : 1	24.2 ± 0.1

Table 5.3: Key findings from mass spectrometry measurements of BrijL23: the ratio between C_{12} and C_{14} alkyl chains of the hydrophobic tail and the total number of EO units per molecule

Surfactant properties The following tables summarise the properties used to fit the small-angle neutron scattering profiles from dispersions of surfactant micelles.

chemical / formula	*cmc*	*M*	density	v_m
	$mM\,L^{-1}$	$g\,mol^{-1}$	nm^3	nm^3
SDS / $C_{12}H_{25}SO_4Na$	8.3 [178]	288.4	1.01	0.410
Tween20 / $C_{58}H_{11}O_{26}$	0.059 [136]	1128	1.150	1.805
BrijL23 / $C_{58}H_{118}O_{24}$	0.09 [137]	1198	1.115	1.809

Table 5.4: Critical micelle concentrations *cmc*, molar mass *M* as given by the manufacturer, the determined density and the molecular volume v_m of the used surfactants

group	v_m	ρ
	nm^3	$10^{-6}\,Å^{-2}$
$C_{12}H_{25}$	0.351	-0.39
$C_{11}H_{23}$	0.324	-0.39
CH_2CH_2O	0.0616	0.67
D_2O	0.0301	6.34

Table 5.5: Molecular volumes v_m are given in [179, 180]. Neutron scattering length densities ρ of the surfactants alkyl chains $C_{11}H_{23}$ and $C_{12}H_{25}$, ethylene oxide (EO, CH_2CH_2O) contained in the headgroups, and the solvent D_2O are calculated with the NIST NCNR SLD calculator (www.ncnr.nist.gov).

Small-angle neutron scattering results of pure BrijL23 micellar dispersions The bulk structure of BrijL23 micelles was determined using light scattering [181], small-angle neutron scattering [180, 182], small-angle X-ray scattering [183] and Monte Carlo simulations [184]. Here, own measurements were conducted for consistency. Similar to the analysis of Tween20 micelles, a core-shell ellipoid model, as discussed in section 3.2.2, was used.

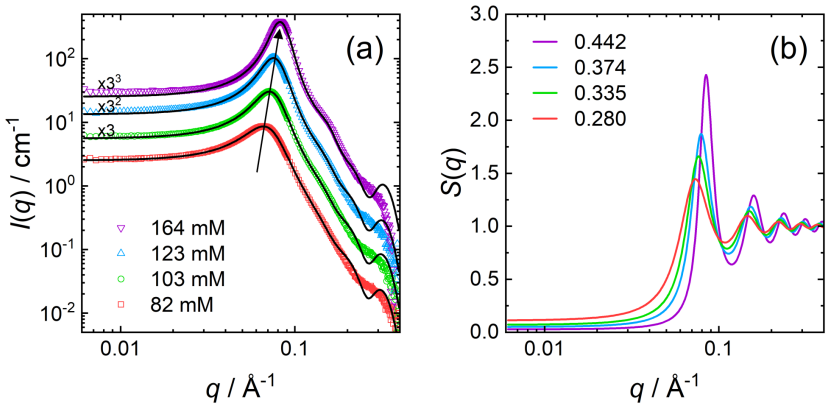

Figure 5.13: (a) SANS data for BrijL23 micellar dispersions at various concentrations. Symbols are experimental scattering data, the black solid lines are the results from the fitting procedure as described in the text. Data sets are scaled by the factors in black for clarity. (b) Extracted structure factors $S(q)$ from the model fits at different volume fractions ϕ.

c mM	ϕ	x_c	t_s nm	ρ_s 10^{-6} Å^{-2}	r_{eff} nm	N_{agg}
82	0.280	1.89	2.17	5.42	4.28	58
103	0.335	1.82	2.12	5.41	4.21	58
123	0.374	1.77	2.08	5.38	4.14	59
164	0.442	1.69	2.00	5.35	4.02	61

Table 5.6: Parameters obtained for BrijL23 micellar dispersions. Fit results from the SANS analysis: axial ratio of the core x_c, shell thickness t_s, scattering length density of the shell ρ_s and the volume fraction ϕ. Calculated values: effective radius r_{eff} and the aggregation number N_{agg}.

Small-angle neutron scattering results of pure SDS micellar dispersions In oder to fit the SANS data measured for pure SDS micellar dispersions some assumptions were adjusted. The critical micelle concentration *cmc* is known to depend on the total SDS surfactant concentration. The *cmc* is, therefore, calculated from activity measurements [185, 186] for each SDS concentration separately. Knowing the *cmc* allows the calculation of the micelle volume fraction ϕ. Best fit results were obtained assuming only scattering from the core ($t_s = 0$). The shape of the core was modelled as oblate ellipsoid ($r_{eq} > r_p$), with the polar radius r_p fixed to 1.67 nm.

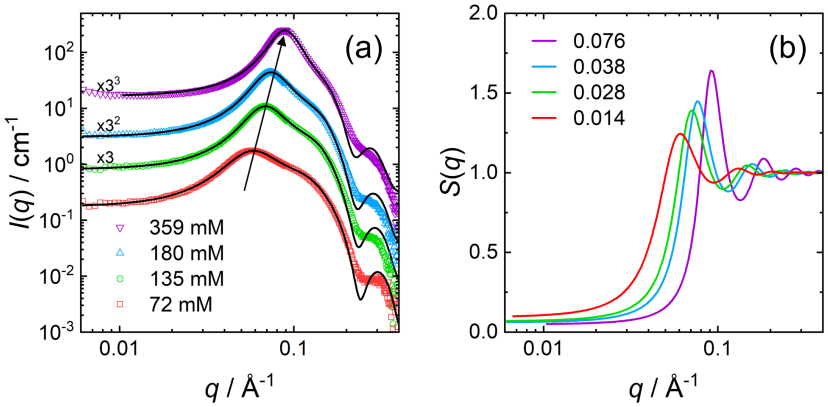

Figure 5.14: (a) SANS data for SDS micellar dispersions at various concentrations. Symbols are experimental scattering data, the black solid lines are the results from the fitting procedure as described in the text. Data sets are scaled by the factors in black for clarity. (b) Extracted structure factors $S(q)$ from the model fits at different volume fractions ϕ.

c mM	ϕ	cmc mM	r_{eq} nm	z	r_{eff} nm	N_{agg}
72	0.014	3.9	2.03	28	1.90	87
135	0.028	2.8	2.13	41	1.96	93
180	0.038	1.6	2.18	45	1.99	95
359	0.076	1.0	2.30	65	2.06	105

Table 5.7: Parameters obtained for SDS micellar dispersions. Fit results from the SANS analysis: equatorial radius of the core r_{eq} and charge per micelle z. Calculated values: effective radius r_{eff} and the aggregation number N_{agg}.

Surface forces across BrijL23 micellar dispersions Although force profiles across BrijL23 micellar dispersion are already reported [91], our own measurements were conducted for consistency.

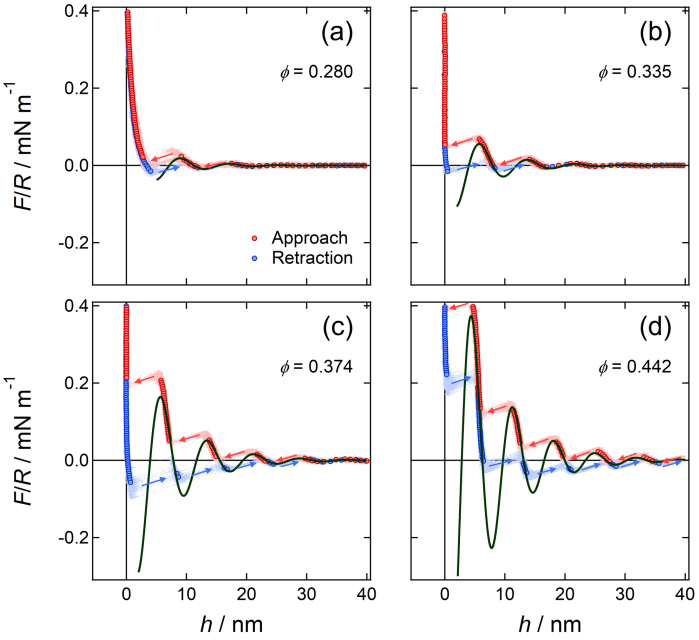

Figure 5.15: Interaction forces across BrijL23 micellar dispersions at various volume fractions ϕ. Red dots are data for approaching surfaces, blue dots for retracting surfaces. Experimental data are fitted as oscillatory structural force to eqn. 5.2 (black, solid line).

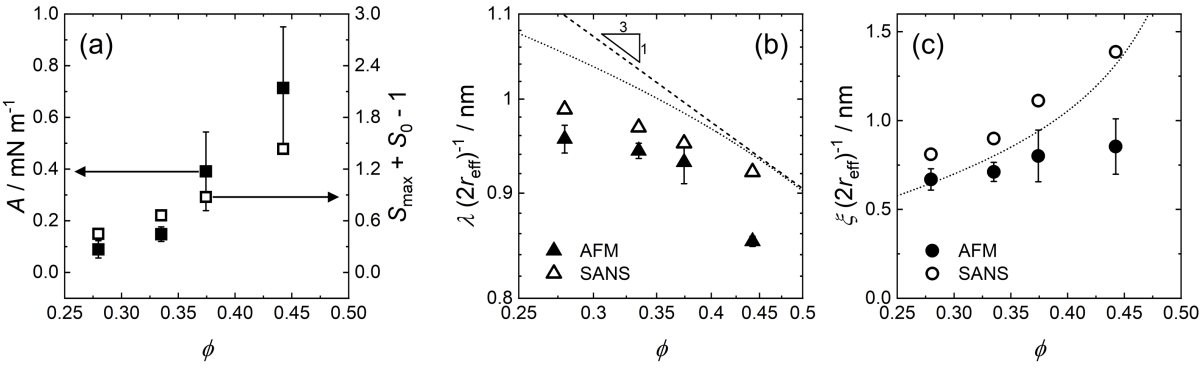

Figure 5.16: Fit parameters of the oscillatory structural force in dependency of the volume fraction ϕ of BrijL23 micelles. Parameters describing the oscillatory structural force are (a) the amplitude A, (b) the wavelength λ, and (c) the decay length ξ. These parameters are compared with parameters of the bulk dispersion obtained from fits to the structure peak $S(q)$ in Fig. 5.15: the ordering strength $S_{\max} + S_0 - 1$, the bulk intermicellar distance $\frac{2\pi}{q_{\max}}$, and the bulk correlation length $\frac{2}{\Delta q}$

Surface forces across SDS micellar dispersions Although force profiles across SDS micellar dispersion are already reported [67, 68], our own measurements were conducted for consistency.

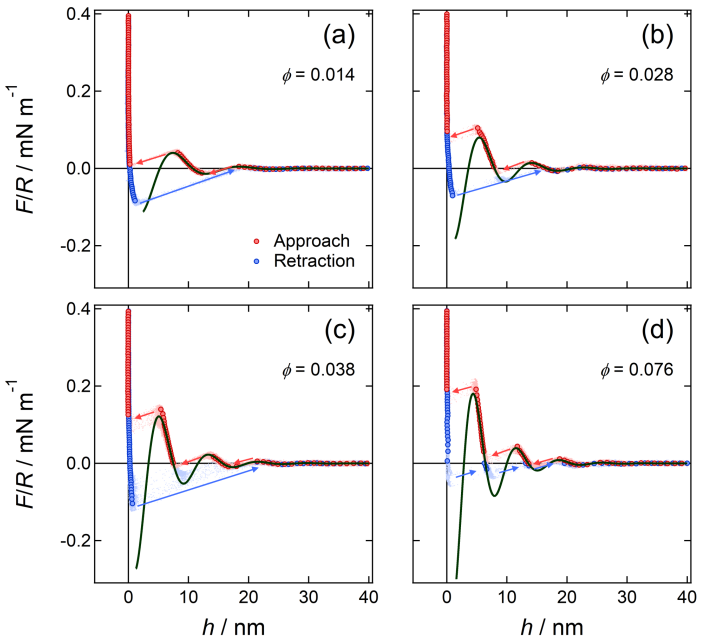

Figure 5.17: Interaction forces across SDS micellar dispersions at various volume fractions ϕ. Red dots are data for approaching surfaces, blue dots for retracting surfaces. Experimental data are fitted as oscillatory structural force to eqn. 5.2 (black, solid line).

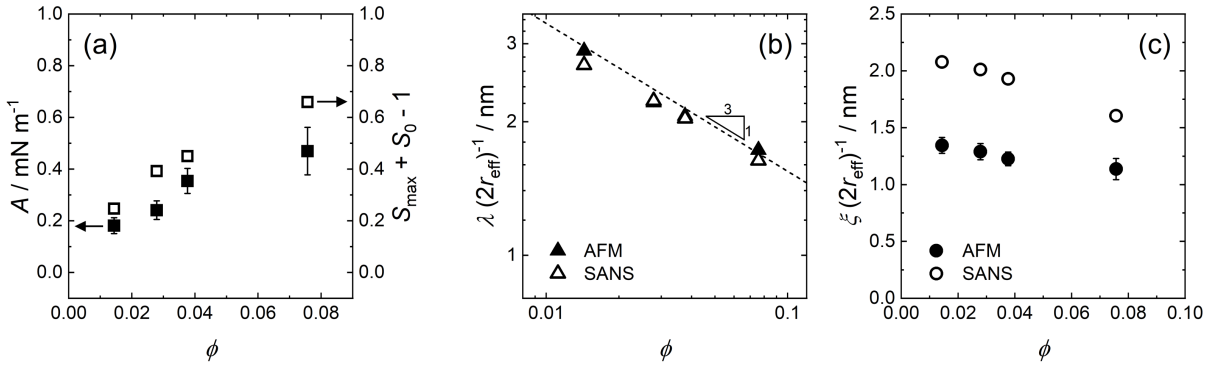

Figure 5.18: Fit parameters of the oscillatory structural force in dependency of the volume fraction ϕ of SDS micelles. Parameters describing the oscillatory structural force are (a) the amplitude A, (b) the wavelength λ, and (c) the decay length ξ. These parameters are compared with parameters of the bulk dispersion obtained from fits to the structure peak $S(q)$ in Fig. 5.17: the ordering strength $S_{\max} + S_0 - 1$, the bulk intermicellar distance $\frac{2\pi}{q_{\max}}$, and the bulk correlation length $\frac{2}{\Delta q}$

6 Superposition of double layer and structural forces

Similar content is published in "Untangling superposed double layer and structural forces across confined nanoparticle suspensions", Michael Ludwig and Regine von Klitzing, *Phys. Chem. Chem. Phys.*, **2021**, 23, 1325-1334. [187] doi:10.1039/D0CP05631F. Reproduced by permission of the PCCP Owner Societies.

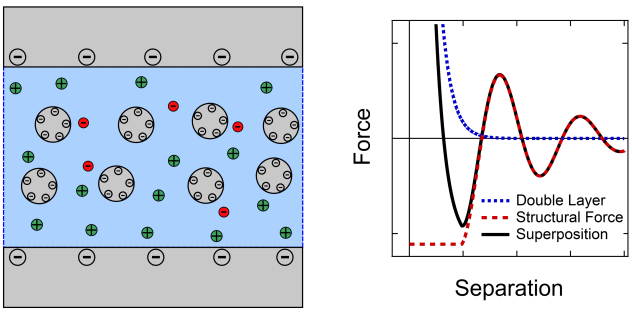

Abstract

The complete description of forces across confined colloidal dispersions is challenging due to the possible overlap of different force contributions. In this chapter, an attempt is made to untangle the interactions between charged surfaces across suspensions containing nanoparticles and monovalent salt. Interaction forces are measured using colloidal-probe atomic force microscopy (CP-AFM). The experimental force profiles are considered as a superposition of double layer and structural forces. In order to independently describe the decay of the double layer force, the ionic strength of the suspension is determined by electrolytic conductivity measurements. Jellium approximation is used to define the impact of the fluid on screening the surface potential.

There, the nanoparticles are considered homogeneously distributed across the fluid and screening is only carried out via the particles counterions and added salt. The structural force follows a damped oscillatory profile due to the layer-wise expulsion of the nanoparticles upon approach of both surfaces. The description of the oscillatory structural force is extended by a depletion layer next to the confining surfaces, with no nanoparticles present. The thickness of the depletion layer is related to the electrostatic repulsion of the charged nanoparticles from the like-charged surfaces. The results show that the total force profile is a superposition of independent force contributions without any mutual effects. Using this model describes the complete experimentally determined interaction force profiles very well from surface separations of a few hundred nanometres down to the surfaces being almost in contact.

6.1 Introduction

While a lot of work was spent on the description of oscillatory structural forces itself, *e.g.* in the previous chapters of this thesis, only a few research dealt with the role and superposition of DLVO-type forces - mainly the double layer forces - in such fluids. A first description of the interplay between double layer and depletion attraction was obtained for surfaces of two oil-droplets in a micellar solution [188]. Due to the presence of a depletion attraction, the interaction force profile deviates from a exponential decay, as typically observed for a pure double layer interaction. Recently, the interaction force profiles between charged silica surfaces in dispersions containing likely charged polyelectrolytes (polystyrene sulphonate, PSS) were modelled [81, 189]. There, the polyelectrolytes are treated as multivalent ions and non-linearised PB solution is assumed for the description of the short-ranged double layer force [190]. At larger surface separations oscillatory structural forces dominate the interaction force profile.

Treating dispersed colloidal particles as multivalent ions results in unexpectedly large screening leaving it a heavily discussed topic. Moreover, the complete depletion of the dispersed particles at small distances between the confining surfaces is still missing in the existing models.

In this chapter, it is demonstrated how superposed force contributions can be untangled. Therefore, interaction forces between charged silica surfaces in suspensions con-

taining nanoparticles and monovalent salt at various concentrations are measured. Additionally, the screening behaviour of suspensions is determined independently from electrolytic conductivity measurements. In that way, the double layer force could be extracted from the oscillatory structural force, leading to a deeper insight in the surface forces across concentrated colloidal dispersions.

Experimental approach In contrast to the experiments in chapter 4, only one type of silica nanoparticles (Ludox HS) is used. Monovalent salt is added to alter the ionic strength of the suspension. Most importantly, a higher force value is chosen for the onset of the constant compliance region. In previous experiments the surfaces are assumed to be in contact at $0.4\,\mathrm{mN\,m^{-1}}$. Here, the surfaces are expected to be in contact, once the normalised force excess $2.5\,\mathrm{mN\,m^{-1}}$ in order to overcome the double layer repulsion.

6.2 Modelling and fitting of interaction forces

The normalised interaction forces between two charged surfaces at separations h were fitted using a superposition of double layer F_{dl} and structural forces F_{str}, see section 3.

$$\frac{F}{R}(h) = \frac{F_{\mathrm{dl}}}{R}(h) + \frac{F_{\mathrm{str}}}{R}(h) \tag{6.1}$$

Due to the complexity of the present systems, different assumptions were made. Hereafter, these assumptions are explained in detail.

Double layer forces Superposition approximation is used to model the normalised double layer force $\frac{F_{dl}}{R}$ in dependence of the surface separation h as explained in section 2.2.3. The diffuse layer potentials ψ_{dl} of both confining silica surfaces are assumed to be equal, giving rise to a symmetric potential profile. The double layer force is described by eqn. 2.35 which can also be written as:

$$\frac{F_{\mathrm{dl}}}{R}(h) = 4\pi\epsilon\epsilon_0\kappa \left(\frac{4kT}{ze}\tanh\left(\frac{ze\psi_{\mathrm{dl}}}{4kT}\right)\right)^2 \cdot \exp(-\kappa h)\,. \tag{6.2}$$

The double layer force in eqn. 6.2 is described by two adjustable parameters: the diffuse layer potential ψ_{dl} and the Debye screening length κ^{-1}.

The Debye screening length κ^{-1} depends on the ion distribution in the electrical double layer. This is typically expressed via the ionic strength I. Here, the ionic strengths I of the NP suspensions are calculated using the jellium approximation (JA). A schematic representation of the JA is given in Fig. 6.1.

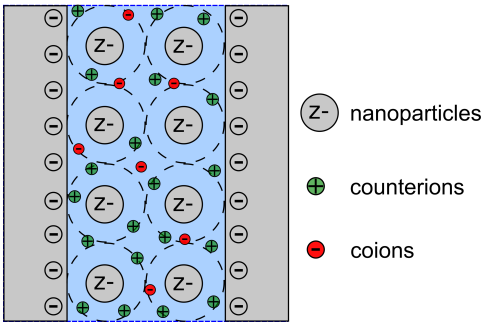

Figure 6.1: Schematic representation of the jellium approximation for dispersions containing charged NPs confined between charged walls. The NPs are assumed to be uniformly distributed across the fluid due to their repulsive interaction, while monovalent ions (the particles counterions and added salt) obey Boltzmann distribution due to the surface potential. As a result, the NPs *do not* contribute to Debye screening of the surfaces' electric field.

Historically, the term "jellium" was introduced for quantum mechanical description of quasi-free electrons in a solid where the positive atomic nuclei are assumed to be uniformly distributed in space [191]. This framework was later adopted for the description of colloidal systems at low concentrations of electrolyte [192, 193]. Given the picture in Fig. 6.1, two types of ions are considered: On the one hand, monovalent ions (counterions of the particles and added salt ions), and on the other hand the NPs themselves. Monovalent cations c_+ and anions c_- (with $z = 1$) obtain Boltzmann distribution. Their concentration next to a charged surface can be calculated via eqn. 2.22, see chapter 2. The dispersed NPs, however, are considered as a scaffold with the monovaltent ions distributed around. The concentration of NPs c_p is assumed constant and equal to its bulk concentration $c_{p,\infty}$.

$$c_p = c_{p,\infty} = \text{const.} \tag{6.3}$$

As a result, using the JA, the NPs are neglected from Debye screening. The ionic strength I is only depending on the concentrations of the monovalent ions c_i and can be directly calculated using eqn. 2.27. This in turn enables the Debye screening length κ^{-1} to be calculated via eqn. 2.26. This independent determination of the Debye screening length leaves the diffuse layer potential ψ_{dl} as the only free parameter that enters the fit to the double layer force.

The applicability of the JA will be further considered in section 6.4.1. In general discussions, the term "macroion" is used to describe the NPs, since this model can be extended to other colloidal systems, *e.g* to dispersions containing ionic micelles or polyelectrolytes.

Structural forces After subtraction of the fitted double layer force from the experimental data, the structural force was fitted to eqn. 6.4.

$$\frac{F_{\mathrm{str}}}{R}(h) = \begin{cases} \frac{F_{\mathrm{osc}}}{R}(h') \;=\; \text{const.}, & 0 < h \leq h' \\ \frac{F_{\mathrm{osc}}}{R}(h) = -A \cdot \exp\left(\frac{-h}{\xi}\right) \cdot \cos\left(\frac{2\pi}{\lambda}(h-h')\right), & h' < h < \infty \end{cases} \tag{6.4}$$

Combination of the oscillatory structural force ($h' < h < \infty$) with the depletion attraction ($0 < h \leq h'$) is referred to as the structural force. The total structural force is schematically illustrated in Fig. 6.2.

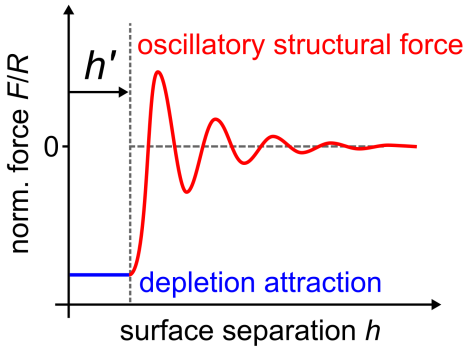

Figure 6.2: Schematic model of the total structural force. Below a certain offset h' the interaction switches from an oscillatory structural force to a depletion attraction.

First, the asymptotic behaviour was fitted using a damped oscillatory profile, see also chapter 2. This contribution is referred to as the oscillatory structural force, with the amplitude A, the decay length ξ, and the wavelength λ. The parameter h' corrects for the offset of the structural force. The oscillatory structural force is used to describe the structural force for surface separations h being larger than the offset h'.

At surface separations h smaller than the offset h', all nanoparticles are considered to be depleted from the vicinity of the surfaces, resulting in a constant depletion attraction. Here, the strength of the depletion attraction is set as a constant value. It is determined from the value of the fitted oscillatory structural force at the offset h', *i.e.* the first minimum of the oscillatory structural force, to ensure continuity between both scenarios.

6.3 Results

The ionic strength of each suspension used in this study is calculated from its electrolytic conductivity (section 6.3.1). Individual determination of the ionic strength eliminates it as free parameter in fitting of the double layer force.

Direct force measurements were carried out between silica surfaces in suspensions containing different amounts of nanoparticles (NPs) and monovalent salt (section 6.3.2). Interaction profiles are described as a superposition of double layer forces from the outer confining surfaces and structural forces induced by the confined NP suspensions.

6.3.1 Determination of the ionic strength of nanoparticle suspensions

In order to obtain the ionic strength of pure NP suspensions, their electrolytic conductivities were measured. The results for pure suspensions and suspensions with added NaCl are displayed in Fig. 6.3. In general, contributions to the conductivity are expected from protons H^+ and hydroxide-anions OH^-, as well as from the negatively charged silica nanoparticles NP^{Z-} including their sodium counterions Na^+.

The pH value of the suspension was determined as 9.2 (see Fig. 6.9, Appendix), revealing the concentrations of protons H^+ and hydroxide-anions OH^- to be rather low.

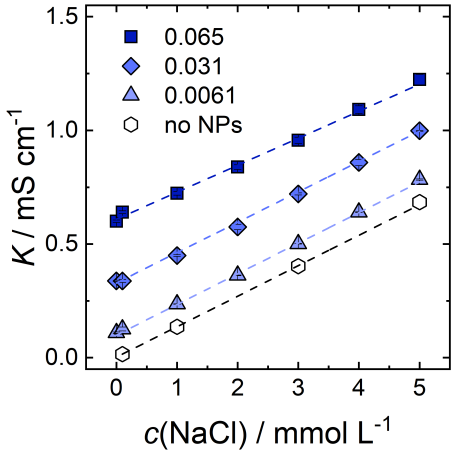

Figure 6.3: Electrolytic conductivities K of suspensions at varying volume concentrations of dispersed NPs as a function of added NaCl. Dotted lines are linear fits to the data.

Their contribution is neglected in the following. The mobility of the NPs is also small compared to the one of its Na^+ counterions. Consequently, the ionic strength of the pure NP suspensions is dominated by the NPs counterions. Ion-ion correlations, as described by the Kohlrausch law [194], are neglected. The concentration of Na^+ counterions $c_0(Na^+)$ in suspensions without addition of salt is, therefore, calculated by the limiting molar conductivity of the sodium counterions ($\lambda_+^0(Na^+) = 5.011\,\mathrm{mS\,m^2\,mol^{-1}}$) and the electrolytic conductivity without added salt K_0. Determined ionic strengths of the pure NP suspensions I_0 are summarised in Table 6.1.

$$c_0(Na^+) = \frac{K_0}{\lambda_+^0(Na^+)}, \quad I_0 = \frac{1}{2}\,c_0(Na^+) \tag{6.5}$$

The slopes b of all fitted curves are approximately the same, although a small deviation for the highest NP concentration is observed. Accounting for this deviation would decrease the calculated ionic strength in the system by less than 5 %. Added NaCl (within the measured concentrations) is, therefore, assumed to be completely dissociated and not to be adsorbed onto the NPs. The total ionic strength I can simply be calculated as the sum of the ionic strength of the pure NP suspension I_0 and the ionic strength from

$\phi\,(SiO_2)$	b	K_0	I_0
	$mS\,L\,mmol^{-1}\,cm^{-1}$	$mS\,cm^{-1}$	$mmol\,L^{-1}$
-	0.134 ± 0.001	0.002 ± 0.001	0.02 ± 0.01
0.0061	0.135 ± 0.002	0.099 ± 0.004	0.99 ± 0.04
0.031	0.135 ± 0.001	0.329 ± 0.006	3.28 ± 0.06
0.065	0.119 ± 0.005	0.609 ± 0.006	6.08 ± 0.06

Table 6.1: Parameters from the linear fit ($K = b\,c(\mathrm{NaCl}) + K_0$) on the conductivity data shown in Fig. 6.3. The value for the ionic strengths of the pure NP suspensions I_0 without added salt are calculated via eqn. 6.5.

the added salt I_{NaCl} under the assumption of full dissociation.

$$I = I_0 + I_{\mathrm{NaCl}} \tag{6.6}$$

6.3.2 Forces across nanoparticle suspensions with added salt

In order to highlight different characteristics of the interaction forces, two representations (semilogarithmic and linear) for the same force profiles are chosen in this section. First, a semilogarithmic representation is preferred to analyse the double layer contribution. The second part focuses on the structural force, and, therefore, a linear representation is selected.

Double layer force Semilogarithmic representations of the absolute values of interaction forces between charged silica surfaces in aqueous suspensions containing like-charged silica NPs and salt are given in Fig. 6.4. The complete measured force up to the constant compliance region is visualised. This representation emphasises the behaviour of the double layer force as well as its transition region towards the structural force.

The determination of the ionic strength in section 6.3.1 allows the Debye screening length κ^{-1} to be calculated independently which is then put as a fixed parameter into the fit procedure. Double layer forces are fitted to eqn. 6.2 by adjusting the diffuse layer potential ψ_{dl}.

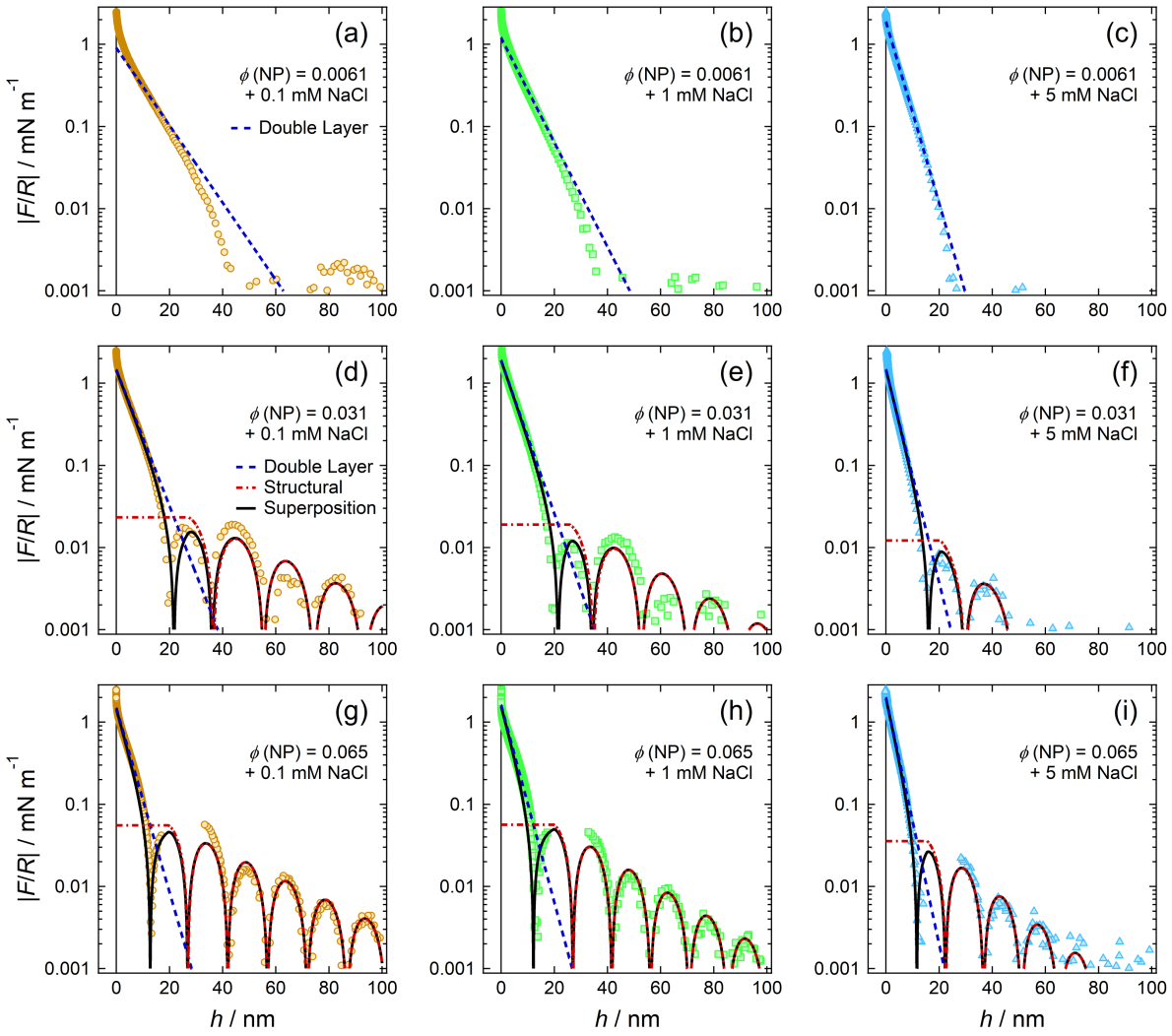

Figure 6.4: Absolute values of the interaction forces between charged silica surfaces in aqueous suspensions containing likely charged silica NPs and salt at different concentrations. Experimental data (coloured dots) are modelled with a superposition (black, solid line) of double layer (blue, dashed line) and structural forces (red, dashed line). No structural forces could be fitted for the smallest volume concentration of silica NPs ($\phi = 0.0061$). Double layer forces are fitted to eqn. 6.2 by adjusting ψ_{dl} as the only fit parameter.

Fig. 6.4 (a-c) shows the force profiles with NP volume fractions of $\phi = 0.0061$. The force profile at 0.1 mM NaCl exhibits a deviation from the ideal, exponential decay, as known for pure NaCl solutions (see Fig. 6.10, Appendix). Upon further addition of NaCl this deviation decreases, until at 5 mM NaCl the interaction profile is well described by the exponential double layer force. Generally, the Debye screening length κ^{-1} decreases with increasing salt concentration, resulting in shorter ranged double layer forces at higher concentrations of NaCl.

Interaction profiles with NP volume fractions of $\phi = 0.031$ are shown in Fig. 6.4 (d-f). Higher amounts of NPs involve increased amounts of counterions which result in a stronger Debye screening of the surface potential compared to smaller volume fractions of NPs. The Debye screening length of the double layer force decreases further upon addition of NaCl. Superposition of the double layer and structural forces results in a good description of the experimental data even in the transition region of both force contributions, *i.e.* the region where both, the double layer and the structural force contribute considerably to the total interaction force.

Fig. 6.4 (g-i) shows the interaction profiles at NP volume fractions of $\phi = 0.065$. The same trends in the double layer force are observed as compared to the ones with smaller NP volume fractions. The decay in the double layer forces are well described with the independently calculated ionic strength.

The total ionic strength I is calculated according to eqn. 6.6, as the sum of the ionic strength of the pure NP suspension and the ionic strength of the added salt. The diffuse layer potential ψ_{dl} is fitted to the data according to eqn. 6.2. Absolute values of the diffuse layer potential of the confining surfaces typically decreases with ionic strength in pure electrolyte solutions (data in Fig. 6.10, Appendix). When NP are in solution, however, the diffuse layer potentials appear rather constant with a mean value of $\psi_{\mathrm{dl}} = -28.6 \pm 2.9$ mV, irrespective of the concentration of NPs and salt in the system (Fig. 6.5 (a)). It remains unclear if the addition of NPs constrain the diffuse layer potential to a constant value or if it will change at different ionic strengths, since only a small interval of the ionic strength can be investigated.

Surface charge densities σ_{dl} at the origin of the diffuse layer of the confining surfaces were calculated via the Grahame equation (eqn. 2.28 in chapter 2). Resulting values can be seen in Fig. 6.5 (b). The absolute value of the surface charge density is found to

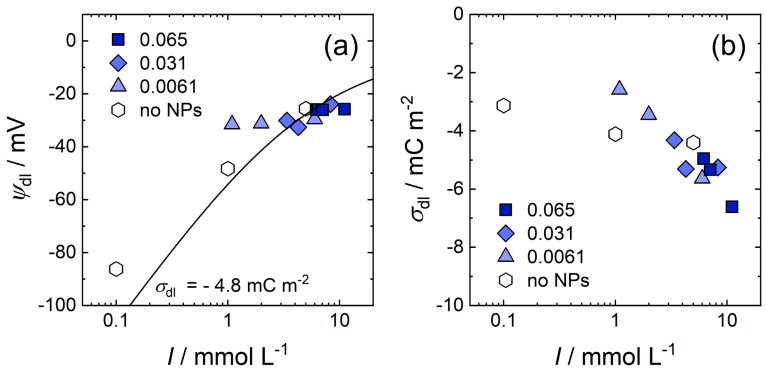

Figure 6.5: Surface characteristics at different volume fractions of NPs and upon addition of NaCl. The total ionic strength I is calculated as the sum of the ionic strengths of the pure NP suspension and added NaCl, $I = I_0 + I_{\mathrm{NaCl}}$. (a) The fitted diffuse layer potential ψ_{dl}, and (b) the surface charge density at the origin of the diffuse layer σ_{dl} as calculated from the Grahame equation (eqn. 2.28).

increase with ionic strength. This behaviour was found before in pure electrolyte solutions [35] and was attributed to *e.g.* higher degree of ionisation of surface groups, or dissociation of adsorbed water molecules. The mean value of the surface charge density in presence of NP suspensions is $\sigma_{\mathrm{dl}} = -4.8 \pm 1.1\,\mathrm{mC\,m^{-2}}$. This is in good agreement with literature values [81, 195]. Under the assumption of this constant surface charge density, the general trend in the diffuse layer potential could be outlined, as visualised by the solid line in Fig. 6.5 (a).

Structural forces The interaction force profiles in linear representation are shown in Fig. 6.6. A smaller force range is chosen for a better resolution of the structural force.

Fig. 6.6 (a-c) shows the force profiles at NP volume fractions of $\phi = 0.0061$. At this concentration, the force profiles are almost completely determined by the double layer force. At 0.1 mM added NaCl, a small contribution of the structural force can be observed. It is, however, too small to be reasonably described by a sufficient fit model in order to extract further information. Upon further addition of NaCl, the total ionic strength - from the NP's counterions and added salt - increases almost by a factor of six from (a) to (c). As a result, the structural force weakens, until at 5 mM NaCl no

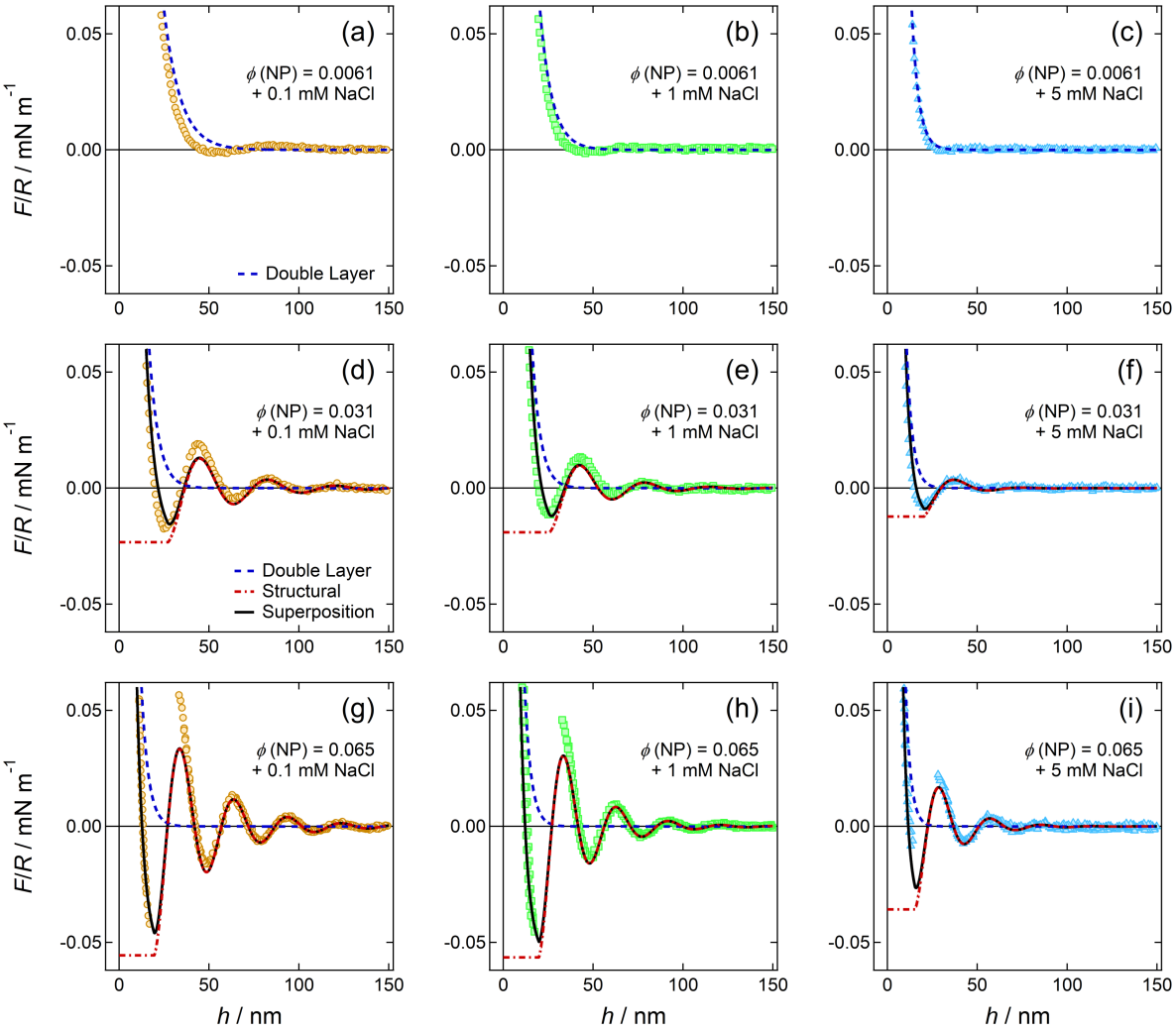

Figure 6.6: Interaction forces between charged silica surfaces in aqueous suspensions containing silica NPs and salt at different concentrations, *i.e.* the same force data as in Fig. 6.4. Linear representation increases the resolution of the structural force. Experimental data (coloured dots) is modelled with a superposition (black solid line) of double layer (blue, dashed line) and structural force (red, dashed line). No structural forces could be fitted for the smallest volume concentration of silica NPs ($\phi = 0.0061$).

structural force is observed and the interaction profile is well described by the double layer force only.

Interaction profiles at NP volume fractions of $\phi = 0.031$ are displayed in Fig. 6.6 (d-f). With increased NP volume fraction, structural forces are more pronounced and fitting is possible using eqn. 6.4 for all salt concentrations investigated. Three pronounced oscillations are observed in the structural force in the system with a low amount of added salt. With increasing salt concentration, the structural force contribution decreases, so that upon addition of 5 mM only one clear oscillation remains observable. At the same time, the magnitude of the depletion attraction, *i.e.* the force at surface separation below the first minimum in the force profile, decreases with increasing ionic strength in the systems.

Interaction profiles in suspensions of NP volume fractions of $\phi = 0.065$ are shown in Fig. 6.6 (g-i). The structural force is most pronounced at the highest NP volume fraction. With more pronounced oscillations in the force profile, the gradient of the force exceeds the cantilevers spring constant between the first minimum and first maximum. As a result, the full force profiles cannot be resolved and a jump-in (at approach) or jump-out (when retract) to the next stable force branch occurs between the first minimum and first maximum in the force profile. At least five force oscillations up to surface separations of more than 150 nm are observed at low salt concentrations. Fitting of the structural force using eqn. 6.4 systematically shows and underestimation of the first maximum in the force profile, which is most pronounced at highest volume fractions of silica and lowest salt concentration, *i.e.* at most pronounced force oscillations.

The fit parameters for the structural forces are given in Fig. 6.7. The amplitude A is known to increase with higher volume fractions of silica [87]. This finding can be confirmed in this study. No distinct change in amplitude is obtained upon addition of monovalent salt. The wavelength λ is calculated via the inverse cubic root scaling law: $\lambda = 1.612(0.5\,d)\phi^{-1/3}$ (see eqn. 4.3 in chapter 4) and is independent of the ionic strength in the suspension [196]. The diameter of the particles was taken from chapter 4 as 15.8 nm. The results are displayed in Fig. 6.7 (b). Fitted values are a few percent below the predicted values but are well within the uncertainty of the determination method. The offset h' generally decreases with increasing ionic strength in suspension. A scaling exponent m = - 0.45 $\pm$ 0.07 for $h' \propto I^{\mathrm{m}}$ could be extracted and will be further considered in the discussion section. The decay length ξ decreases with inceasing ionic

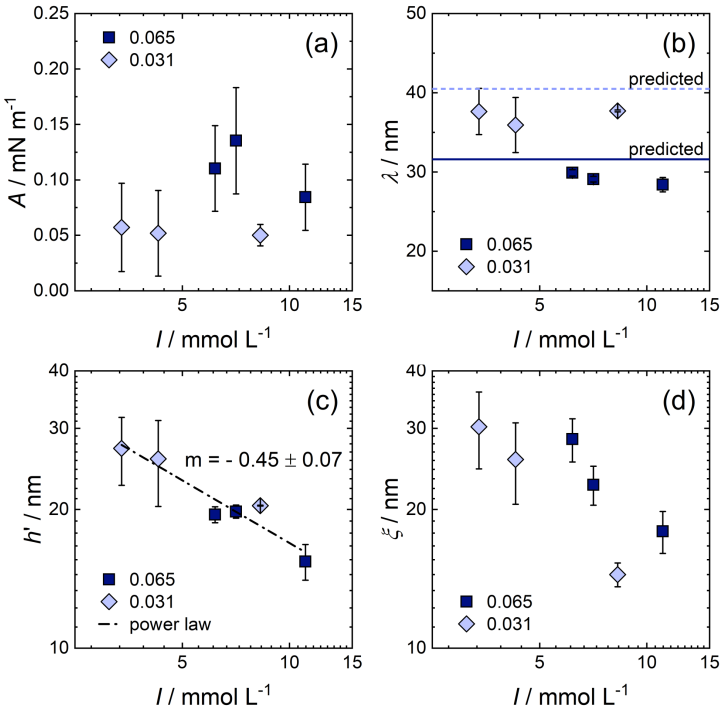

Figure 6.7: Fit parameters of the structural force at different volume fractions of NPs and upon addition of NaCl. Total ionic strength is calculated as the sum of added NaCl and the ionic strength of the pure NP suspension. Parameters describing the structural forces are (a) amplitude A, (b) wavelength λ, (c) offset h' and (d) the decay length ξ. In (b), the wavelength λ can also be predicted using the inverse cubic root scaling law $\lambda = 1.612(0.5\,d)\phi^{-1/3}$ (dashed line: $\phi = 0.031$, solid line: $\phi = 0.065$). Fitting was performed in (c) to extract a scaling exponent m for $h' \propto I^{\mathrm{m}}$.

strength. A higher volume fraction and, consequently, a tighter packing of the particles increases the decay length. This in good agreement with simulations [63].

Superposition of double layer and structural force The complete force profile can be divided into different parts, according to the prevalent force contributions. At small surface separations, the interaction force is determined by the strength of the double layer force with its typical exponential decay. The interaction force at larger surface separations, however, is purely determined by the structural force, since it is typically longer-ranged than the double layer force.

In between these parts a transition region is observed, where both, the double layer and the structural force contribute considerably to the total interaction force. Some features may seem surprising when looking at it from a perspective of a single force contribution. On the one hand, deviations from an exponential decay at smaller surface separation are observed once the structural force gains influence compared to the double layer force. While on the other hand, the oscillations in the force profile are asymmetric to the zero-force line in the region where still a considerable strength of the double layer force is present. Those features are no properties of the force contributions itself but originate from the superposition of both forces.

6.4 Discussion

6.4.1 Model of the double layer force using jellium approximation

The challenge of describing the screening behaviour of suspensions containing charged nanoparticles (NPs) and salt is that the system represents a strongly asymmetric electrolyte of small monovalent ions and large multivalent particles (macroions). Different approaches to this problem have already been published. Danov *et al.* compared the applicability of the Poisson-Boltzmann model (PB) with the jellium approximation (JA) for the description of the screening behaviour in dispersions containing ionic micelles [142]. For the general discussion here, the framework of colloidal dispersions containing macroions and added salt is used.

In the PB model, all charge carriers in the dispersion (monovalent ions and multivalent macroions) obtain Boltzmann distribution as a response to the surfaces electric field. As a result, both the multivalent macroions and the monovalent ions contribute to the Debye screening. The valence per particles z_i can be very large, resulting in a very strong Debye screening when applying eqn. 6.5.

Moazzami-Gudarzi *et al.* described the interaction profile in dispersions containing strong, negatively charged polyelectrolytes (macroions) and added monovalent salt with a superposition of double layer and structural forces [81, 189]. A numerical solution of the PB model was chosen for the description of the double layer interaction. Two distinct regions are defined: (i) At small surface separations, the polyelectrolytes are

too large to enter the vicinity between the surfaces and Debye screening is only transacted through the monovalent ions in the dispersion. (ii) Once the surface separation is large enough that the macroions can enter the vicinity between the confining surfaces, they also contribute to Debye screening and the double layer force typically vanishes within a few nanometer. The non-exponential decay in the force profile was described as the non-exponential double layer force. The effective charge per macroion enters the fit of the double layer force as a free parameter. Using this description, almost no transition region between the double layer force and structural force dominated regions exist.

In the PB model, monovalent ions and multivalent macroions are treated as point-like ions. In reality, the macroions themselves have a considerable volume. Moreover, the repulsive interactions between the macroions hinder them from a Boltzmann distribution. Danov *et al.* concluded, that the JA offers an improved description of the screening behaviour compared to the PB model. In this approximation, the macroions obtain a uniform distribution and the macroions are excluded from Debye screening. Only the co- and counterions of low valency contribute to it. JA was already used - without specifically calling it JA - to calculate the interparticle interactions in dispersions containing polyelectrolytes [74] and nanoparticles [197], yet without description of the interaction of the confining surfaces.

The non-exponential decay of the total interaction force in this study (see Fig. 6.4) is caused by the superposition of the exponentially decaying double layer force and the structural forces. When the macroions are excluded from Debye screening, the double layer force offers reasonable results with a reduction of fit parameters based on an independent determination of the ionic strength of the dispersion. This result offers an easy description of the double layer force when its superposed with structural forces, together with the interesting finding that the macroions themselves *do not* contribute to Debye screening. However, macroions do contain a considerable amount of counterions (in this study up to a concentration of a few millimolar), which *do* contribute to Debye screening. It is, therefore, irrelevant for the double layer force if the macroions are present in confinement.

6.4.2 Model of the structural force introducing a particle-free layer

Maroni *et al.* recently studied the structuring of the same type of silica NP suspensions (Ludox HS) near the suspension-silica interface, using specular neutron reflectivity [198]. The concentration profile of the NPs perpendicular to the interface is characterised by a damped oscillatory profile, indicating a layering of the particles next to a wall. In order to correctly fit the reflection curves, a particle free layer next to the interface was defined. The thickness of this particle free layer d depends on the volume fraction of the dispersed silica particles ϕ with a scaling law of roughly $d \propto \phi^{-1/2}$. The authors concluded that the dependency originated from the electrostatic repulsion of the NPs from the charged surface.

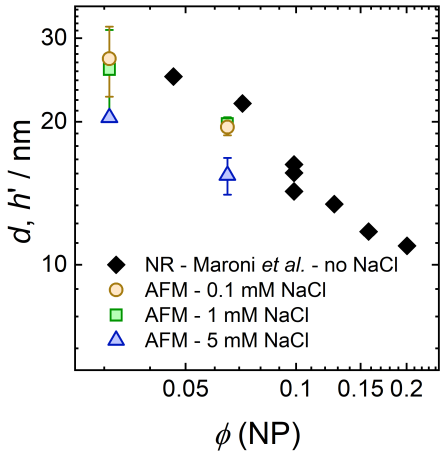

Figure 6.8: Comparison of the thickness d of particle free layers next to a single silica-liquid interface as probed by specular neutron reflectivity from Maroni *et al.* [198] (black dots, without NaCl) with the offset h' extracted from fitting the structural force (coloured dots, at various salt concentrations). Values are presented as a function of the volume fraction ϕ of NPs in suspension.

The oscillatory structural force is the direct result of overlapping concentration profiles, when two surfaces are brought into close contact. Therefore, a particle free layer at one surface should be directly related to an offset in the oscillatory structural force between two surfaces, as described in this study.

Fig. 6.8 shows the comparison of the particle free layer thickness d (from neutron reflectivity data) with the offset h' extracted from the position of the first minimum of force

measurements. Both experiments are in good agreement with each other. With increasing amount of added salt, the electrostatic screening increases due to an increased ionic strength. This results in a decrease in the thickness of the particle free layer and, therefore, also in the offset (see also Fig. 6.7 (c)). The scaling exponent m = - 0.45 $\pm$ 0.07 for $h' \propto I^{m}$ confirms the finding of Maroni *et al.* for the offset being of electrostatic origin. A scaling exponent of - 0.5 is rationalized by the Debye screening length, which increases with the inverse of the square root of the ionic strength. The offset can also be compressed by addition of salt at a constant volume fraction of NPs. This further indicates that the offset is rather dominated by the electrostatic interactions between the particles and the surfaces, than by packing effects of the particles in the fluid.

The determination of a particle free layer next to the surface also affirms the introduction of the depletion attraction once the surface separation is smaller than the offset, since all particles are considered depleted from the vicinity of the confining surfaces.

6.4.3 Deviation between fit and data

With increasing NP concentration and decreasing ionic strength, deviations of the fit and the experimental data increase. The deviation is, therefore, most pronounced in Fig. 6.6 (g). An underestimation of the data by the fit often occurs at the last layer of NPs, especially, when they are well ordered, *i.e.* at high concentration and high repulsion between the NPs. Similar underestimations have also been reported for highly compressed ionic liquids [199].

Although an extended fitting formula that accounts for an additional repulsive contribution in the oscillatory structural force was presented recently [88, 200], it is excluded for this analysis in order to keep the fit model as simple as possible. The underestimation of the first maximum is considered as the breakdown of the asymptotic behaviour, predicted by density functional theory (DFT) for large distances [150]. This deviation cannot be explained by purely electrostatic reasons and might be seen as an confinement effect itself, which has to be further clarified. A possible explanation may include slower dynamics of NPs when they are strongly confined.

6.5 Conclusion

Interaction forces between negatively charged surfaces across suspensions containing nanoparticles and monovalent salt are successfully measured using colloidal-probe atomic force microscopy. Full description of the force profiles is achieved by the superposition of double layer and structural forces with no mutual effect between the two types of forces. The Debye screening length of the suspensions are independently calculated from results of conductivity measurements. This was previously a major obstacle for the correct description of the double layer force. Like this, both force contributions are untangled. Following conclusions are made:

The charged nanoparticles show a preferred self-organised structure which can be described by the jellium approximation. Next to a surface, they form a layer-like arrangement which can be detected as oscillatory structural force. The particles are depleted from the region next to a confining surface. The thickness of this depletion zone is dominated by the electrostatic repulsion of the particles from the likely charged surface rather than by particle concentration, *i.e.* packing effects. This picture is in good agreement with a particle-free layer next to a single surface as probed by neutron reflectivity measurements. Unlike the nanoparticles, the monovalent ions (the particles counterions and added salt ions) follow Boltzmann distribution.

It has to be emphasised that the total force profile can be simply divided into a pure double layer force and a pure structural force contribution. The decay of the double layer force is only determined by the Boltzmann distributed monovalent ions while the structural force originates simply from the layer-like arrangement of the particles. This means that the different distributions of particles and ions do not affect each other. Deviations from an exponential decay at small separations, as already reported in literature, are simply caused by the superposition of a double layer and the structural force. The same superposition leads to asymmetry of the force oscillation.

The study contributes to a better understanding of surface interactions across different kinds of concentrated colloidal dispersions. It explains the superposition of DLVO and structural forces. This model might be extended for the description of other types of confined colloidal dispersions like for instance biomolecules in a physiological solution between biomembranes or complex fluids in wetting films.

6.6 Appendix

Potentiometric titration of nanoparticle suspensions Potentiometric titration curves of pure nanoparticle (NP) suspensions (Ludox HS) at three different volume concentrations of NPs are shown in Fig. 6.9.

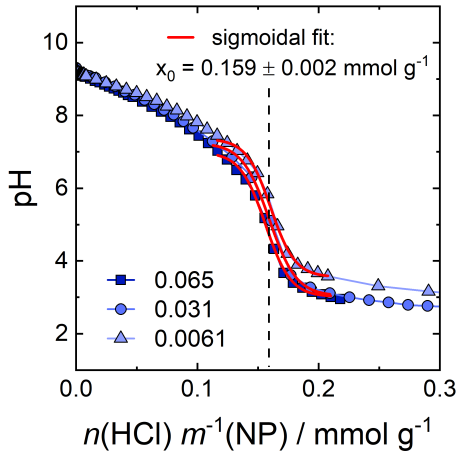

Figure 6.9: Potentiometric titration of pure NP suspensions (without added salt) upon addition of HCl for various volume fractions of NPs. The amount of added HCl is normalised by the total mass of NPs in the suspension. Sigmoidal fitting is used to extract the point of inflection x_0 with the mean value being displayed in the graph.

The surface charge density σ of NPs in pure, aqueous dispersions can be calculated from the point of inflection x_0 in the titration curve ($0.159 \pm 0.002\,\mathrm{mmol\,g^{-1}}$), the density of silica NPs ρ and the mean diameter d of the NPs, assuming spherical particles.

$$\sigma = x_0 N_\mathrm{A} \rho \frac{d}{6} \tag{6.7}$$

Eqn. 6.7 results in a surface charge density $\sigma = 0.50 \pm 0.01\,\mathrm{nm^{-2}} = 0.080 \pm 0.002\,\mathrm{C\,m^{-2}}$, irrespective of the NP concentration. This is in good agreement with literature values [31, 201, 202].

Interaction forces between charged surfaces in pure electrolyte solution Interaction forces of negatively charged silica surfaces in pure NaCl solutions were measured for reference.

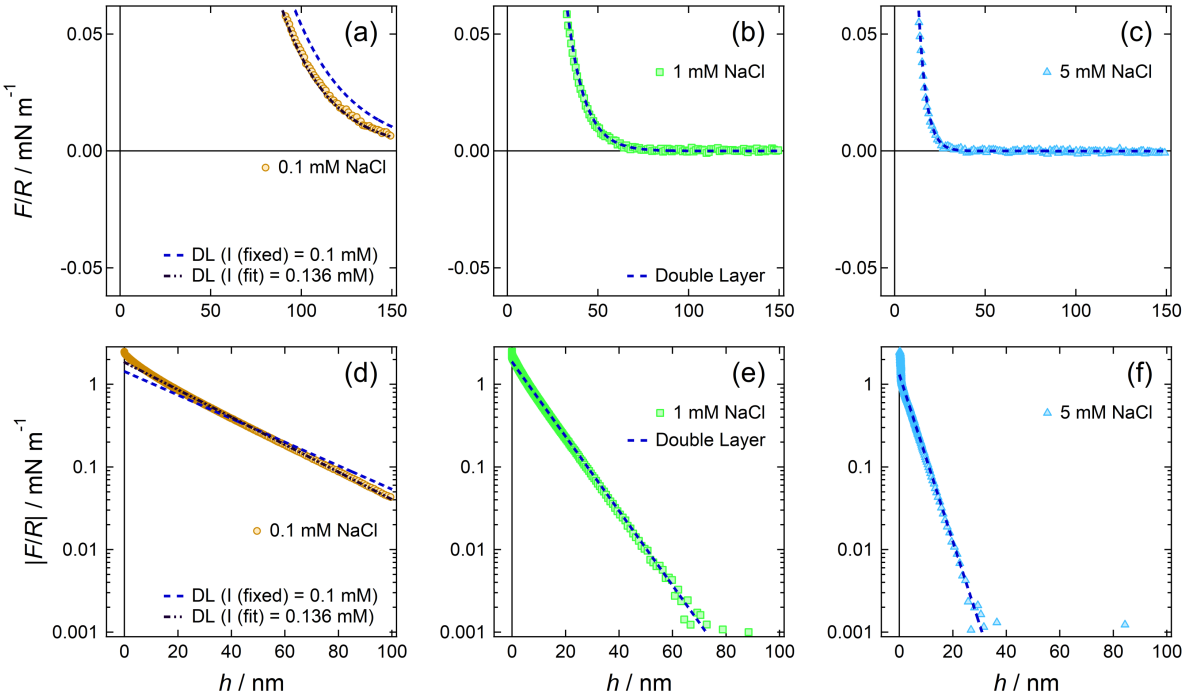

Figure 6.10: Interaction forces between silica surfaces in aqueous NaCl solutions. Experimental data (dots) is compared with the fitted double layer force (dashed line). (a-c): linear representation, (d-f): semilogarithmic representation for emphasis of the double layer force. For 0.1 mM NaCl (a,d) two different fits were performed with either the ionic strength I being fixed or entering as free fit parameter of the double layer force.

Fig. 6.10 shows the measured interaction force profiles in pure NaCl solutions. While (a-c) is in linear representation, (d-f) shows the same data in semilogarithmic representation, for emphasis of the double layer force. The blue dotted lines are the fits to the double layer force, eqn. 6.2, with the diffuse layer potential ψ_{dl} being the only parameter to enter the fitting. Diffuse layer potentials ψ_{dl} are - 86.6 $\pm$ 4.4 mV, - 48.3 $\pm$ 1.5 mV, and - 25.7 $\pm$ 0.9 mV in 0.1 mM, 1 mM, and 5 mM NaCl solutions, respectively. This is in good aggreement with literature values [35]. In Figs. 6.10 (a,d) also a black dotted line is shown, which represents the fit of the double layer force with the ionic strength I also as free fit parameter. Best fit result is obtained for an ionic strength I of 0.136 mM

which shows the difficulty to work at such low ion concentrations, since *e.g.* adsorption of CO_2 may change the ionic strength to this amount.

7 Conclusions and future perspectives

7.1 Conclusions

This thesis presents interaction forces between macroscopic surfaces across colloidal dispersions. Two model systems were chosen as colloidal dispersions: On the one hand, aqueous suspensions of solid silica nanoparticles and on the other hand aqueous dispersions of self-assembled surfactant micelles. Silica nanoparticles feature a stable size and shape under the studied conditions. They can be imaged using electron microscopy and their volume fraction is easily checked by drying a specific volume of the sample. They are, however, limited in concentration up to a volume fraction of approximately 10 vol% are polydisperse, especially when their diameter is small. Moreover, they are intrinsically charged due to the material properties. Self-assembled micelles are colloidal particles that can be concentrated to higher volume fractions. The formation of uncharged particles is also possible by using nonionic surfactants. Due to their self-assembled nature they are considered monodisperse but their size and shape may be very sensitive to solution parameters, such as *e.g.* surfactant and salt concentrations or temperature. Since direct imaging techniques are not easily applicable, their self-assembly was checked by small-angle neutron scattering.

The combination of direct force measurements using colloidal-probe atomic force microscopy, small-angle neutron scattering, and supportive measurements (electron microscopy, zeta-potential measurements, potentiometric titration) offers a wide overview of basically two important features: understanding the bulk properties of the colloidal dispersions and its influence on surface forces. The results reported in the thesis offer new information on following aspects:

Limit of the scaling law for charged particles When surfaces interact across concentrated colloidal dispersion of charged spherical particles, the wavelength λ of the

oscillatory structural force depends on the volume fraction of dispersed particles ϕ as: $\lambda \propto \phi^{-1/3}$. In this approach dispersed nanoparticles are assumed to form a simple cubic packing and the limit of the scaling law was defined at a particle volume fraction of $\phi = 0.52$. This allows the wavelength λ, the particle diameter d and the particle volume fraction ϕ to be connected as: $\lambda = n_p^{-1/3} = 1.612(0.5\,d)\phi^{-1/3}$. This inverse cubic root scaling law allows the determination of single particle properties from force measurements. Nanoparticles of three different sizes were checked by measuring oscillatory structural forces across the nanoparticle suspensions. The extracted wavelengths λ at certain volume fractions ϕ were extrapolated to a volume fraction of $\phi = 0.52$. At this volume fraction, the wavelength λ is expected to coincide with the real particle diameter d according to simple cubic packing. With this method, diameters of the silica nanoparticles are determined as 11.6 ± 0.3 nm, 14.6 ± 0.2 nm, and 24.3 ± 0.4 nm. This is in good agreement with diameters of 10.3 ± 2.0 nm, 15.8 ± 2.9 nm, and 26.1 ± 4.0 nm obtained by transmission electron microscopy. Although this approach shows good results for the determination of the particles diameters, it remains unclear if the simple cubic packing reflects the real packing.

Influence of colloidal surface charge The influence of the colloidal surface charge on the oscillatory structural force is studied using micellar dispersions. Micellar dispersions are used since in suspensions of solid nanoparticles their material properties determine the particles surface charge. Among pure nonionic (*i.e.* uncharged) and pure ionic (*i.e.* charged) micellar dispersions, also dispersions of mixed micelles containing nonionic and anionic surfactant molecules were measured. Mixing nonionic (Tween20) and anionic (SDS) surfactants allowed the formation of micelles with similar shape but variable surface charge. Systematic studies showed that the amplitude A of the oscillatory structural force can be enhanced in two ways: with higher micelle volume fractions but also with higher surface charge per micelle. Moreover, it is observed, that the $\lambda \propto \phi^{-1/3}$ scaling is not a universal scaling behaviour of colloidal particles. The intermicellar distance of uncharged micelles depends only little on the micelles' volume fraction and will even change when the micelles are compressed under geometrical confinement.

Only when the micelles are highly charged, a pronounced structuring occurs. In this case, their interparticle distance is in good agreement the inverse cubic root scaling law. This is observed in the bulk dispersion, but also under geometrical confinement.

The inverse cubic root scaling law can be compared for particle suspensions and micellar dispersion by evaluation of the prefactor f in the inverse cubic root scaling law considering the effective micellar radius r_{eff} as: $\lambda = f r_{\text{eff}} \phi^{-1/3}$. Particles arranging in a simple cubic packing, as proposed for solid nanoparticles, yield a prefactor of $f = 1.612$. The results obtained for charged micelles, however, agree well with a prefactor $f = 1.436$. If there is a fundamental difference in the structuring of both types of colloidal dispersions is still unclear.

Superposition of forces In order to resolve the complete interaction force profile, overlapping force contributions were considered. Interaction forces between negatively charged surfaces across suspensions containing negatively charged nanoparticles and monovalent salt are successfully described by a superposition of double layer and structural forces. No mutual effect between the two types of forces is observed. To model the electrostatic screening behaviour of the concentrated suspensions, best results are observed when the charged nanoparticles are excluded from the electrostatic screening behaviour of the suspension. The nanoparticles cannot respond to the surfaces' electric field due to the strong interparticle interactions. This is taken into account by the so-called jellium approximation. Unlike the nanoparticles, the monovalent ions (the particles counterions and added salt ions) take part in the electrostatic screening of the suspension. Furthermore, the nanoparticles are depleted from the region next to the confining surfaces forming a depletion zone. The onset of the oscillatory structural force has to be shifted by the thickness of the depletion zone. Its thickness is dominated by the electrostatic repulsion of the particles from the likely charged surface rather than by the particle concentration, *i.e.* packing effects.

7.2 Future perspectives

While some questions could be solved in this thesis, other questions remained and in the meantime new ones have arisen which will be addressed in the following:

In the past 40 years, several techniques for direct measurements of surface forces were developed, as listed in chapter 2. Most techniques are nowadays well established, yet some differences in these techniques are still not completely understood. Most likely,

different research groups use one type of technique, *i.e.* CP-AFM throughout this thesis. Only a few studies compare different techniques, as for example the direct comparison of force measurements using AFM and total internal reflection microscopy (TIRM) [203]. When comparing the two most established techniques these days, AFM and SFA, differences become obvious considering the ability to measure oscillatory forces. Interestingly, both techniques are able to measure the complete variety of oscillatory forces in (pseudo) one-component systems, however, for two-component systems, the only SFA measurement showing oscillatory forces was across highly concentrated CTAB micellar dispersions [66]. Neither in nanoparticle suspensions nor in polyelectrolyte solutions oscillatory forces were detectable with a SFA. A reason for this may be that in a SFA measurement only a small area of a complete sphere (with the radius of curvature) is immersed in liquid. To resolve these apparent contradictions, further investigations of the differences of SFA and AFM measurements, especially when measuring depletion forces, would be highly desirable.

The validity of the jellium approximation in chapter 6 reveal the screening behaviour of concentrated nanoparticle suspensions. The interparticle repulsion hinders the particles from responding to an electric field, while monovalent ions in the system remain unhindered. It would be interesting to find out up to which size and interaction charged particles can be considered as macroions, *i.e.* taking part in the screening of surface charges according to the Poisson-Boltzmann framework. This issue may be closely related to the recent discovery of "underscreening" (*i.e.* unexpectedly long Debye screening lengths) in highly concentrated electrolytes solutions or ionic liquids [57, 204–206]. It was shown that at high ion concentrations the mean ion-ion distance may become smaller than the Bjerrum length - a measure at which distance the electrostatic interaction is compensated by thermal energy. In such a regime the ion-ion interactions reduce the ions ability to sufficiently respond to an electric field and an "underscreening" of the liquid is observed.

Deviation between measured oscillatory structural forces and the fit to a simple decaying oscillatory function is briefly discussed in section 6.4.3. Although, in this case, the double layer contribution was subtracted, deviations between data and fit are still observed in the first oscillation of the force profile with its physical origin remaining unclear. To further evaluate this phenomenon, future experiments may be carried out using following approaches:

1. Force measurements at different potentials of the confining surfaces. This can be

achieved in AFM measurements using an electrochemical cell, where typically a conducting, flat substrate is connected as working electrode to a potentiostat [207–210]. In more sophisticated measurements, both the substrate and cantilever may be connected as working electrodes using a bi-potentiostat, allowing the potential of both confining surfaces to be adjusted.

2. Dynamic force measurements may be used to extract the dissipation of confined complex liquids. This was already demonstrated for confined ionic liquids by de Beer *et al.* [211, 212]. In those experiments, the cantilever is excited, typically to its resonance frequency at small amplitudes. Simultaneously, the amplitude and phase is measured during probe-substrate approach. With this information, an interaction stiffness and dissipation can be calculated using a harmonic oscillator model. First promising experiments have been carried out across concentrated nanoparticle suspensions. A major obstacle remains the correct determination of the resonance frequency of soft cantilevers in liquid. This is still to be optimised and discussed in order to extract correct results.

The results presented throughout this thesis might further contribute to the broad field of colloidal science. The fundamental understanding of surface forces across concentrated colloidal dispersions is not restricted to the model systems from this work, *i.e.* nanoparticle suspensions and micellar dispersions, but may be transferred to other types of colloidal systems. Interesting applications in life sciences and engineering often comprise geometrically confined colloidal dispersions, such as *e.g.* interacting biomembranes or blood vessels, lab-on-a-chip applications, or different surface wetting phenomena.

Bibliography

[1] Fåhraeus, R. *Physiological Reviews* **1929**, *9*, 241–274.

[2] Tanford, C. *Science (New York, N.Y.)* **1978**, *200*, 1012–1018.

[3] Marenduzzo, D.; Finan, K.; Cook, P. R. *The Journal of cell biology* **2006**, *175*, 681–686.

[4] Briscoe, W. H. *Current Opinion in Colloid & Interface Science* **2015**, *20*, 46–53.

[5] Fleischmann, D.; Maslanka Figueroa, S.; Beck, S.; Abstiens, K.; Witzgall, R.; Schweda, F.; Tauber, P.; Goepferich, A. *ACS applied materials & interfaces* **2020**, *12*, 34689–34702.

[6] Elbourne, A.; Crawford, R. J.; Ivanova, E. P. *Journal of colloid and interface science* **2017**, *508*, 603–616.

[7] Trokhymchuk, A.; Henderson, D. *Current Opinion in Colloid & Interface Science* **2015**, *20*, 32–38.

[8] van Roij, R.; Dijkstra, M.; Hansen, J.-P. *Physical Review E* **1999**, *59*, 2010–2025.

[9] Dijkstra, M.; van Roij, R.; Evans, R. *The Journal of chemical physics* **2000**, *113*, 4799–4807.

[10] Luckham, P. F.; Ansarifar, M. A.; de L. Costello, B. A.; Tadros, T. *Powder Technology* **1991**, *65*, 371–379.

[11] Hunter, R. J. *Foundations of colloid science*, 2nd ed.; Oxford Univ. Press: Oxford, 2001.

[12] Butt, H.-J.; Kappl, M. *Surface and Interfacial Forces*, 2nd ed.; Wiley-VCH: Weinheim, 2018.

[13] Evans, D. F.; Wennerström, H. *The colloidal domain: Where physics, chemistry, biology, and technology meet*, 2nd ed.; Wiley-VCH: New York, NY, 1999.

[14] Israelachvili, J. N.; Mitchell, D. J.; Ninham, B. W. *Journal of the Chemical Society, Faraday Transactions 2* **1976**, *72*, 1525.

[15] Barrat, J.-L.; Hansen, J.-P. *Basic concepts for simple and complex liquids*; Cambridge University Press: Cambridge, 2003.

[16] Hansen, J.-P.; McDonald, I. R. *Theory of simple liquids*, 3rd ed.; Elsevier/Academic Press: Amsterdam, 2008.

[17] Percus, J. K.; Yevick, G. J. *Physical Review* **1958**, *110*, 1–13.

[18] Hayter, J. B.; Penfold, J. *Molecular Physics* **1981**, *42*, 109–118.

[19] Yarnell, J. L.; Katz, M. J.; Wenzel, R. G.; Koenig, S. H. *Physical Review A* **1973**, *7*, 2130–2144.

[20] Derjaguin, B. *Kolloid-Zeitschrift* **1934**, *69*, 155–164.

[21] Derjaguin, B.; Landau, L. *Acta Physico Chemica URSS* **1941**, *14*, 30–59.

[22] Verwey, E. J. W. *The Journal of physical and colloid chemistry* **1947**, *51*, 631–636.

[23] Hamaker, H. C. *Physica* **1937**, *4*, 1058–1072.

[24] Dzyaloshinskii, I. E.; Lifshitz, E. M.; Pitaevskii, L. P. *Soviet Physics Uspekhi* **1961**, *4*, 153–176.

[25] Tabor, R. F.; Manica, R.; Chan, D. Y. C.; Grieser, F.; Dagastine, R. R. *Physical review letters* **2011**, *106*, 064501.

[26] Helmholtz, H. *Annalen der Physik und Chemie* **1853**, *165*, 211–233.

[27] Gouy, M. *Journal de Physique Théorique et Appliquée* **1910**, *9*, 457–468.

[28] Chapman, D. L. *The London, Edinburgh, and Dublin Philosophical Magazine and Journal of Science* **1913**, *25*, 475–481.

[29] Stern, O. *Zeitschrift für Elektrochemie* **1924**, *30*, 508–516.

[30] Russel, W. B.; Saville, D. A.; Schowalter, W. R. *Colloidal dispersions*; Cambridge University Press: Cambridge, 1989.

[31] Brown, M. A.; Goel, A.; Abbas, Z. *Angewandte Chemie (International ed. in English)* **2016**, *55*, 3790–3794.

[32] Stierstadt, K. *Thermodynamik: Von der Mikrophysik zur Makrophysik*; Springer: Berlin, Heidelberg, 2010.

[33] Israelachvili, J. N. *Intermolecular and surface forces*, 3rd ed.; Academic Press: Burlington, MA, 2011.

[34] Danov, K.; Basheva, E.; Kralchevsky, P. *Materials* **2016**, *9*, 145.

[35] Smith, A. M.; Maroni, P.; Trefalt, G.; Borkovec, M. *The journal of physical chemistry. B* **2019**, *123*, 1733–1740.

[36] Carnie, S. L.; Chan, D. Y. *Journal of colloid and interface science* **1993**, *161*, 260–264.

[37] Zhao, C.; Ebeling, D.; Siretanu, I.; van den Ende, D.; Mugele, F. *Nanoscale* **2015**, *7*, 16298–16311.

[38] Trefalt, G.; Behrens, S. H.; Borkovec, M. *Langmuir* **2016**, *32*, 380–400.

[39] Ludwig, M.; von Klitzing, R. *Current Opinion in Colloid & Interface Science* **2020**, *47*, 137–152.

[40] Horn, R. G.; Israelachvili, J. N. *The Journal of chemical physics* **1981**, *75*, 1400–1411.

[41] O'Shea, S. J.; Welland, M. E.; Rayment, T. *Applied Physics Letters* **1992**, *60*, 2356–2358.

[42] Liu, F.; de Beer, S.; van den Ende, D.; Mugele, F. *Physical review. E* **2013**, *87*, 062406.

[43] Christenson, H. K. *The Journal of chemical physics* **1983**, *78*, 6906–6913.

[44] Chan, D. Y. C.; Horn, R. G. *The Journal of chemical physics* **1985**, *83*, 5311–5324.

[45] Christenson, H. K.; Gruen, D. W. R.; Horn, R. G.; Israelachvili, J. N. *The Journal of chemical physics* **1987**, *87*, 1834–1841.

[46] Li, T.-D.; Gao, J.; Szoszkiewicz, R.; Landman, U.; Riedo, E. *Physical Review B* **2007**, *75*, 6996.

[47] Li, T.-D.; Riedo, E. *Physical Review Letters* **2008**, *100*, 106102.

[48] Nakada, T.; Miyashita, S.; Sazaki, G.; Komatsu, H.; Chernov, A. *Jpn. J. Appl. Phys.* **1996**, *35*, 52–55.

[49] Franz, V.; Butt, H.-J. *The Journal of Physical Chemistry B* **2002**, *106*, 1703–1708.

[50] Carbone, G.; Barberi, R.; Musevic, I.; Krzic, U. *Physical review. E* **2005**, *71*, 051704.

[51] de Gennes, P. G. *Langmuir* **1990**, *6*, 1448–1450.

[52] Petrov, P.; Olsson, U.; Christenson, H.; Miklavic, S.; Wennerstroem, H. *Langmuir* **1994**, *10*, 988–990.

[53] Petrov, P.; Miklavcic, S.; Olsson, U.; Wennerstroem, H. *Langmuir* **1995**, *11*, 3928–3936.

[54] Petrov, P.; Olsson, U.; Wennerstroem, H. *Langmuir* **1997**, *13*, 3331–3337.

[55] Wydro, M. J.; Warr, G. G.; Atkin, R. *Langmuir* **2015**, *31*, 5513–5520.

[56] Hayes, R.; Borisenko, N.; Tam, M. K.; Howlett, P. C.; Endres, F.; Atkin, R. *The Journal of Physical Chemistry C* **2011**, *115*, 6855–6863.

[57] Gebbie, M. A.; Smith, A. M.; Dobbs, H. A.; Lee, A. A.; Warr, G. G.; Banquy, X.; Valtiner, M.; Rutland, M. W.; Israelachvili, J. N.; Perkin, S.; Atkin, R. *Chemical communications* **2017**, *53*, 1214–1224.

[58] Rodenbücher, C.; Wippermann, K.; Korte, C. *Applied Sciences* **2019**, *9*, 2207.

[59] Asakura, S.; Oosawa, F. *The Journal of chemical physics* **1954**, *22*, 1255–1256.

[60] Lekkerkerker, H. N. W.; Tuinier, R. *Colloids and the depletion interaction*; Springer: Dordrecht, 2011; Vol. 833.

[61] Kralchevsky, P. A.; Danov, K. D.; Anachkov, S. E. *Current Opinion in Colloid & Interface Science* **2015**, *20*, 11–18.

[62] Klapp, S. H. L.; Qu, D.; Klitzing, R. V. *The journal of physical chemistry. B* **2007**, *111*, 1296–1303.

[63] Klapp, S. H. L.; Grandner, S.; Zeng, Y.; von Klitzing, R. *Journal of Physics: Condensed Matter* **2008**, *20*, 494232.

[64] Nikolov, A.; Wasan, D. *Journal of colloid and interface science* **1989**, *133*, 1–12.

[65] Bergeron, V.; Radke, C. J. *Langmuir* **1992**, *8*, 3020–3026.

[66] Richetti, P.; Kékicheff, P. *Physical Review Letters* **1992**, *68*, 1951–1955.

[67] McNamee, C. E.; Tsujii, Y.; Ohshima, H.; Matsumoto, M. *Langmuir* **2004**, *20*, 1953–1962.

[68] Tulpar, A.; van Tassel, P. R.; Walz, J. Y. *Langmuir* **2006**, *22*, 2876–2883.

[69] Tabor, R. F.; Chan, D. Y. C.; Grieser, F.; Dagastine, R. R. *The Journal of Physical Chemistry Letters* **2011**, *2*, 434–437.

[70] Tabor, R. F.; Lockie, H.; Chan, D. Y. C.; Grieser, F.; Grillo, I.; Mutch, K. J.; Dagastine, R. R. *Soft Matter* **2011**, *7*, 11334.

[71] James, G. K.; Walz, J. Y. *Colloids and Surfaces A: Physicochemical and Engineering Aspects* **2014**, *441*, 406–419.

[72] Milling, A. J. *The Journal of Physical Chemistry* **1996**, *100*, 8986–8993.

[73] Milling, A. J.; Vincent, B. *Journal of the Chemical Society, Faraday Transactions* **1997**, *93*, 3179–3183.

[74] Klitzing, R.; Espert, A.; Asnacios, A.; Hellweg, T.; Colin, A.; Langevin, D. *Colloids and Surfaces A: Physicochemical and Engineering Aspects* **1999**, *149*, 131–140.

[75] Biggs, S.; Dagastine, R. R.; Prieve, D. C. *The Journal of Physical Chemistry B* **2002**, *106*, 11557–11564.

[76] Qu, D.; Pedersen, J. S.; Garnier, S.; Laschewsky, A.; Möhwald, H.; von Klitzing, R. *Macromolecules* **2006**, *39*, 7364–7371.

[77] Qu, D.; Brotons, G.; Bosio, V.; Fery, A.; Salditt, T.; Langevin, D.; von Klitzing, R. *Colloids and Surfaces A* **2007**, *303*, 97–109.

[78] Biggs, S. *Physical Chemistry Chemical Physics* **2010**, *12*, 4172–4177.

[79] Üzüm, C.; Christau, S.; von Klitzing, R. *Macromolecules* **2011**, *44*, 7782–7791.

[80] Browne, C.; Tabor, R. F.; Grieser, F.; Dagastine, R. R. *Journal of colloid and interface science* **2015**, *451*, 69–77.

[81] Moazzami-Gudarzi, M.; Maroni, P.; Borkovec, M.; Trefalt, G. *Soft Matter* **2017**, *13*, 3284–3295.

[82] Kubiak, K.; Maroni, P.; Trefalt, G.; Borkovec, M. *Soft Matter* **2020**, *31*, 7378.

[83] Piech, M.; Walz, J. Y. *Journal of colloid and interface science* **2002**, *253*, 117–129.

[84] Piech, M.; Walz, J. Y. *The Journal of Physical Chemistry B* **2004**, *108*, 9177–9188.

[85] Drelich, J.; Long, J.; Xu, Z.; Masliyah, J.; Nalaskowski, J.; Beauchamp, R.; Liu, Y. *Journal of colloid and interface science* **2006**, *301*, 511–522.

[86] Tulpar, A.; Walz, J. Y. *Colloids and Surfaces A* **2007**, *300*, 268–280.

[87] Zeng, Y.; Grandner, S.; Oliveira, C. L. P.; Thünemann, A. F.; Paris, O.; Pedersen, J. S.; Klapp, S. H. L.; von Klitzing, R. *Soft Matter* **2011**, *7*, 10899.

[88] Schön, S.; von Klitzing, R. *Beilstein journal of nanotechnology* **2018**, *9*, 1095–1107.

[89] Scarratt, L. R. J.; Kubiak, K.; Maroni, P.; Trefalt, G.; Borkovec, M. *Langmuir* **2020**, *36*, 14443–14452.

[90] Basheva, E. S.; Kralchevsky, P. A.; Danov, K. D.; Ananthapadmanabhan, K. P.; Lips, A. *Physical Chemistry Chemical Physics* **2007**, *9*, 5183.

[91] Christov, N. C.; Danov, K. D.; Zeng, Y.; Kralchevsky, P. A.; von Klitzing, R. *Langmuir* **2010**, *26*, 915–923.

[92] Basheva, E. S.; Danov, K. D.; Kralchevsky, P. A. *Langmuir* **1997**, *13*, 4342–4348.

[93] Crocker, J. C.; Matteo, J. A.; Dinsmore, A. D.; Yodh, A. G. *Physical Review Letters* **1999**, *82*, 4352–4355.

[94] Akbulut, M.; Alig, A. R. G.; Min, Y.; Belman, N.; Reynolds, M.; Golan, Y.; Israelachvili, J. *Langmuir* **2007**, *23*, 3961–3969.

[95] Fewkes, C. J.; Tabor, R. F.; Dagastine, R. R. *Soft Matter* **2015**, *11*, 1303–1314.

[96] Zeng, Y.; von Klitzing, R. *Langmuir* **2012**, *28*, 6313–6321.

[97] Zeng, Y.; von Klitzing, R. *Soft Matter* **2011**, *7*, 5329–5338.

[98] Grandner, S.; Zeng, Y.; von Klitzing, R.; Klapp, S. H. L. *The Journal of chemical physics* **2009**, *131*, 154702.

[99] Grandner, S.; Klapp, S. H. L. *EPL (Europhysics Letters)* **2010**, *90*, 68004.

[100] Kralchevsky, P. A.; Denkov, N. D. *Chemical Physics Letters* **1995**, *240*, 385–392.

[101] Trokhymchuk, A.; Henderson, D.; Nikolov, A.; Wasan, D. T. *Langmuir* **2001**, *17*, 4940–4947.

[102] Iler, R. K. *The chemistry of silica: Solubility, polymerization, colloid and surface properties, and biochemistry*; Wiley: New York, 1979.

[103] Binnig, G.; Quate, C. F.; Gerber, C. *Physical Review Letters* **1986**, *56*, 930–933.

[104] Claesson, P. M.; Ederth, T.; Bergeron, V.; Rutland, M. W. *Advances in colloid and interface science* **1996**, *67*, 119–183.

[105] Ducker, W. A.; Senden, T. J.; Pashley, R. M. *Nature* **1991**, *353*, 239–241.

[106] Butt, H.-J. *Biophysical Journal* **1991**, *60*, 1438–1444.

[107] Senden, T. J. *Current Opinion in Colloid & Interface Science* **2001**, *6*, 95–101.

[108] Butt, H.-J.; Cappella, B.; Kappl, M. *Surface Science Reports* **2005**, *59*, 1–152.

[109] Kuznetsov, V.; Papastavrou, G. *The Review of scientific instruments* **2012**, *83*, 116103.

[110] Valmacco, V.; Elzbieciak-Wodka, M.; Besnard, C.; Maroni, P.; Trefalt, G.; Borkovec, M. *Nanoscale Horiz* **2016**, *1*, 325–330.

[111] Valmacco, V.; Elzbieciak-Wodka, M.; Herman, D.; Trefalt, G.; Maroni, P.; Borkovec, M. *Journal of colloid and interface science* **2016**, *472*, 108–115.

[112] Trefalt, G.; Palberg, T.; Borkovec, M. *Current Opinion in Colloid & Interface Science* **2017**, *27*, 9–17.

[113] Fielden, M. L.; Hayes, R. A.; Ralston, J. *Langmuir* **1996**, *12*, 3721–3727.

[114] Assemi, S.; Nguyen, A. V.; Miller, J. D. *International Journal of Mineral Processing* **2008**, *89*, 65–70.

[115] Dagastine, R. R.; Manica, R.; Carnie, S. L.; Chan, D. Y. C.; Stevens, G. W.; Grieser, F. *Science* **2006**, *313*, 210–213.

[116] Tabor, R. F.; Grieser, F.; Dagastine, R. R.; Chan, D. Y. C. *Journal of colloid and interface science* **2012**, *371*, 1–14.

[117] Helfricht, N.; Mark, A.; Dorwling-Carter, L.; Zambelli, T.; Papastavrou, G. *Nanoscale* **2017**, *9*, 9491–9501.

[118] Mark, A.; Helfricht, N.; Rauh, A.; Karg, M.; Papastavrou, G. *Small* **2019**, *15*, 1902976.

[119] Ralston, J.; Larson, I.; Rutland, M. W.; Feiler, A. A.; Kleijn, M. *Pure and Applied Chemistry* **2005**, *77*, 2149–2170.

[120] Albrecht, T. R.; Akamine, S.; Carver, T. E.; Quate, C. F. *Journal of Vacuum Science & Technology A: Vacuum, Surfaces, and Films* **1990**, *8*, 3386–3396.

[121] Hutter, J. L.; Bechhoefer, J. *Review of Scientific Instruments* **1993**, *64*, 1868–1873.

[122] Cleveland, J. P.; Manne, S.; Bocek, D.; Hansma, P. K. *Review of Scientific Instruments* **1993**, *64*, 403–405.

[123] Sader, J. E.; Chon, J. W. M.; Mulvaney, P. *Review of Scientific Instruments* **1999**, *70*, 3967–3969.

[124] Kearley, G. J., Peterson, V. K., Eds. *Neutron Applications in Materials for Energy*; Springer, 2015.

[125] Kumar, C. S., Ed. *X-ray and Neutron Techniques for Nanomaterials Characterization*; Springer: Berlin, Heidelberg, 2016.

[126] Castellanos, M. M.; McAuley, A.; Curtis, J. E. *Computational and structural biotechnology journal* **2017**, *15*, 117–130.

[127] Feigin, L. A.; Svergun, D. I.; Taylor, G. W. *Structure Analysis by Small-Angle X-Ray and Neutron Scattering*; Springer US: Boston, MA, 1987.

[128] Sivia, D. S. *Elementary Scattering Theory: For X-ray and Neutron Users*; OUP: Oxford, 2011.

[129] Pedersen, J. S. *Advances in colloid and interface science* **1997**, *70*, 171–210.

[130] Lindner, P.; Schweins, R. *Neutron News* **2010**, *21*, 15–18.

[131] Kotlarchyk, M.; Chen, S.-H. *The Journal of chemical physics* **1983**, *79*, 2461–2469.

[132] Berr, S. S. *The Journal of Physical Chemistry* **1987**, *91*, 4760–4765.

[133] Tanford, C. *The Journal of Physical Chemistry* **1972**, *76*, 3020–3024.

[134] Hansen, J.-P.; Hayter, J. B. *Molecular Physics* **1982**, *46*, 651–656.

[135] Penfold, J.; Thomas, R. K.; Li, P. X.; Tucker, I.; Petkov, J.; Petkova, R. E. *Langmuir* **2016**, *32*, 1319–1326.

[136] Helenius, A.; McCaslin, D. R.; Fries, E.; Tanford, C. *Methods in enzymology* **1979**, *56*, 734–749.

[137] Sharma, K. S.; Patil, S. R.; Rakshit, A. K.; Glenn, K.; Doiron, M.; Palepu, R. M.; Hassan, P. A. *The Journal of Physical Chemistry B* **2004**, *108*, 12804–12812.

[138] Spaar, A.; Salditt, T. *Biophysical Journal* **2003**, *85*, 1576–1584.

[139] McNeil, S. E., Ed. *Characterization of nanoparticles intended for drug delivery*; Humana Press: New York, 2010; Vol. 697.

[140] Hunter, R. J.; Ottewill, R. H.; Rowell, R. L. *Zeta Potential in Colloid Science: Principles and Applications*; Elsevier Science: Burlington, 2013.

[141] Ludwig, M.; Witt, M. U.; von Klitzing, R. *Advances in colloid and interface science* **2019**, *269*, 270–276.

[142] Danov, K. D.; Basheva, E. S.; Kralchevsky, P. A.; Ananthapadmanabhan, K. P.; Lips, A. *Advances in colloid and interface science* **2011**, *168*, 50–70.

[143] Zeng, Y.; von Klitzing, R. *Journal of Physics. Condensed Matter* **2012**, *24*, 464125.

[144] Semmler, M.; Mann, E. K.; Rička, J.; Borkovec, M. *Langmuir* **1998**, *14*, 5127–5132.

[145] Tulpar, A.; Tilton, R. D.; Walz, J. Y. *Langmuir* **2007**, *23*, 4351–4357.

[146] Ji, S.; Walz, J. Y. *Langmuir* **2013**, *29*, 15159–15167.

[147] Ji, S.; Walz, J. Y. *Current Opinion in Colloid & Interface Science* **2015**, *20*, 39–45.

[148] Lele, B. J.; Tilton, R. D. *Langmuir* **2020**, *36*, 10772–10784.

[149] Henderson, D. *Journal of colloid and interface science* **1988**, *121*, 486–490.

[150] Roth, R.; Evans, R.; Dietrich, S. *Physical Review E* **2000**, *62*, 5360–5377.

[151] Lebowitz, J. L. *Physical Review* **1964**, *133*, A895–A899.

[152] Carnahan, N. F.; Starling, K. E. *The Journal of chemical physics* **1969**, *51*, 635–636.

[153] Anachkov, S. E.; Danov, K. D.; Basheva, E. S.; Kralchevsky, P. A.; Ananthapadmanabhan, K. P. *Advances in colloid and interface science* **2012**, *183-184*, 55–67.

[154] Mahajan, R. K.; Chawla, J.; Vohra, K. K.; Aswal, V. K. *Journal of Applied Polymer Science* **2010**, *36*, 3038–3046.

[155] Penfold, J.; Thomas, R. K.; Li, P. X.; Petkov, J. T.; Tucker, I.; Webster, J. R. P.; Terry, A. E. *Langmuir* **2015**, *31*, 3003–3011.

[156] Nayem, J.; Zhang, Z.; Tomlinson, A.; Zarraga, I. E.; Wagner, N. J.; Liu, Y. *Journal of pharmaceutical sciences* **2020**, *109*, 1498–1508.

[157] Quina, F. H.; Nassar, P. M.; Bonilha, J. B. S.; Bales, B. L. *The Journal of Physical Chemistry* **1995**, *99*, 17028–17031.

[158] Buchner, R.; Baar, C.; Fernandez, P.; Schrödle, S.; Kunz, W. *Journal of Molecular Liquids* **2005**, *118*, 179–187.

[159] Sterpone, F.; Pierleoni, C.; Briganti, G.; Marchit, M. *Langmuir* **2004**, *20*, 4311–4314.

[160] Sommer, C.; Pedersen, J. S.; Garamus, V. M. *Langmuir* **2005**, *21*, 2137–2149.

[161] Manning, G. S. *The Journal of chemical physics* **1969**, *51*, 924–933.

[162] Treiner, C.; Khodja, A.; Fromon, M. *Journal of colloid and interface science* **1989**, *128*, 416–421.

[163] Bucci, S.; Fagotti, C.; Degiorgio, V.; Piazza, R. *Langmuir* **1991**, *7*, 824–826.

[164] Cabane, B.; Duplessix, R. *Journal de Physique* **1987**, *48*, 651–662.

[165] Brown, W.; Fundin, J.; Miguel, M. d. G. *Macromolecules* **1992**, *25*, 7192–7198.

[166] Fajalia, A. I.; Tsianou, M. *The journal of physical chemistry. B* **2014**, *118*, 10725–10739.

[167] Dey, J.; Sultana, N.; Kumar, S.; Aswal, V. K.; Choudhury, S.; Ismail, K. *RSC Advances* **2015**, *5*, 74744–74752.

[168] Lindner, P., Zemb, T., Eds. *Neutrons, X-rays and light: Scattering methods applied to soft condensed matter*, 1st ed.; Elsevier: Amsterdam, 2002.

[169] Greene, D. G.; Ferraro, D. V.; Lenhoff, A. M.; Wagner, N. J. *Journal of Applied Crystallography* **2016**, *49*, 1734–1739.

[170] Grant, L. M.; Tiberg, F.; Ducker, W. A. *The Journal of Physical Chemistry B* **1998**, *102*, 4288–4294.

[171] Patist, A.; Kanicky, J. R.; Shukla, P. K.; Shah, D. O. *Journal of colloid and interface science* **2002**, *245*, 1–15.

[172] Arnim Cumme, G.; Blume, E.; Bublitz, R.; Hoppe, H.; Horn, A. *Journal of Chromatography A* **1997**, *791*, 245–253.

[173] Ayorinde, F. O.; Gelain, S. V.; Johnson, J. H.; Wan, L. W. *Rapid Communications in Mass Spectrometry* **2000**, *14*, 2116–2124.

[174] Frison-Norrie, S.; Sporns, P. *Journal of agricultural and food chemistry* **2001**, *49*, 3335–3340.

[175] Raith, K.; Schmelzer, C. E. H.; Neubert, R. H. H. *International journal of pharmaceutics* **2006**, *319*, 1–12.

[176] Hewitt, D.; Alvarez, M.; Robinson, K.; Ji, J.; Wang, Y. J.; Kao, Y.-H.; Zhang, T. *Journal of Chromatography A* **2011**, *1218*, 2138–2145.

[177] Li, Y.; Hewitt, D.; Lentz, Y. K.; Ji, J. A.; Zhang, T. Y.; Zhang, K. *Analytical chemistry* **2014**, *86*, 5150–5157.

[178] Danov, K. D.; Kralchevsky, P. A.; Ananthapadmanabhan, K. P. *Advances in colloid and interface science* **2014**, *206*, 17–45.

[179] Funasaki, N.; Hada, S.; Neya, S. *The Journal of Physical Chemistry* **1984**, *88*, 1243–1248.

[180] Preu, H.; Zradba, A.; Rast, S.; Kunz, W.; Hardy, E. H.; Zeidler, M. D. *Physical Chemistry Chemical Physics* **1999**, *1*, 3321–3329.

[181] Phillies, G. D. J.; Hunt, R. H.; Strang, K.; Sushkin, N. *Langmuir* **1995**, *11*, 3408–3416.

[182] Borbély, S. *Langmuir* **2000**, *16*, 5540–5545.

[183] Tomšič, M.; Bešter-Rogač, M.; Jamnik, A.; Kunz, W.; Touraud, D.; Bergmann, A.; Glatter, O. *The Journal of Physical Chemistry B* **2004**, *108*, 7021–7032.

[184] Tóth, G.; Madarász, A. *Langmuir* **2006**, *22*, 590–597.

[185] Sasaki, T.; Hattori, M.; Sasaki, J.; Nukina, K. *Bulletin of the Chemical Society of Japan* **1975**, *48*, 1397–1403.

[186] Kale, K. M.; Cussler, E. L.; Evans, D. F. *The Journal of Physical Chemistry* **1980**, *84*, 593–598.

[187] Ludwig, M.; von Klitzing, R. *Physical Chemistry Chemical Physics* **2021**, *59*, 2010.

[188] Mondain-Monval, O.; Leal-Calderon, F.; Phillip, J.; Bibette, J. *Physical Review Letters* **1995**, *75*, 3364–3367.

[189] Moazzami-Gudarzi, M.; Kremer, T.; Valmacco, V.; Maroni, P.; Borkovec, M.; Trefalt, G. *Physical review letters* **2016**, *117*, 088001.

[190] Téllez, G. *Philosophical transactions. Series A, Mathematical, physical, and engineering sciences* **2011**, *369*, 322–334.

[191] Giuliani, G.; Vignale, G. *Quantum theory of the electron liquid*; Cambridge University Press: Cambridge, 2005.

[192] Beresford-Smith, B.; Chan, D. Y. C. *Faraday Discussions of the Chemical Society* **1983**, *76*, 65.

[193] Beresford-Smith, B.; Chan, D. Y.; Mitchell, D. *Journal of colloid and interface science* **1985**, *105*, 216–234.

[194] Atkins, P. W.; de Paula, J.; Keeler, J. *Atkins' physical chemistry*, 11th ed.; Oxford University Press, 2018.

[195] Smith, A. M.; Borkovec, M.; Trefalt, G. *Advances in colloid and interface science* **2019**, 102078.

[196] Klapp, S. H. L.; Grandner, S.; Zeng, Y.; von Klitzing, R. *Soft Matter* **2010**, *6*, 2330.

[197] Klapp, S. H. L.; Zeng, Y.; Qu, D.; von Klitzing, R. *Physical Review Letters* **2008**, *100*, 118303.

[198] Maroni, P.; Gvaramia, M.; Kosior, D.; Kubiak, K.; Scarratt, L.; Smith, A. M.; Merkel, D. G.; Bottyán, L.; Borkovec, M. *Physical Chemistry Chemical Physics* **2020**, *22*, 6449–6456.

[199] Hoth, J.; Hausen, F.; Müser, M. H.; Bennewitz, R. *Journal of Physics. Condensed Matter* **2014**, *26*, 284110.

[200] Schön, S.; von Klitzing, R. *Soft Matter* **2018**, *14*, 5383–5392.

[201] Bolt, G. H. *The Journal of Physical Chemistry* **1957**, *61*, 1166–1169.

[202] Dove, P. M.; Craven, C. M. *Geochimica et Cosmochimica Acta* **2005**, *69*, 4963–4970.

[203] Biggs, S.; Prieve, D. C.; Dagastine, R. R. *Langmuir* **2005**, *21*, 5421–5428.

[204] Smith, A. M.; Lee, A. A.; Perkin, S. *The Journal of Physical Chemistry Letters* **2016**, *7*, 2157–2163.

[205] Lee, A. A.; Perez-Martinez, C. S.; Smith, A. M.; Perkin, S. *Physical review letters* **2017**, *119*, 026002.

[206] Lee, A. A.; Perez-Martinez, C. S.; Smith, A. M.; Perkin, S. *Faraday discussions* **2017**, *199*, 239–259.

[207] Wang, J.; Bard, A. J. *The Journal of Physical Chemistry B* **2001**, *105*, 5217–5222.

[208] Barten, D.; Kleijn, J. M.; Duval, J.; Leeuwen, H. P. V.; Lyklema, J.; Cohen Stuart, M. A. *Langmuir* **2003**, *19*, 1133–1139.

[209] Taboada-Serrano, P.; Vithayaveroj, V.; Hou, C.-H.; Yiacoumi, S.; Tsouris, C. *Industrial & Engineering Chemistry Research* **2008**, *47*, 3525–3531.

[210] Kuznetsov, V.; Papastavrou, G. *The Journal of Physical Chemistry C* **2014**, *118*, 2673–2685.

[211] de Beer, S.; van den Ende, D.; Mugele, F. *Nanotechnology* **2010**, *21*, 325703.

[212] de Beer, S.; van den Ende, D.; Mugele, F. *Journal of Physics: Condensed Matter* **2011**, *23*, 112206.

Appendix

Curriculum vitae

[n.a. in online version]

Acknowledgements

[n.a. in online version]